

Electronic Theses and Dissertations, 2020-

2022

Integrated Electro-Optic, Microwave, and Nonlinear Photonic Devices on Thin-Film Lithium Niobate

Milad Gholipour Vazimali
University of Central Florida

 Part of the [Electromagnetics and Photonics Commons](#)
Find similar works at: <https://stars.library.ucf.edu/etd2020>
University of Central Florida Libraries <http://library.ucf.edu>

This Doctoral Dissertation (Open Access) is brought to you for free and open access by STARS. It has been accepted for inclusion in Electronic Theses and Dissertations, 2020- by an authorized administrator of STARS. For more information, please contact STARS@ucf.edu.

STARS Citation

Gholipour Vazimali, Milad, "Integrated Electro-Optic, Microwave, and Nonlinear Photonic Devices on Thin-Film Lithium Niobate" (2022). *Electronic Theses and Dissertations, 2020-*. 1568.
<https://stars.library.ucf.edu/etd2020/1568>

INTEGRATED ELECTRO-OPTIC, MICROWAVE, AND NONLINEAR PHOTONIC
DEVICES ON THIN-FILM LITHIUM NIOBATE

by

MILAD GHOLIPOUR VAZIMALI
B.S. Sharif University of Technology, 2014
M.S. University of Tehran, 2017
M.S. University of Central Florida, 2020

A dissertation submitted in partial fulfilment of the requirements
for the degree of Doctor of Philosophy
in the College of Optics and Photonics
at the University of Central Florida
Orlando, Florida

Summer Term
2022

Major Professor: Sasan Fathpour

© 2022 Milad Gholipour Vazimali

ABSTRACT

Lithium niobate has numerous extraordinary features that make it useful for a wide range of applications, particularly in optics. The material's strong electro-optic effect and second-order nonlinearities are two prime examples with applications in optical modulation and wavelength conversion, respectively. The thin-film lithium niobate platform has revitalized the conventional applications of lithium niobate during the last decade. The platform is now one of the most actively investigated subdisciplines in integrated photonics. The waveguides on this innovative platform are high index contrast, resulting in a size reduction of more than 20 times and a bending radius decrease of about two orders of magnitude when compared to traditional counterparts. These ultracompact waveguides facilitate the realization of highly efficient photonic devices, some of which are presented in this work. First, tunable dual-channel integrated Bragg filters with ultranarrow linewidths are demonstrated. These filters have potential applications in optical communication, sensing, and quantum optics. Next, high-speed Mach-Zehnder electro-optic modulators with an extrapolated 3-dB bandwidth of 170 GHz and low half-wave voltage-length product of 3.3 V.cm are presented. Furthermore, microwave-to-optical converters with integrated antennas and optical waveguides are demonstrated with improved efficiency compared to the currently existing devices for integrated microwave photonics applications. Afterward, fabricated periodically-poled lithium niobate devices are utilized to illustrate nonlinear wavelength translators through cascaded sum- and difference-frequency generations. Finally, further works on these research topics, which are appropriate for future research, are discussed.

To my family

ACKNOWLEDGMENTS

First and foremost, I would like to convey my heartfelt thanks to Prof. Sasan Fathpour, my Ph.D. adviser. It was a privilege to be part of his research lab and progress under his tutelage. I will be eternally thankful for his wisdom, patience, trust, and unwavering support during my Ph.D. studies.

I am also grateful to my supportive Ph.D. committee members, Prof. Peter J. Delfyett, Prof. Patrick L. LiKamWa, and Dr. Arkadiy A. Lyakh for their guidance.

I would like to thank CREOL faculty and staff, Prof. Patrick L. LiKamWa, Dr. Ivan Divliansky, Nathan Aultman, Dr. Keqi Qin, and James D. Ross for maintaining the cleanroom equipment and their help and guidance in my fabrication processes.

I would also like to express my appreciation for the support of all the CREOL administrative staff as well as former CREOL faculty members Prof. Mercedeh Khajavikhan and Prof. Ronald G. Driggers.

I want to thank our collaborators, Dr. Tyler Nagy, Dr. Kim Lee, and Prof. Gregory Kanter for their contributions.

I want to appreciate my former and current colleagues, F. A. Juneghani, Dr. K. Abdelsalam, Dr. A. Honardoost, Dr. T. Sjaardema, E. Ordouie, A. Caputo, P. Thapalia, and P. Kulkarni for their help, contributions, and fun moments we had in the cleanroom and lab.

I would like to express my endless gratitude to my friends, Dr. I. Hatipoglu, Dr. M. Yessenov, A. Shiri, M. Eshaghi, M. Pilevar, M. Mahmoodvand, Dr. N. Mohammadian,

K. Fazelpour, A. Fardoost, and F. G. Vanani for fruitful discussions, motivation, and supporting me in the moments of frustration.

Last but not least, I am forever grateful for my family's unfailing support - my dear parents, to whom I owe everything, and my wonderful siblings.

TABLE OF CONTENTS

LIST OF FIGURES	xi
LIST OF TABLES	xviii
CHAPTER 1: INTRODUCTION	1
1.1 Lithium Niobate and its Physical Properties	1
1.2 Thin-Film Lithium Niobate	2
1.3 Pockel's Effect	5
1.4 Second-Order Nonlinear Optics	7
1.4.1 Periodic Poling in Straight Waveguides	10
1.4.2 Periodic Poling in Microresonators	14
CHAPTER 2: TUNABLE DUAL CHANNEL FILTER	17
2.1 Introduction	17
2.2 Operation Principle and Design	19
2.3 Experimental Results and Discussion	22
2.4 Electro-Optical Tuning of Central Wavelength	25

CHAPTER 3: HIGH-SPEED ELECTRO-OPTIC MODULATOR	29
3.1 Introduction	30
3.2 MZM with Non-Centered Positioning of Optical Waveguides	31
3.3 Results and Discussion	35
3.3.1 Static EO Measurement	35
3.3.2 Electrical Characterization	36
3.3.3 EO Response	39
3.3.4 Data Modulation	41
3.4 Conclusion	43
3.5 Supplemental Document	43
3.5.1 Device Fabrication	43
3.5.2 Electro-Optic Response of the Modulators up to 200 GHz	44
3.5.3 Ultra-High-Speed Electro-Optic Characterization	45
3.5.4 Data Transmission Characterization	46
CHAPTER 4: MICROWAVE TO OPTICAL CONVERTER	48
4.1 Introduction	48
4.2 Theory	50

4.2.1	Field Enhancement Factor (FE)	51
4.2.2	First Sideband-to-Carrier Ratio (FSBCR)	52
4.3	Simulation and Design	53
4.3.1	Optical Waveguide	54
4.3.2	Antenna	55
4.4	Simulation Results and Discussion	56
4.5	Experimental Results and Discussion	60
4.6	Conclusion	64
CHAPTER 5: NONLINEAR WAVELENGTH TRANSLATOR		66
5.1	Introduction	66
5.1.1	Sum-Frequency Generation (SFG)	66
5.1.2	Difference-Frequency Generation (DFG)	68
5.1.3	Cascaded Second-Order Nonlinear Processes	69
5.2	Theory	71
5.3	Design	74
5.3.1	Efficiency	74
5.3.2	Bandwidth	75

5.4	Experimental Results and Discussion	80
CHAPTER 6: CONCLUSION AND FUTURE WORK		84
6.1	Integrated Frequency-Domain Hong-Ou-Mandel Interferometer	84
6.2	Microwave to Optical Converter on TFLN on Quartz Substrate	86
6.3	Experimental Demonstration of Nonlinear Wavelength Translator	90
APPENDIX: COPYRIGHT PERMISSIONS		92
LIST OF REFERENCES		98

LIST OF FIGURES

Figure 1.1: Comparison of optical mode areas, index contrast, and crystal orientations in a) Conventional LN waveguides and b) Thin-film LN waveguides.	3
Figure 1.2: Crystal orientations and corresponding preferred polarization to achieve maximum efficiency for nonlinear processes in TFLN using a,b) Quasi phase-matching via periodic poling and c,d) Modal phase-matching.	9
Figure 1.3: Various phase-matching methods used on the TFLN platform. a) Birefringent phase-matching. b) Modal phase-matching. c) Grating-assisted quasi phase-matching or mode shape modulation. d) Periodically poled lithium niobate (PPLN) on a straight waveguide. e) Natural quasi-phase-matching, which is conceptually similar to cyclic phase-matching. f) Phase-matching-free metasurface.	11
Figure 1.4: Periodically-poled lithium niobate devices in different structures. a) Straight waveguide. b) Racetrack resonator that is poled on one of the straight arms. c) Radially-poled microring resonator. d) Radially-poled microdisk, poled using piezo-response force microscopy technique, in which they also demonstrated poling period as small as 200 nm.	14

Figure 2.1: (a) 3-D schematic of the tunable dual-channel PS-BGF; (b) Top-view of the device schematic is showing the different design parameters (c) Cross-section view of the waveguide at the non-corrugated region, showing the waveguide dimensions and the different materials. The COMSOL simulation of optical TE mode (at 1550 nm) and DC electric field (arrows) from the electrodes are superimposed; (d) False-color SEM image of the fabricated structure around one of the phase-shift sections, showing the fabricated grating (red) and the surrounding metal electrodes (golden). 21

Figure 2.2: A schematic diagram of the characterization setup. SOA: semiconductor optical amplifier; PC: Polarization Controller; P.D: Photodiode; OSA: Optical Spectrum Analyzer; DUT: Device Under Test. . . . 23

Figure 2.3: Normalized transmission spectrum of the filter from both experiment (black, solid) and simulation (green, dotted), demonstrating a good agreement. The inset shows a high-resolution measurement of the peaks (linear scale) using a high-speed photodiode and a synchronized digital oscilloscope. 25

Figure 2.4: Characterization of EO tuning of the PS-BGF, showing (a) filter’s transmission spectrum shift at three applied voltage values; (b) Central wavelength shift as a function of the electric field. 27

Figure 3.1: (a) Cross-sectional view of the high-speed modulator with non symmetrical optical waveguides with respect to the electrodes to reduce the drive voltage, and the incorporated dielectric buffer layer to prevent absorption loss. The compact optical mode has a group index of 2.23. (b) Microscopic image of a fabricated TFLN modulator. 32

Figure 3.2: 3-dB bandwidth and length of modulator as a function of parameter D with and without a silicon dioxide buffer layer underneath the electrodes for fixed values of $G = 10\mu m$, $V_\pi = 6.6$ V and optical loss of < 0.02 dB/cm. Bandwidth and length of modulator without the buffer layer are not presented for $D > 1.5 \mu m$ because the resulting optical loss is more than 0.02 dB/cm. 34

Figure 3.3: Normalized optical transmission of (a) modulator #1 and (b) modulator #2 as a function of the applied electrical voltage, showing V_π of 4.4 V and 6.6 V, respectively, for 5 mm-long devices. (c) Variation of V_π and optical loss versus the distance between the signal electrode edge and the center of the optical waveguide (parameter D). 36

Figure 3.4: Simulation and experimental results of RF loss (α_m), RF effective index (n_m), and characteristic impedance (z_m) of the transmission line as a function of frequency for modulator # 2. 37

Figure 3.5: Measured EO responses referenced to devices with DC $V_{\pi}L$ of (a) 2.2 V.cm and (b) 3.3 V.cm, showing ultra-high 3-dB bandwidths of 84 GHz and well beyond 100 GHz, respectively. The EO responses - measured using a vector network analyzer (VNA) up to 67 GHz and an optical spectrum analyser (OSA) from 60 to 100 GHz - are shown with solid violet and orange lines, respectively. (c) Schematic of the experimental set-up for measuring the OSA-based measurements; EDFA: erbium-doped fiber amplifier; FPC: Fiber polarization controller; DBI-DAC: digital-band-interleaved digital-to-analog converter; HF: High frequency; MF: Medium frequency; LF: Low frequency. 38

Figure 3.6: Extracted RF V_{π} from EO response shown in Fig. 3.5(a) and 3.5(b) as a function of frequency. 39

Figure 3.7: High-speed digital data modulation measurements. (a) Schematic of the experimental set-up for the data modulation using 67 GHz real time oscilloscope. Eye diagrams for (b) OOK modulation at data rates of 100 Gb/s. (c), (d) PAM-4 modulation at 53.125 Gbaud (106.25 Gb/s) and 100 Gbaud (200 Gb/s), respectively and (e) Ultra-high speed PAM-8 modulation at 80 Gbaud (240 Gb/s). 42

Figure 3.8: Experimental and extrapolated Data of (a) RF loss (α_m), (b) RF effective index (n_m), (c) and characteristic impedance (Z_m) of the transmission line versus frequency. 45

Figure 4.1: Cross-section of an EO sensor on the thin-film lithium niobate platform	51
Figure 4.2: Fundamental TE mode of the optical waveguide	54
Figure 4.3: Schematic and dimensions of designed a) patch antenna and b) bow-tie antenna for a center frequency of 28 GHz on TFLN on quartz substrate	55
Figure 4.4: a) Electric field distribution within the gap and b) FE versus frequency for the EO sensor on TFLN on quartz substrate with a bow-tie antenna	58
Figure 4.5: a) Electric field distribution within the gap and b) FE versus frequency for the EO sensor on TFLN on quartz substrate with a patch antenna	59
Figure 4.6: a) Mask layout for the fabrication. Some microscopic images of the fabricated b) Bow-tie and patch antennas and c) Waveguides and ring resonators on TFLN platform on Silicon substrate	61
Figure 4.7: a) Optical measurement setup. b) ring resonator measurement result showing 2.26 dB/cm of propagation loss.	62
Figure 4.8: a) Output optical spectrum with and without RF power. b) Frequency response of the device.	63
Figure 4.9: Sideband to carrier ratio as a function of the applied RF power.	64

Figure 4.10: Photonic down-conversion experiment results. a) Detected signal at 500 MHz frequency can be observed as a result of down-conversion process. b) Quadratic relation (slope of 2 in the logarithmic scale) between the input electric field and power of the down-converted tone	65
Figure 5.1: Schematic of a wavelength translator using cascaded SFG/DFG processes	67
Figure 5.2: Some of the schemes used for implementing cascaded $\chi^{(2)}$ processes in TFLN and the corresponding harmonic generations. a) Two PPLN sections with different poling periods to enable SHG/SFG cascading for a THG device and SHG/SHG for a FHG device. b) Dual-period PPLN microdisk with demonstrated THG and FHG. c) THG and FHG on a single PPLN device via pulse pumping. d) SHG and THG on a microdisk through cascaded SHG/SFG by taking advantage of the natural BPM.	70
Figure 5.3: Energy-level description of the cascaded SFG/DFG process for wavelength translation	71
Figure 5.4: Schematic drawing of the design with parameters	76
Figure 5.5: Mask layout used for fabrication of the devices for nonlinear wavelength translator project.	79
Figure 5.6: Some of the microscopic images and the fabricated chip.	80
Figure 5.7: Poling and measurement setup.	81

Figure 5.8: Applying voltages more than 500 V resulted in burning the electrodes.	82
Figure 5.9: Second-harmonic generation in one of the devices that was designed to work with oil.	83
Figure 6.1: a) Mask layout, b) Picture of the measurement setup, and c) Microscopic image of the fabricated chip for integrated frequency-domain HOM interferometer.	85
Figure 6.2: Measurement results for the integrated HOM interferometer. a) Filter's spectral response along with the peak separation and FWHM. b) Second-harmonic generation using the PPLN device.	87
Figure 6.3: Layout and some of the microscopic images of the fabricated devices on quartz substrate.	88
Figure 6.4: SEM images of the fabricated chip on Quartz substrate in a) and b) show the issues occurred during the fabrication. Microscopic images of the waveguides c) after E-beam lithography and development and d) after the etch step.	89
Figure 6.5: Propagation loss measurement of the first fabricated chip for the nonlinear wavelength translator project.	90
Figure 6.6: SEM image of the fabricated waveguide in the first round of fabrication demonstrating rough side walls, which causes high optical propagation loss.	91

LIST OF TABLES

Table 1.1:	Optical properties at $\lambda = 1550$ nm for some of the materials with second-order nonlinearity and electrooptic effect.	2
Table 1.2:	Performance of various devices based on straight waveguide structure for SHG using periodic poling phase-matching method. Power values for the pump and SH wavelength, as well as the absolute conversion efficiency (in %) correspond to the maximum normalized conversion efficiency and are not necessarily the maximum reported numbers in these papers.	13
Table 1.3:	Comparison of resonant-based structures for SHG using periodic poling phase-matching method.	15
Table 2.1:	Performance comparison between design and measurement of a PS-BGF with $w_g = 1.3 \mu\text{m}$, $\Delta w = 100$ nm, $\Lambda = 458$ nm, $N_1 = 700$, $N_2 = 600$, and $L_1 = L_2 = 82 \mu\text{m}$; $\Delta\lambda$: Bandwidth of the stopband; $\delta\lambda$: Linewidth of the transmission peaks; Δf : Frequency separation between the two peaks; ER: Extinction ration of the stopband edge; δP : Peak power penalty	24
Table 3.1:	Dimension of modulators (μm)	33

Table 4.1:	Comparison of performance parameters for EO sensors in microwave applications. First six rows are the simulations results of this work and next four rows are from the literature	57
Table 4.2:	Optical (insertion loss) measurement results for devices on TFLN platform on silicon substrate with input power of 13.5 dBm or 22.5 mW.	62

CHAPTER 1: INTRODUCTION

Part of the contents of this chapter has been published in: Milad Gholipour Vazimali and Sasan Fathpour "Applications of thin-film lithium niobate in nonlinear integrated photonics," Advanced Photonics 4(3), 034001 (2022).

Lithium niobate (LiNbO_3 or LN) has long been recognized as a dominant photonic material for the long-haul telecom modulator and wavelength-converter applications due to its superior electro-optic (EO) and nonlinear optical capabilities. This chapter provides the background for the rest of this dissertation by covering LN properties, introducing thin-film lithium niobate (TFLN) and its advantages, and theoretical explanation of Pockel's effect and nonlinear optics, which are the two properties of LN used in the presented projects.

1.1 Lithium Niobate and its Physical Properties

Lithium niobate is a wide-bandgap compound synthetic material with transparency window extending from ultraviolet to mid-infrared ($0.35\text{-}5\ \mu\text{m}$). It leverages strong nonlinear optic, electro-optic, piezoelectric, thermo-optic, photorefractive, and acousto-optic effects [1], making it suitable for a wide range of applications, especially in the fields of photonics and micro electro-mechanical systems (MEMS). Table 1.1 compares the optical properties including second-order nonlinearity (d coefficient), electrooptic (EO) effect (r coefficient), and refractive index of LN with other materials that possess these properties. As can be seen in this table, LN has both strong second-order nonlinearity and EO coefficients while benefits from a relatively large refractive index ($n_o = 2.21$ and $n_e = 2.14$ at $\lambda = 1550\ \text{nm}$).

GaAs has a very high d_{36} value but it is not a ferroelectric material, hence modal-phase matching is typically pursued for second-order nonlinear processes, which is less favorable than quasi-phase matching among fundamental guided modes. KTP has stronger EO coefficient, but smaller d coefficient and lower refractive index.

Table 1.1: Optical properties at $\lambda = 1550$ nm for some of the materials with second-order nonlinearity and electrooptic effect.

Material	Largest d coefficient	Largest r coefficient	Refractive index
LiNbO ₃ [2]	$d_{33} = 27$ pm/V	$r_{33} = 27$ pm/V	~ 2.2
AlN [3]	$d_{33} = 4.7$ pm/V	$r_{33} = 1$ pm/V	~ 2.1
GaAs [2]	$d_{36} = 119$ pm/V	$r_{41} = 1.5$ pm/V	~ 3.4
GaN [4]	$d_{33} = 16.5$ pm/V	$r_{33} = 1.9$ pm/V	~ 2.3
KTP [2]	$d_{33} = 14$ pm/V	$r_{33} = 35$ pm/V	~ 1.8

Conventional LN waveguides are most commonly formed by in-diffusion of titanium (Ti) dopants [5] or by the proton exchange process [6]. However, these conventional lithium niobate optical waveguides have a low index-contrast (< 0.1), hence are bulky compared to modern integrated platforms such as silicon photonics. The bulkiness impedes photonic circuit implementations and imposes high optical power requirements for nonlinear optics and EO applications.

1.2 Thin-Film Lithium Niobate

Achieving thin films of LN (with a thickness of a few hundred nanometers) that reside on an insulator cladding with a much lower index (e.g., silicon dioxide or SiO₂) - along with methods to achieve low-loss ridge or channel waveguides on the thin films - can address the above issues and yield high-contrast waveguides.

As shown in Fig. 1.1, owing to the compactness of thin-film lithium niobate (TFLN)

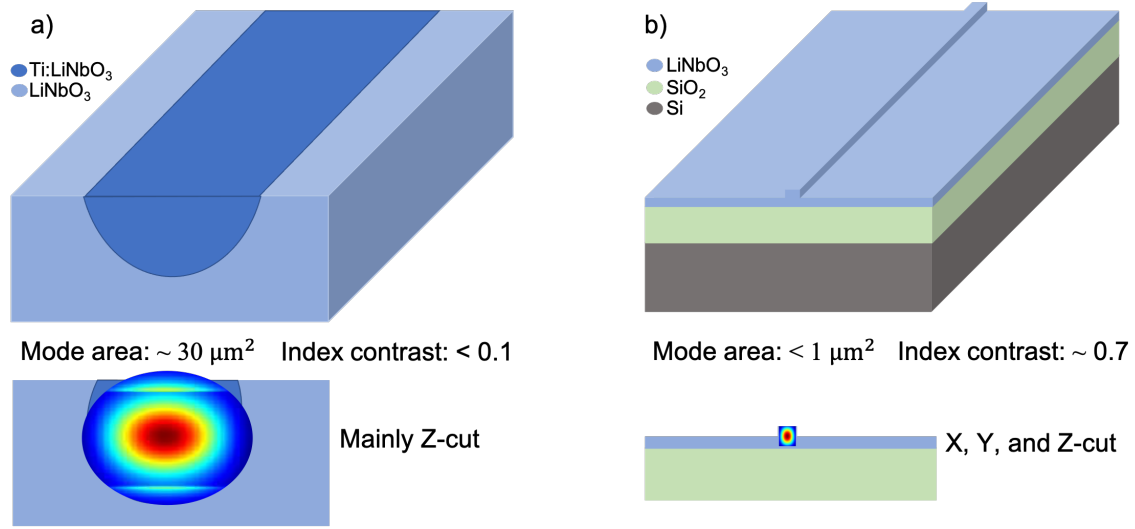


Figure 1.1: Comparison of optical mode areas, index contrast, and crystal orientations in a) Conventional LN waveguides and b) Thin-film LN waveguides.

waveguides provided by the high index contrast, optical mode sizes are remarkably smaller than those in conventional counterparts, hence much higher intensities can be achieved for the same optical power. Moreover, the overlap integral between the interacting optical modes at different wavelengths with the same parity are much larger. These differences result in significant improvements in efficiencies of various nonlinear processes. For example, the normalized conversion efficiency of second harmonic generation (SHG) has a direct relation with the overlap integral of the fundamental and second harmonic modes and an inverse relation with mode areas [7]. Moreover, bending radii in the TFLN platform is much smaller than the conventional LN because of its high index contrast, hence efficient and ultracompact microresonator structures can be easily realized on this platform for integrated nonlinear applications. Additionally and for EO applications such as EO modulators (EOMs), the gap between electrodes can be reduced significantly owing to the compactness of the waveguides, resulting in larger overlap between RF and optical fields and hence lower half-wave voltage. This and smaller bending radii result in

much smaller footprints for EOMs on TFLN compared to those in conventional LN.

Thin-film lithium niobate (TFLN) wafers on silicon (Si) substrates and high-contrast waveguides (with submicron cross-sectional dimensions) were developed for the first time at CREOL in 2013 [8]. Since the commercialization of TFLN wafers by a few vendors [9, 10, 11], efforts by several research teams have tremendously advanced the field of TFLN integrated photonics. A plethora of ultracompact linear and nonlinear optical devices and circuits (waveguides, microring resonators, modulators, grating couplers, wavelength converters, entangled photon sources, isolators, supercontinuum and comb sources, etc.) with unprecedented or significantly superior performances than the conventional (bulk) LN counterparts have been demonstrated. The combined efforts have rejuvenated LN for novel EO, nonlinear- and quantum-optic applications and the material is considered among the top candidates for heterogeneous integrated photonics. That is when multiple materials are monolithically integrated on the same substrate (preferably silicon), while each material is chosen for the functionalities that it suits the best.

TFLN is still under investigation for a better understanding of its fundamental properties, such as crystal defects, optical damage [12], and the photorefractive effect [13]. First-principle studies have also been used to explore new capabilities of the material [14, 15]. Dry etching of LN is challenging in bulky conventional waveguides with deep sidewalls, hence diffusion or implantation of dopants are typically preferred. Etching appeared to be challenging in the early years of TFLN, thus rib-loading techniques were adopted [8, 16, 17], which is indeed advantageous for EO devices in some aspects [18]. However, direct etching of LN is preferred for nonlinear-optic applications. Partially thanks to the shallow etching required in TFLN waveguides, optical propagation losses as low as 0.027 dB/cm [19], as well as intrinsic Q -factors beyond 10^8 [20], have been achieved. Even at the wafer level, a propagation loss of 0.27 dB/cm has been demonstrated [21], which is

an important milestone for large-scale integration. Progress in fabrication processes on TFLN is reviewed elsewhere [22, 23].

Numerous studies have also been conducted on the technological improvement of the platform such as domain engineering [24, 22, 25, 26, 27], which is particularly important for nonlinear devices based on periodic poling. Increasing number of functionalities are being demonstrated on TFLN and are rendering it a fully functional integrated platform. For example, light sources including rare-earth ion-doped [28, 29, 30, 31, 32, 33] and Raman lasers [34, 35], as well as heterogeneously integrated electrically-pumped III-V laser [36, 37] have been demonstrated. Shams *et al.* [37] adopted flip-chip bonding and demonstrated electrically pumped DFB laser on TFLN with up to 60 mW of optical power coupled to the TFLN waveguide. The performance of EO modulators is still being further improved [38, 39], with a recently reported data transmission rate of 1.96 Tb/s at a single wavelength with 110 GHz 3-dB bandwidth and < 1 V of driving voltage [40]. Progress has been made in design and experimental results to enhance the EO bandwidth of TFLN modulators into the subterahertz regime [18, 41]. Other components, such as highly efficient couplers [42], tunable filters [43], optical isolators [44], and programmable spatial light modulators (SLM) [45] have also been reported.

1.3 Pockel's Effect

Refractive indices of LN can be varied via applying electric field, which is called electro-optic effect. The variations can be described in terms of impermeability tensor η_{ij} , in which $\eta_{ij} = \epsilon_0 / \epsilon_{ij} = 1 / n_{ij}^2$ and is formulated as:

$$\eta_{ij}(E_0) = \eta_{ij}^{(0)} + \Delta\eta_{ij}(E_0) = \eta_{ij}^{(0)} + \sum_k r_{ijk} E_{k0} + \sum_k s_{ijkl} E_{k0} E_{l0} + \dots, \quad (1.1)$$

where η_{ij} is the field-independent relative impermeability, r_{ijk} is the linear EO coefficient called Pockel's coefficient, and s_{ijkl} is the quadratic EO coefficient called the Kerr coefficient. In Equ. 1.1, indices of i and j are related to the optical field, and indices of k and l are related to the electrical field. Because $\eta_{ij} = \eta_{ji}$ and $\Delta\eta_{ij} = \Delta\eta_{ji}$, indices of i and j can be replaced with α , therefore, Equ. 1.1 is reduced to:

$$\eta_{\alpha}(E_0) = \eta_{\alpha}^{(0)} + \Delta\eta_{\alpha}(E_0) = \eta_{\alpha}^{(0)} + \sum_k r_{\alpha k} E_{k0} + \sum_k s_{\alpha k l} E_{k0} E_{l0} + \dots, \quad (1.2)$$

where $\alpha = 1, 2, \dots, 6$. Pockel's effect only exist in non-centrosymmetric materials and can be expressed as:

$$\Delta\eta_{\alpha} = \sum_k r_{\alpha k} E_{k0}, \quad (1.3)$$

Equation 1.3 can be written in matrix form as:

$$\Delta\eta = \begin{bmatrix} r_{11} & r_{12} & r_{13} \\ r_{21} & r_{22} & r_{23} \\ r_{31} & r_{32} & r_{33} \\ r_{41} & r_{42} & r_{43} \\ r_{51} & r_{52} & r_{53} \\ r_{61} & r_{62} & r_{63} \end{bmatrix} \begin{bmatrix} E_x \\ E_y \\ E_z \end{bmatrix}. \quad (1.4)$$

In the case of LN and due to the symmetry, Equ. 1.4 can be reduced to:

$$\Delta\eta = \begin{bmatrix} 0 & -r_{22} & r_{13} \\ 0 & r_{22} & r_{13} \\ 0 & 0 & r_{33} \\ 0 & r_{42} & 0 \\ r_{42} & 0 & 0 \\ r_{22} & 0 & 0 \end{bmatrix} \begin{bmatrix} E_x \\ E_y \\ E_z \end{bmatrix}. \quad (1.5)$$

The largest element of this matrix is r_{33} for LN, which can be exploited by applying an electric field along the c -axis (z -axis) of LN. Assuming an applied electric field along the z -axis (E_z), the change of refractive indices in LN can be written as:

$$n_o(E_z) \approx n_o(E=0) - \frac{1}{2}n_o^3r_{13}E_z \quad (1.6)$$

$$n_e(E_z) \approx n_e(E=0) - \frac{1}{2}n_e^3r_{33}E_z \quad (1.7)$$

1.4 Second-Order Nonlinear Optics

The polarization of a material, i.e., P , can be expressed as a power series of the applied electric field:

$$P = \epsilon_0[\chi^{(1)}E + \chi^{(2)}E^2 + \chi^{(3)}E^3 + \dots] \equiv [P^{(1)} + P^{(2)} + P^{(3)} + \dots] \quad (1.8)$$

Where $\chi^{(i)}$ are the susceptibilities of different orders, among which $\chi^{(2)}$ is the second-order susceptibility and is of our interest in here. $\chi^{(2)}$ tensor has various elements interacting with different components of the applied electric field and may be represented using a contracted matrix notation d_{ij} under Kleinman symmetry:

$$d_{ijk} = \frac{1}{2} \chi_{ijk}^{(2)} \xrightarrow{\text{Contracted}} d_{ijk} \rightarrow d_{il} \quad (1.9)$$

The index contraction is similar to the case of electro-optic effect. The non-zero elements of $\chi^{(2)}$ are ruled by the crystal symmetry of the material. For LN with crystalline class of $3m$, the d_{il} matrix can be expressed as:

$$d_{il} = \begin{bmatrix} 0 & 0 & 0 & 0 & d_{31} & -d_{22} \\ -d_{22} & d_{22} & 0 & d_{31} & 0 & 0 \\ d_{31} & d_{31} & d_{33} & 0 & 0 & 0 \end{bmatrix} \quad (1.10)$$

Similar to the case of Pockel's effect, the largest element of d_{il} is along the c -axis (z -axis) of LN, which is $d_{33} = 27 \text{ pm/V}$, which is almost five times larger than the second largest element of this tensor, i.e., d_{31} . Therefore, in second-order nonlinear processes the crystal orientation and optical field polarization are usually chosen in a way to utilize d_{33} to achieve the best efficiency. This is depicted in Fig. 1.2 for two methods of phase-matching.

It is well-known that for an efficient nonlinear process, both the energy and momentum conservation conditions should be satisfied, the latter of which is not trivial due to waveguide and material dispersion. For example, sum-frequency generation (SFG) requires $\omega_1 + \omega_2 = \omega_3$, and $k_1 + k_2 = k_3$ or $n_1\omega_1/c + n_2\omega_2/c = n_3\omega_3/c$, where ω_i denotes the angular frequencies of the participating signals in the nonlinear process, and k_i and n_i are the corresponding wave-vector and refractive index, respectively [46]. For the case

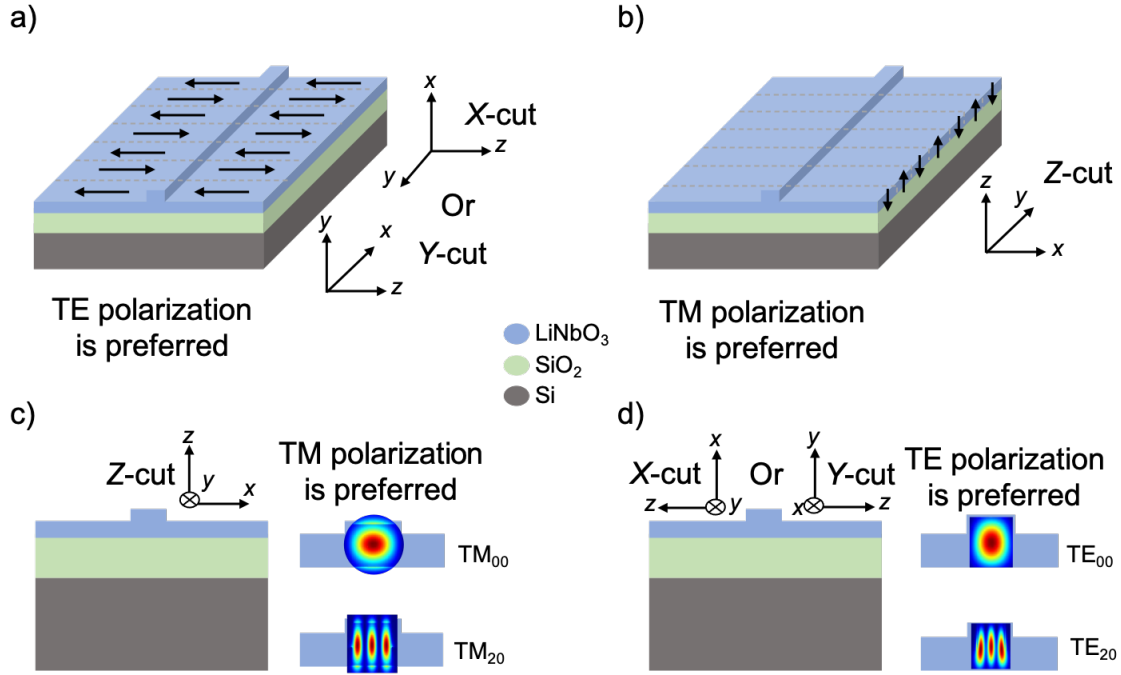


Figure 1.2: Crystal orientations and corresponding preferred polarization to achieve maximum efficiency for nonlinear processes in TFLN using a,b) Quasi phase-matching via periodic poling and c,d) Modal phase-matching.

of second-harmonic generation (SHG), in which $\omega_1 = \omega_2$, $k_1 = k_2$, and $n_1 = n_2$ the energy and momentum conservation conditions are simplified to $\omega_3 = 2\omega_1$, $k_3 = 2k_1$ or $n(\omega_1) = n(2\omega_1)$. Similarly, these conditions should be fulfilled for other efficient nonlinear processes. In the presence of a wavevector mismatch (or as often referred to as phase mismatch), e.g., $\Delta k = k_1 + k_2 - k_3 \neq 0$ for SFG, the power oscillates between the participating frequencies instead of efficiently generating the targeted frequency. Therefore, phase matching (PM) becomes the most critical aspect of any nonlinear process. Additionally and in resonant-based structures, all the frequencies involved in an efficient nonlinear process should meet the resonance condition.

Several phase-matching methods have been adopted or developed on TFLN (see Fig. 1.3).

They can be divided into two broad categories [7]. The first group is perfect PM, which achieves $\Delta k = 0$ by keeping the refractive indices for the fundamental and SH modes equal. Birefringent PM (BPM) and modal PM (MPM) are two examples of perfect PM methods. Cyclic PM (CMP), which is used in microrings and microdisks, meets the $\Delta k = 0$ condition for perfect PM in certain azimuthal angles. The second category is quasi-PM (QPM), $\Delta k \neq 0$, which is based on perturbing the nonlinear process to compensate for phase mismatches and includes grating-assisted QPM (GA-QPM) and periodic poling. Using metasurfaces, PM-free SHG is also possible.

In this report, only periodic poling has been employed as the phase-matching method for nonlinear projects. Therefore, periodic poling is explained in more details in Sections 1.4.1 and 1.4.2 for the case of SHG, which can be similarly applied to the other second-order nonlinear processes.

Single-pass straight microwaveguides and resonant-based structures such as microrings, microdisks, racetracks, as well as photonic crystals have been used to investigate nonlinear integrated photonics on the TFLN platform. Classical second-order nonlinearities such as SHG, SFG, difference-frequency generation (DFG), optical parametric amplification (OPA), and optical parametric oscillation (OPO) have been demonstrated, as well as the non-classical spontaneous parametric down-conversion (SPDC) process.

1.4.1 Periodic Poling in Straight Waveguides

Periodic poling, demonstrated first on bulk LN devices over a few decades ago [52], is the most common and efficient QPM technique on LN, especially for straight waveguides despite the fact that $\Delta k \neq 0$. In this method, in order to compensate for Δk , the sign of the relevant nonlinear coefficient is periodically altered in the areas that the power is sup-

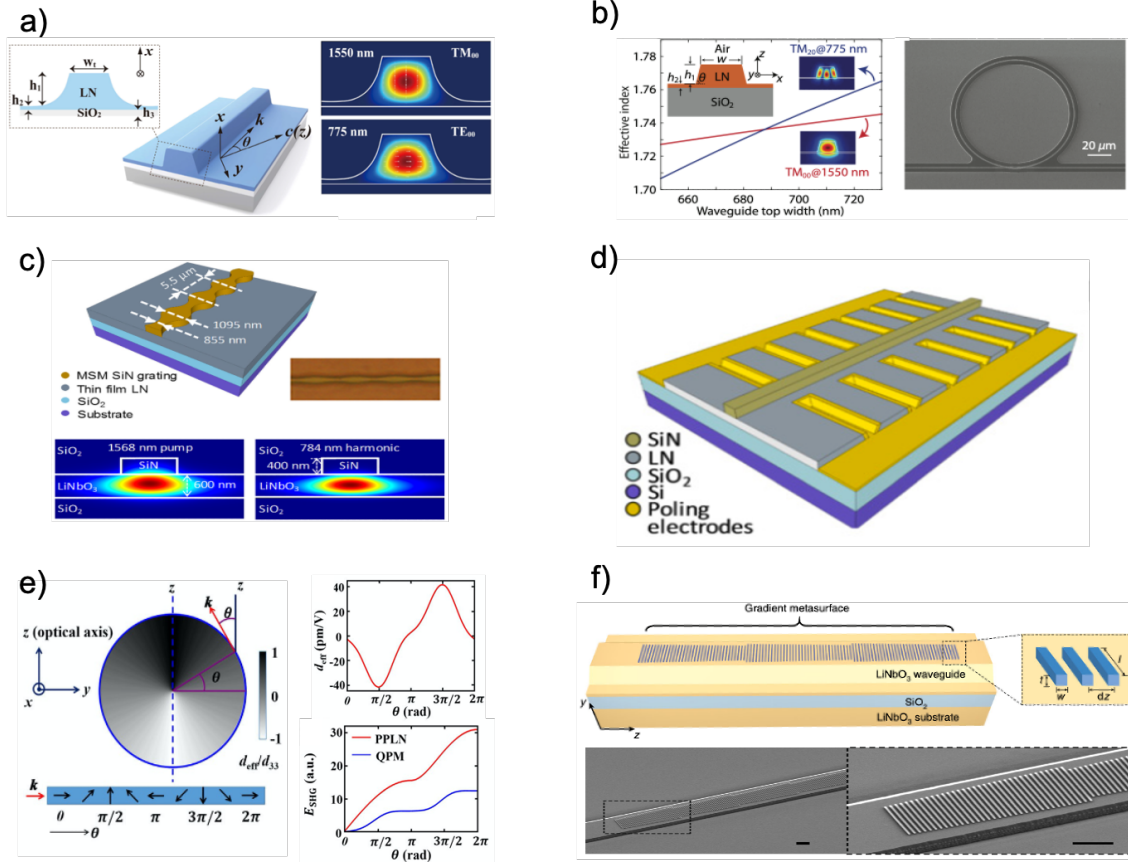


Figure 1.3: Various phase-matching methods used on the TFLN platform. a) Birefringent phase-matching [47]. b) Modal phase-matching [48]. c) Grating-assisted quasi phase-matching or mode shape modulation [49]. d) Periodically-poled lithium niobate (PPLN) on a straight waveguide [17]. e) Natural quasi-phase-matching, which is conceptually similar to cyclic phase-matching [50]. f) Phase-matching-free metasurface [51].

posed to be converted back to the pump frequency. A periodicity of $\Lambda = 2\pi / \Delta k$ with 50% duty cycle prevents power oscillation between interactive waves and facilitates a much more efficient power transfer from the pump to the targeted frequency. Devices made with this technique are called periodically-poled lithium niobate (PPLN) and are commercialized for many years. Poling is accomplished by utilizing the ferroelectric property of LN through domain inversion by applying electric fields greater than the coercive field.

For congruent bulk LN, the coercive field value is $\sim 21 \text{ V}/\mu\text{m}$ [53]. This value is higher in TFLN ($\sim 40\text{-}48 \text{ V}/\mu\text{m}$), which is possibly related to the interface of SiO_2/LN bonding [54] or the annealing step of wafer fabrication process and the subsequent out-diffusion of Li^+ ions [55]. PPLN devices typically utilize d_{33} in a Type-0 PM configuration, in which the fundamental modes can be used for both the pump and SH wavelengths, resulting in a strong overlap integral and enhanced overall conversion efficiency. Extensive studies have been conducted to optimize the poling process parameters, e.g., pre-heat treatment, temporal waveform, and electric field strength for achieving a stable and uniform $\sim 50\%$ duty cycle throughout the entire device [25, 56, 26, 27]. Recently, several groups have successfully demonstrated submicron poling periods [57, 58, 59], which are capable of compensating for large values of Δk and are of high-demand particularly for short-wavelength nonlinear devices and counter-propagating processes. Also, non-destructive measurement methods such as piezo-response force microscopy (PFM), SH confocal microscopy [60], and far-field diffraction [61] are employed to visualize and evaluate the poling quality.

In 2016, PPLN devices were demonstrated for the first time on the TFLN platform on LN [54] and Si [17] substrates. Both of these devices relied on silicon nitride (SiN) rib-loaded waveguides on TFLN. Using SiN rib-loaded waveguides and by engineering the lateral leakage, a normalized conversion efficiency of $1160 \text{ \%W}^{-1}\text{cm}^{-2}$ was achieved in 2019 for a 4.8-mm-long device [62]. Figure 1.4 depicts various types of PPLN devices demonstrated in TFLN such as straight waveguides and resonator structures.

Following the development of low-loss etching processes [19], ultra-high efficient nonlinear processes on TFLN using direct etching emerged. In 2018, using direct etching on a MgO-doped X-cut TFLN, Wang *et al.* [63] reported a normalized SHG conversion efficiencies of $2,600 \text{ \%W}^{-1}\text{cm}^{-2}$ and $2,300 \text{ \%W}^{-1}\text{cm}^{-2}$ for 4-mm-long devices on two different

Table 1.2: Performance of various devices based on straight waveguide structure for SHG using periodic poling phase-matching method. Power values for the pump and SH wavelength, as well as the absolute conversion efficiency (in %) correspond to the maximum normalized conversion efficiency and are not necessarily the maximum reported numbers in these papers.

Config & Ref	Pump / SH power	Length	$\%W^{-1}cm^{-2}$	$\%W^{-1}$	Absolute %
Type-0 [65]	3 mW / 370 nW	300 μ m	4600	4.14	\sim 0.012
Type-0 [66]	530 μ W / 2.7 μ W	5 mm	3757	939.25	\sim 0.5
Type-0 [63]	1.5 mW / 9.4 μ W	4 mm	2600	416	\sim 0.6
Type-0 [68]	2.95 mW / 31.6 μ W	4 mm	2200	352	\sim 1
Type-0 [67]	\sim 6 mW / 550 μ W	20 mm	\sim 320	\sim 1280	\sim 9

waveguide widths operating at two distinct wavelengths. MgO-doping mitigates any potential photorefractive effect in LN and hence enables high-power operation. Chen *et al.* [64] achieved a very similar performance on an undoped X-cut TFLN with an η of 2,200 $\%W^{-1}cm^{-2}$ for a 4-mm-long device. In 2019, our group showed a record high normalized SHG conversion efficiency to date of 4,600 $\%W^{-1}cm^{-2}$ on a 300- μ m-long device by actively monitoring the poling process and by performing multiple iterative cycles of poling and depoling [65]. In 2020, another very high η of 3,757 $\%W^{-1}cm^{-2}$ was reported on a longer device length of 5 mm [66]. Recently, a normalized conversion efficiency of \sim 320 $\%W^{-1}cm^{-2}$ was reported for a 20-mm-long device corresponding to \sim 1,280 $\%W^{-1}$ [67], which is relatively high for conversion efficiencies reported to this date in units of $\%W^{-1}$ for straight waveguides (see Table 1.2).

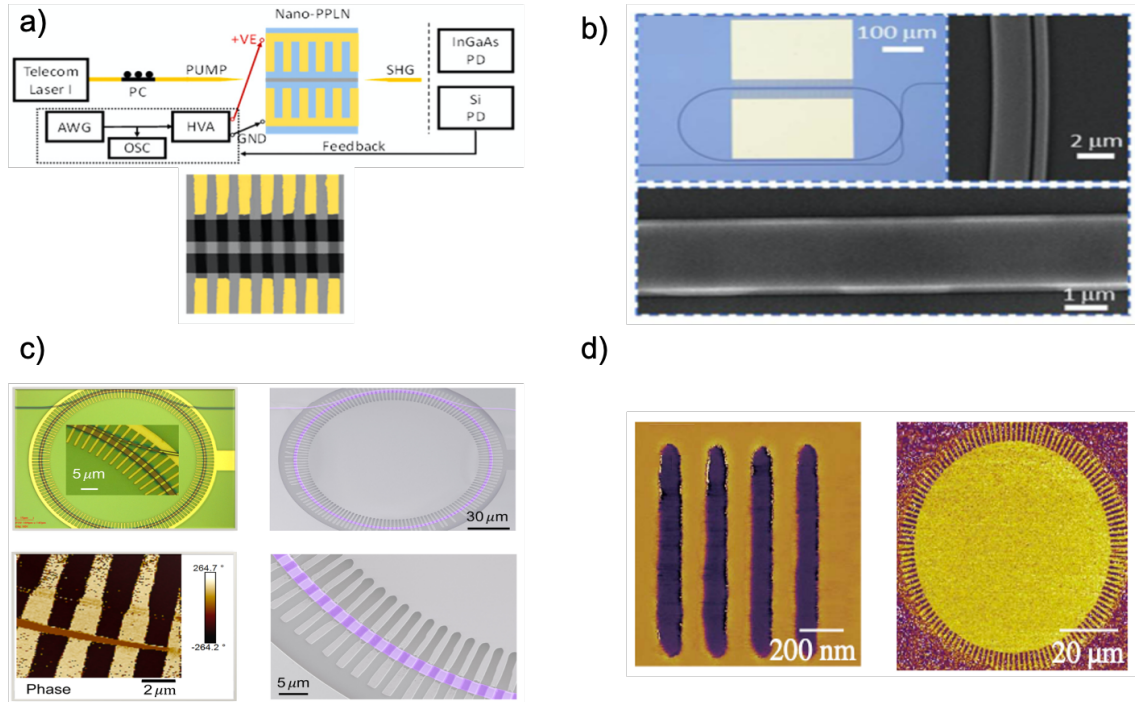


Figure 1.4: Periodically-poled lithium niobate devices in different structures. a) Straight waveguide [65]. b) Racetrack resonator that is poled on one of the straight arms [69]. c) Radially-poled microring resonator [70]. d) Radially-poled microdisk, poled using piezo-response force microscopy technique, in which they also demonstrated poling period as small as 200 nm [71].

1.4.2 Periodic Poling in Microresonators

Combining highly-efficient PPLN devices with the intensified light-matter interaction in resonant-based structures has led to a new front in nonlinear processes. In 2019, Chen *et al.* [69] utilized a doubly-resonant microcavity in a racetrack shape on X-cut MgO-doped TFLN and periodically poled the 300- μm -long straight waveguide on one arm to achieve a normalized conversion efficiency of $230,000 \text{ \%W}^{-1}$ with only $5.6 \text{ }\mu\text{W}$ of pump power and a moderate Q -factor of 3.7×10^5 . Lu *et al.* [72] radially poled a doubly-resonant microring resonator on a Z-cut TFLN and were able to demonstrate $\eta = 250,000 \text{ \%W}^{-1}$. This

Table 1.3: Comparison of resonant-based structures for SHG using periodic poling phase-matching method.

Structure & Ref	Config	Pump / SH power	Q_L at FW	$\%W^{-1}$	Absolute %
Microring [70]	Type-0	$1.05 \mu\text{W} / 56 \text{ nW}$	1.8×10^6	5×10^6	~ 5.3
Microring [72]	Type-I	$55 \mu\text{W} / 7.5 \mu\text{W}$	8×10^5	2.5×10^5	~ 13.5
Racetrack [69]	Type-0	$5.6 \mu\text{W} / 73 \text{ nW}$	3.7×10^5	2.3×10^5	~ 1.3

is while they employed d_{31} by using TE_{00} for the pump mode and TM_{00} for the SH mode due to the difficulty of poling, since the poling period of Type-0 PM would have been almost three times smaller. By utilizing d_{33} in Type-0 configuration through overcoming the poling issues and by improving the Q -factor of resonators, the same group reached $5,000,000 \ \%W^{-1}$ conversion efficiency at low power regime with a pump power of $\sim 10 \ \mu\text{W}$ [70]. As mentioned above, such very high efficiencies in $\%W^{-1}$ are possible because the ratio P_2/P_1^2 would increase inversely with a decrease of the pump power for the same order of absolute power efficiency (see Table 1.3). Nonlinear optics at such low pump powers is a welcome development. However as mentioned before, in most practical applications the amount of the generated output power is more important and the absolute power efficiency, P_2/P_1 in %, is therefore a more relevant figure of merit.

With a high single-photon coupling rate of 1.2 MHz and reasonably low dissipation rate of 184.6 MHz, the previously cited work [70] reached a single-photon anharmonicity of 0.7% [70], which could find application in integrated quantum photonics [73, 74]. Periodically-poled whispering-gallery resonators and microdisks are also demonstrated [75, 71, 76], but with much lower conversion efficiencies. Nonetheless, the developed poling techniques for microdisks using piezo-response force microscopy are invaluable and pave the

way for reaching poling periods below 100 nm [76] (see Fig. 1.4d).

CHAPTER 2: TUNABLE DUAL CHANNEL FILTER

The contents of this chapter have been published in: Kamal Abdelsalam , Ehsan Ordouie, Milad G. Vazimali, Farzaneh A. Juneghani, Prem Kumar, Gregory S. Kanter, and Sasan Fathpour, "Tunable dual-channel ultra-narrowband Bragg grating filter on thin-film lithium niobate," Opt. Lett. 46, 2730-2733 (2021)

Abstract— We demonstrate dual-channel phase-shifted Bragg grating filters in the tele-com band on thin-film lithium niobate. These integrated tunable ultra-narrow linewidth filters are crucial components for optical communication and sensing systems, as well as future quantum photonic applications. Thin-film lithium niobate is an emerging platform suitable for these applications and has been exploited in this work. The demonstrated device has an extinction ratio of 27 dB and two channels with close linewidths of about 19 pm (Q-factor of 8×10^4), separated by 19 GHz. The central wavelength could be efficiently tuned using the high electrooptic effect in lithium niobate with a tuning factor of 3.83 pm/V. This demonstration can be extended to tunable filters with multiple channels along with desired frequency separations and optimized tunability, which would be useful for a variety of complex photonic integrated circuits.

2.1 Introduction

Integrated Bragg grating filters (BGF) have been attractive for optical communication systems [77, 78], microwave photonics [79, 80], optical signal processing using programmable filters [81] and optical delay lines [82]. A phase-shifted (PS) BGF possesses a narrow transmission peak, or multiple peaks, inside the stopband. A PS-BGF can provide an

unprecedented filtering response with sub-nm linewidth and high extinction ratio (ER). These features render them as fundamental building blocks in high-sensitivity optical sensing [83, 84], quantum photonics [85] and electrooptic (EO) modulation [86]. Tuning the response of these filters through the EO effect [87], the thermo-optic (TO) effect [88] or free-carrier modulation [81], adds another degree of freedom and extends their applicability to high-precision and high-performance integrated systems.

EO-tunable PS-BGFs can offer much higher bandwidth, less power consumption, and lower optical loss than the other mentioned techniques. Obviously, a suitable platform on a material with a high EO effect is required. Thin-film lithium niobate (TFLN) on silicon [8, 38] stands as a superior candidate for modern integrated photonics due to its unique and unparalleled properties, for instance, its strong EO coefficient ($r_{33} \approx 31$ pm/V), and high index-contrast waveguides (~ 0.7). Thanks to the ultracompact waveguides achievable on this thin-film platform, the technology has been utilized for demonstrating a plethora of high-performance electro-optic, nonlinear-optic and quantum-optic devices [38, 89, 90].

Implementation of BGFs on TFLN adds a critical building block to the available component library and facilitates the realization of advanced photonic integrated circuits (PICs) on this versatile platform. Uniform [91, 92] and PS [93, 94] BGF have been previously demonstrated on TFLN. These filters demonstrate zero-, first- or high-order resonance configuration in which they introduce zero, one, or multiple channels, respectively, inside the stopband. Separation of various channels, i.e., the free-spectral range, can be controlled by the length of the cavity formed by the PS section and the grating mirrors, similar to Fabry-Perot (FP) etalons. However, such FP-like filters are not quite suitable for precise-channel filtering of correlated photons [95, 96, 97]. For instance, in spontaneous parametric down-conversion experiments, two precisely and symmetrically separated

ultra-narrowband channels (around twice the pump wavelength) are critically needed for symmetric filtering of correlated signal and idler waves. Such filtration could be achieved by using programmable pulse-shapers [95, 96]. These pulse-shapers are, however, bulky and can only be used in large lab setup demonstrations.

Integrated BGFs on TFLN with two or multiple transmission channels in the stopband have been demonstrated [93]. This is achieved through higher-order resonances in longer phase-shift sections. However, similar to FP filters, these BGFs do not provide flexibility and control over the channels' exact wavelength and separation.

2.2 Operation Principle and Design

In this work, we demonstrate true tunable dual-channel PS-BGF on TFLN. This novel approach is based on three uniform grating waveguides with identical periodicity but a different length for the middle one (see Figure 2.1(b)). This length difference controls the separation of the two distinct channels in the stopband. Furthermore, two phase-shift sections with different lengths are inserted between the grating sections that control the central wavelengths of the channels, independent of the channel spacing.

The two channels, at the 1550 nm wavelength range, are designed to have a separation of $\Delta f = 20$ GHz and similar linewidths of $\delta\lambda = 10\text{-}20$ pm, corresponding to a quality factor up to 1.5×10^5 . The 20 GHz separation represents a reasonable performance metric consistent with achievable optical modulation bandwidths on TFLN for further processing of the filtered signals. Also, the designed linewidth values are chosen for future photon-pair filtering in quantum PICs[342]. It is also noted that the filter is designed for a bandwidth (stopband) of at least a few nanometers at the telecom wavelength range with more than

a 20 dB ER.

The device, shown in Figure 2.1, also enables EO tuning of the central wavelength while keeping the separation between the channels and their transmission ratio consistent with the unbiased case. This is critical for the application of these filters in highly accurate quantum measurements and optical communication, where fine adjustment of the wavelength is needed.

The three-dimensional (3-D) schematic of our filter structure is presented in Figure 2.1(a). The device consists of a Bragg grating with period of Λ and the corrugation depth of $\Delta w = (w_2 - w_1)/2$ around the waveguide width w_g , where w_1 and w_2 are the grating widths at the narrow and the wide part of the grating, respectively. Two phase-shift sections are introduced inside the grating with lengths L_1 and L_2 and separated by a grating section with N_2 periods. N_1 grating periods are used for the input and output gratings. The phase shift sections have a width of $w_g + 2\Delta w$, which helps achieving resonance peaks with a narrower bandwidth.

The device was demonstrated on an X-cut TFLN wafer with the cross-section shown in Figure 2.1(c). X-cut LN enables the utilization of the highest EO coefficient of LN; $r_{33} = 31$ pm/V. We use a directly etched LN waveguiding structure with a shallow etch-depth of 100 nm out of the 300-nm-thick LN layer to decrease the propagation loss through minimizing the overlap with the sidewalls. A scanning-electron microscopy (SEM) image of the fabricated device is shown in Figure 2.1(d). More details on the fabrication process can be found elsewhere [98].

The waveguide has a tight optical-mode confinement, as evident from the transverse-electric (TE) optical-mode simulation shown in Figure 2.1(c). This enables bringing the electrodes closer to the waveguide while avoiding the metal-induced optical loss. We

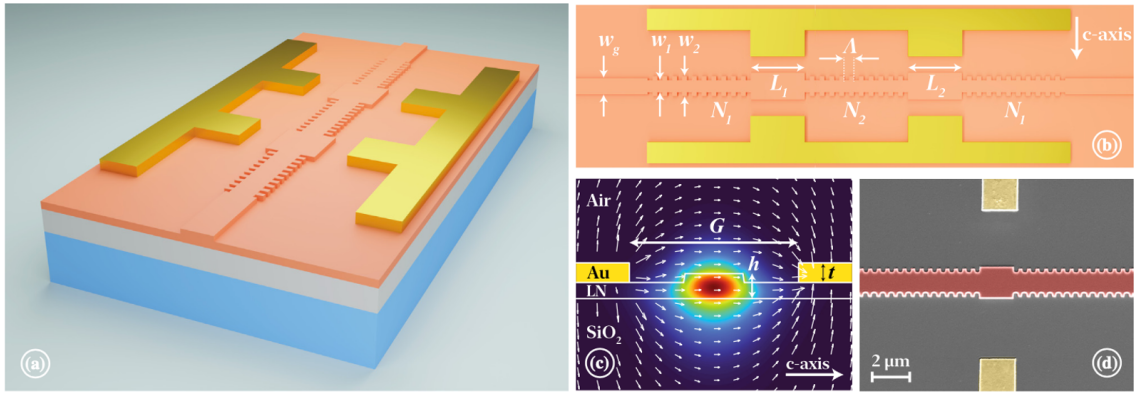


Figure 2.1: (a) 3-D schematic of the tunable dual-channel PS-BGF; (b) Top-view of the device schematic is showing the different design parameters (c) Cross-section view of the waveguide at the non-corrugated region, showing the waveguide dimensions and the different materials. The COMSOL simulation of optical TE mode (at 1550 nm) and DC electric field (arrows) from the electrodes are superimposed; (d) False-color SEM image of the fabricated structure around one of the phase-shift sections, showing the fabricated grating (red) and the surrounding metal electrodes (golden).

chose to keep the gap between the electrodes at $7.5 \mu\text{m}$ to minimize the losses as much as possible while still having enough DC electric field (arrows in Figure 2.1(c)) overlap with the optical mode for EO tuning.

The Bragg wavelength can be adjusted around 1550 nm through the Bragg grating period, Λ [91, 99]. The bandwidth ($\Delta\lambda$) is proportional to the coupling coefficient of the grating ($\kappa \cong 2\Delta n/\lambda_B$), for a long grating in the strong coupling regime [100], where Δn is the difference between the effective refractive indices at the wider and narrower parts of the grating. Therefore, increasing the corrugation depth, and hence Δn , results in increasing the bandwidth and enhancing the ER through the increase of the peak reflectivity, $R_p = \tanh^2(\kappa L)$ [100]. The grating length has a direct impact on increasing the ER [92] and enhancing the linewidth (Q-factor) of the transmission peaks in PS-BGFs.

The eigenmode expansion (EME) method in Lumerical simulation tools simulates the de-

vice performance and achieves optimum design parameters. The EME optical simulation result is shown in Figure 2.3 (green dotted line) for a device with the design and performance parameters given in Table 2.1. Δf is controlled by the number of periods between the two-phase sections, N_2 , whereas the position of the channels could be accurately controlled by changing the length of the PS sections, L_1 and L_2 .

Finally, the EO tuning is simulated through calculation of the overlap between the optical mode and the DC electric field from COMSOL Multiphysics simulation, as shown in Figure 2.1(c). The variation of the TE-mode effective index, Δn_{TE} , through the EO effect can then be calculated from:

$$\Delta n_{TE} = \frac{n_e^3 r_{33} V_a \Gamma}{2G} \quad (2.1)$$

where n_e is the extra-ordinary index of LN, V_a is the applied bias, G is the electrode gap, and Γ is the overlap integral between the optical mode and the DC electric field. The fabricated device with $G = 7.5 \mu\text{m}$ and metal thickness of 130 nm would result in $\Delta n_{TE} \sim 2 \times 10^{-3}$ at 250 V. Further optimization of the EO design (decreasing G and improving Γ) can enhance the EO tuning, the metal-induced losses notwithstanding.

2.3 Experimental Results and Discussion

The fabricated BGF was characterized using the setup shown in Figure 2.2. The amplified spontaneous emission (ASE) from a semiconductor optical amplifier (SOA) is used as a wideband input signal with a 3-dB bandwidth of 85 nm at a biasing current of 500 mA and a controlled temperature of 25°C. The filter's transmission spectrum is measured using an optical spectrum analyzer (OSA), with a minimum resolution bandwidth of 20 pm. Besides, a continuous-wave (CW) tunable laser source with 0.1 pm tuning resolution and

a high-speed InGaAs photodiode, coupled to a digital oscilloscope, are used to capture the fine details of the filter's channels with a resolution better than the employed OSA. A polarization controller is used at the input to excite the fundamental TE mode inside the TFLN waveguides. The light is coupled in and out from the polished facets of the chip using anti-reflection-coated lensed fibers. A DC voltage supply followed by a 100× piezo amplifier is used to provide the needed bias to EO-tune the devices, providing on-sample electric fields as high as 50 kV/mm.

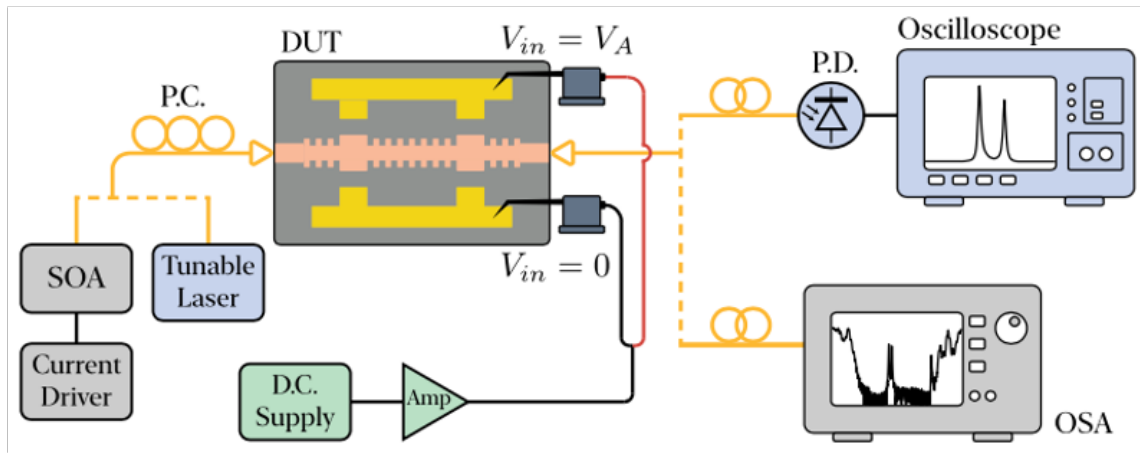


Figure 2.2: A schematic diagram of the characterization setup. SOA: semiconductor optical amplifier; PC: Polarization Controller; P.D: Photodiode; OSA: Optical Spectrum Analyzer; DUT: Device Under Test.

We measured a total insertion loss as low as -8 dB. The propagation loss of 0.2 dB/cm is measured on unmodulated waveguides. The Bragg grating has a length of 1.1 mm, while the total device length is ~ 8 mm. The excess device length (~ 6.9 mm) may be eliminated when integrating these filters with other components. This makes them an attractive compact alternative for high-density PICs.

The measured optical spectrum in the C-band is shown in Figure 2.3 (black solid line). The experimental results are evidently in good agreement with the EME simulation. Ta-

Table 2.1: Performance comparison between design and measurement of a PS-BGF with $w_g = 1.3 \mu\text{m}$, $\Delta w = 100 \text{ nm}$, $\Lambda = 458 \text{ nm}$, $N_1 = 700$, $N_2 = 600$, and $L_1 = L_2 = 82 \mu\text{m}$; $\Delta\lambda$: Bandwidth of the stopband; $\delta\lambda$: Linewidth of the transmission peaks; Δf : Frequency separation between the two peaks; ER: Extinction ration of the stopband edge; δP : Peak power penalty

	$\Delta\lambda(\text{nm})$	$\delta\lambda(\text{pm})$	$\Delta f(\text{GHz})$	ER (dB)	$\delta P(\text{dB})$
Design	3.8	11	21.8	40	-2.5
Measurement	4.0	19	19	27	-6.0

ble 2.1 summarizes and compares the performance parameters of the fabricated device to the simulation. The small mismatch between measurement and simulation can be attributed to the imperfections in the fabrication process. The difference in the peaks power penalty coefficient, δP , and the linewidth of the transmission peaks may be attributed to sidewall and fabrication-induced surface scattering loss in BG waveguides, which are not accounted for in the simulations.

A high-resolution measurement of the resonance peaks in linear scale using the mentioned CW tunable laser, high-speed photodiode and oscilloscope is shown in the inset of Figure 2.3, with better resolution than the OSA-based data. $\delta\lambda = 19 \pm 1 \text{ pm}$ and $\Delta f = 19 \text{ GHz}$ are recorded using this technique, corresponding to a quality factor of 8×10^4 . The ER is 27 dB at the filter's band edge and 13 dB between the peaks due to the limited linewidth of the peaks. This value can be enhanced for filters designed with narrower linewidths.

The shift of the measured central wavelength (1559 nm) from the designed value (1550 nm) is likely due to an etch depth of $\sim 110 \text{ nm}$ in fabricated devices, which is slightly higher than the design value (100 nm). Other attributions could be fabrication tolerances in the grating period and thin-film nonuniformity. The evident sensitivity of the filters

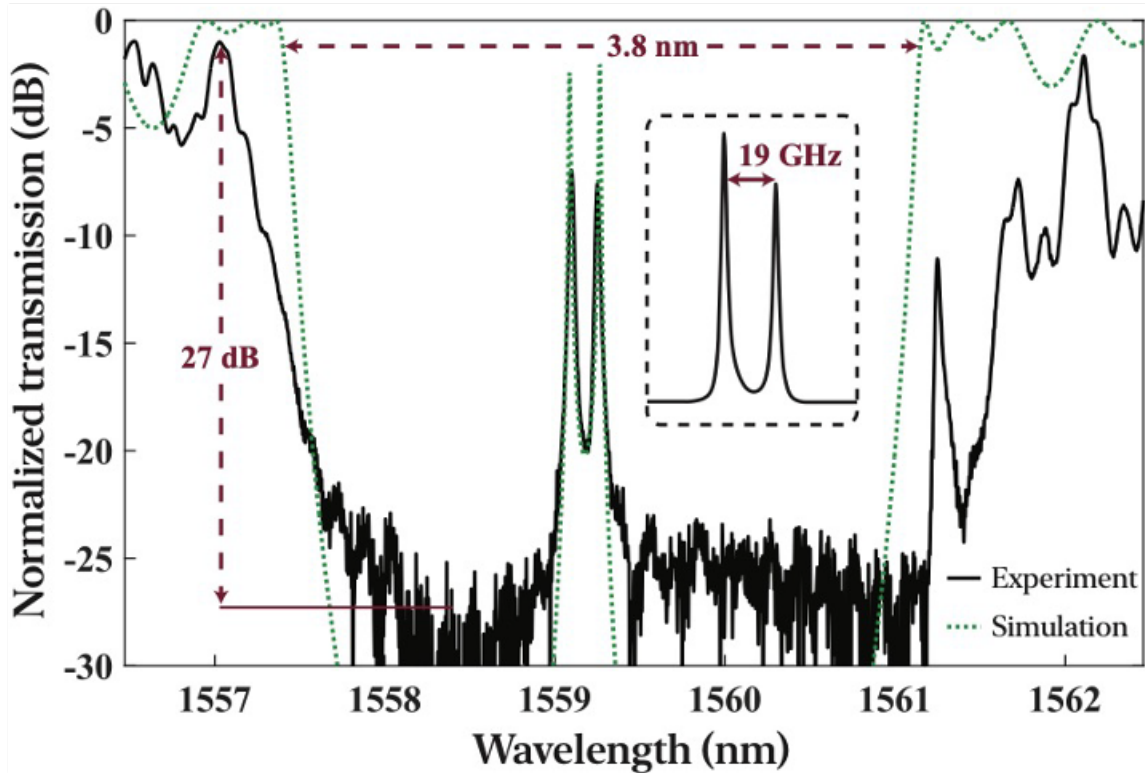


Figure 2.3: Normalized transmission spectrum of the filter from both experiment (black, solid) and simulation (green, dotted), demonstrating a good agreement. The inset shows a high-resolution measurement of the peaks (linear scale) using a high-speed photodiode and a synchronized digital oscilloscope.

to design and fabrication tolerances highlights the importance of having a tuning mechanism for the central wavelength.

2.4 Electro-Optical Tuning of Central Wavelength

The optical transmission spectrum of the filter is recorded for different V_a , as shown in Figure 2.4(a), demonstrating an EO-tuning sensitivity of 3.83 pm/V. With more optimized designs and fabrication, at least 3× improvement is expected, on par with prior reports

[94]. Even higher EO tuning of up to 25.1 pm/V can be achieved [92, 93], but at the cost of increased propagation loss, which cannot be tolerated for quantum-photonics applications.

A small change in the peaks' transmission spectrum is noticed, especially for high applied voltages. This may be attributed to the slight change of the effective indices in the regions outside the phase-shift sections ($\sim 1 \times 10^{-4}$), due to the excessive electrical field coming from the electrodes and the fringing field. The high applied DC voltages may also result in heating of the TFLN, due to potential leakage current, which would result in an effective change of the refractive index. Any field distribution mismatch between the PS sections, due to fabrication or biasing setup, would also result in a relative change between the measured peaks when the high voltage is applied.

The central wavelength is plotted versus the on-chip electric field at steps of 10 V and shown in Figure 2.4(b) (green circle markers), following a linear curve fitting (red line). The performance drifts significantly from this linear relationship and starts to saturate at electric field values of $\sim 22\text{-}24$ kV/mm, which is higher than the coercive field of LN (~ 21 kV/mm) at which the polarity of crystal domains is inverted.

In conclusion, we have demonstrated dual-channel EO tunable ultra-narrowband optical filters using PS-BG structures. The fabricated device demonstrates an ER of 27 dB and a bandwidth of 3.8 nm. The dual channels have a linewidth of 19 pm and a quality factor of 8×10^4 and are separated by 20 GHz. The central wavelength of the filter can be tuned using the EO effect in TFLN with a tuning factor of 3.83 pm/V, which can be beneficial for fine-tuning of high-precision photonic integrated circuits. The measured performances are in a good agreement with design and simulations. These filters can be incorporated into advanced PICs for quantum-photonics applications in the near future. The same

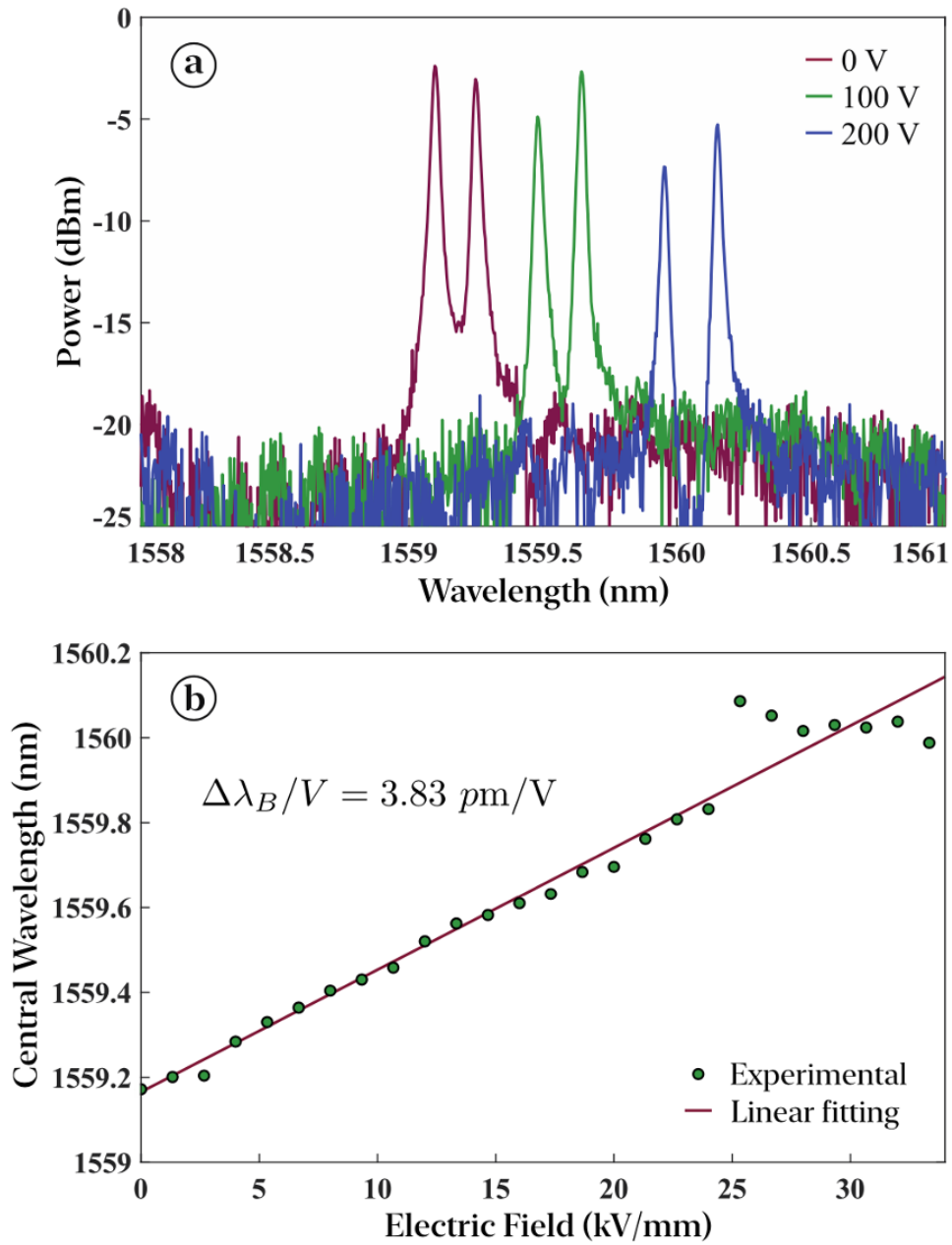


Figure 2.4: Characterization of EO tuning of the PS-BGF, showing (a) filter's transmission spectrum shift at three applied voltage values; (b) Central wavelength shift as a function of the electric field.

concept can also be extended for the realization of multiple-channel ultra-narrowband filters with different and adjustable frequency separations for optical communications applications.

CHAPTER 3: HIGH-SPEED ELECTRO-OPTIC MODULATOR

The contents of this chapter have been submitted as: Farzaneh Arab Juneghani, Milad Gholipour Vazimali, Jie Zhao, Xi Chen, Son Thai Le, Haoshuo Chen, Ehsan Ordouie, Nicolas K Fontain, and Sasan Fathpour, "Non-symmetric high-speed (>100 GHz) thin-film lithium niobate modulator for signal modulation up to 240 Gbits⁻¹," Submitted (2022)

Abstract- High-speed modulators with low driving voltage, low loss, and compact size are essential for future optical communication systems. Thin-film lithium niobate modulators have met each of these criteria separately, but simultaneous achievement of all of them has been challenging on this platform. Low driving voltage electro-optic modulators necessitate either a narrow gap between the electrodes or an elongated Mach-Zehnder arms, both of which adversely affect the microwave loss, hence the bandwidth. Here, this trade-off is alleviated by placing the optical waveguides non-symmetrically with respect to the electrodes and by including a dielectric buffer layer beneath the electrodes. Exploiting this novel design yields a modulator with a measured roll-off of only 2 dB from low frequencies up to 100 GHz, and with an extrapolated 3-dB bandwidth of 170 GHz. The measured voltage-length product of this subterahertz device is 3.3 V.cm. Another device, optimized for a lower voltage-length product of 2.2 V.cm, exhibits a 3-dB electro-optic bandwidth of 84 GHz. The devices are also tested for eight-level phase-amplitude modulation (PAM-8) and demonstrate data rates of up to 240 Gbit.s⁻¹ at 80 Gbaud, validating that the modulators are a propitious candidate for next-generation optical communication systems.

3.1 Introduction

To reduce the size, cost, and power consumption of current optical communication systems and to meet the requirements of future networks, it is crucial to develop modulators with high speed, low driving power, low loss, low cost, and small footprint [101, 102].

Currently, the majority of available commercial modulators are based on silicon (Si) [101, 103, 104, 105], indium phosphide (InP) [106, 107, 108], and bulk lithium niobate (LN) [109]. Despite impressive performance of modulators on these three platforms, none are capable of complying with the required criteria for the next generation of communication systems.

In recent years, modulators based on thin-film lithium niobate (TFLN) have emerged as a promising approach for ultra-high-bandwidth modulators with low driving voltages and small footprint [110, 111, 112, 113, 114, 38, 115, 116, 117]. The optical modes in TFLN waveguides are more compact than conventional LN counterparts, allowing the radio-frequency (RF) electrode spacing to be reduced without causing detrimental optical absorption loss. Consequently, the overlap between the optical and electric fields increases, resulting in a lower driving voltage. Furthermore, using a substrate with a lower dielectric constant than bulk LN makes velocity mismatch between optical and electric fields easier, and thus improving bandwidth [118]. Another factor that can enhance the optical bandwidth is by increasing the thickness of the SiO₂ insulating layer under the thin films in order to optimize the velocity mismatch [112]. Despite the inherent advantages of the TFLN platform, a delicate design is required to reach very high-performance modulators. In a prior work, it was shown that increasing the spacing between electrodes can minimize the RF loss, a key parameter in determining the bandwidth at the expense of increasing the half-wave voltage, V_π [119].

Various TFLN modulators have been reported to expand the 3-dB bandwidth of a single modulator up to 100 GHz and higher [111, 112]. One method is to use a large gap between the electrodes, which leads to a bandwidth of more than 100 GHz, but with a $V_\pi > 13$ V [111], due to the weak overlap between the electric and optical fields inside the gap. Another approach is to utilize asymmetric arms in a Mach-Zehnder modulator (MZM) and to operate at a null point of the transfer function. This approach, however, limits the operating wavelength and is sensitive to fabrication errors [112].

The present work proposes a novel design to relieve the trade-off between bandwidth and V_π in order to achieve modulators with ultra-high bandwidth and reasonably low voltage-length product ($V_\pi \cdot L$). This is done by locating the optical waveguides in a non-symmetric position with respect to the metal electrodes and by incorporating a thin dielectric layer under the electrodes. To validate these concepts, experimental results on two modulators with different design parameters are presented. One has an extrapolated 3-dB electro-optic bandwidth of 170 GHz with a $V_\pi \cdot L$ of 3.3 V.cm. Another device demonstrated a 3-dB bandwidth of 84 GHz with $V_\pi \cdot L$ of 2.2 V.cm. Moreover, an 8-level pulse amplitude modulation (PAM-8) up to 240 Gbit.s⁻¹ is demonstrated using these modulators.

3.2 MZM with Non-Centered Positioning of Optical Waveguides

High-speed MZMs in a push-pull configuration with traveling wave transmission lines on TFLN on Si substrate are studied in this work. Impedance matching, velocity matching, and minimal RF loss are three decisive factors in the design of high-speed modulators [119]. Impedance matching can be done by the proper design of the transmission lines. Velocity matching is significantly easier to achieve in TFLN devices compared to conven-

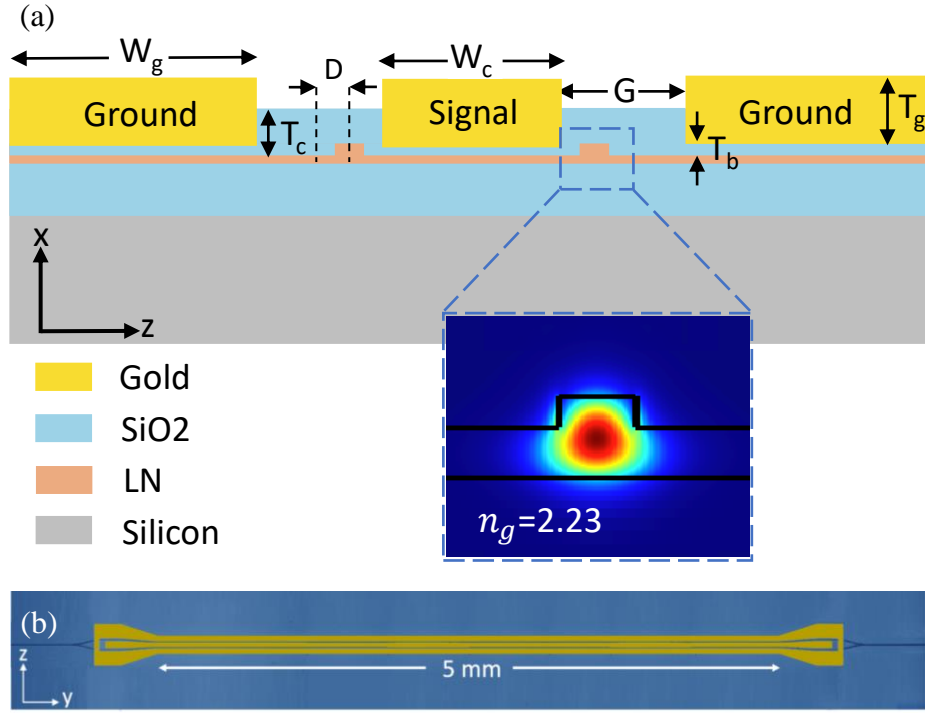


Figure 3.1: (a) Cross-sectional view of the high-speed modulator with non-symmetrical optical waveguides with respect to the electrodes to reduce the drive voltage, and the incorporated dielectric buffer layer to prevent absorption loss. The compact optical mode has a group index of 2.23. (b) Microscopic image of a fabricated TFLN modulator.

tional LN devices, thanks to the low RF-index of the insulating silicon dioxide layer, as well as the silicon or quartz substrates. Certain efforts have been made to minimize the RF loss by increasing the spacing between the electrodes at the cost of larger V_π or by designing segmented electrodes, which makes the velocity matching more challenging [111, 115].

Here, instead of positioning the optical waveguides at the center of the gap between the signal and ground electrodes, they are shifted closer to the signal electrode, whose vicinity has a stronger electric field profile. The parameter D (see Fig. 3.1(a)) denotes the distance between the center of the optical waveguide and the center of the gap between

the electrodes. Accordingly, the spacing between the electrodes can be kept large enough to minimize the RF loss and hence increase the bandwidth, while the electric and optical fields overlap heavily to reduce the V_π of the modulator. The only concern in such an arrangement is the increased optical propagation loss due to the proximity of metallic electrodes, which is mitigated by incorporating a thin silicon dioxide buffer layer beneath the electrodes. This buffer layer also reduces the RF effective index and helps with velocity matching.

In this work, the COMSOLTM Multiphysics software package is used to design and optimize the structure in Fig. 3.1(a) to simultaneously achieve impedance matching, velocity matching and low RF loss. Figure 3.1(a) depicts the cross-sectional view of these modulators. The device layer is a 500 nm-thick X-cut lithium niobate (LN) on an insulator layer on silicon substrate. The rib optical waveguides are 800 nm-wide, which are formed through etching of the LN layer for 200 nm. Other design parameters of two different sets of modulators, later referred to as modulator #1 and modulator #2, are provided in Table 3.1, whose performances are discussed in the next sections.

Table 3.1: Dimension of modulators (μm)

MZM	G	D	W_c	W_g	T_g	T_b	T_c	Length
#1	5	0.6	12	40	1	0.2	0.8	5000
#2	10	2.6	22	40	1	0.2	0.8	5000

The effect of the non-symmetric position of the optical waveguide and inclusion of a buffer layer on the 3-dB bandwidth and required length of MZMs are illustrated in Fig. 3.2. The considered device is assumed to have fixed G and V_π , as well as a limit on optical propagation loss, with values given in the caption and rationalized later in this work. The two main parameters that determine the V_π of a modulator are the length of

the transmission lines and the overlap integral between the optical and electrical fields. Moving the optical waveguide towards the signal electrode, i.e., increasing D , improves the overlap integral and hence the modulator can afford a shorter length for the same V_π . On the other hand, the reduction in length results in a lower RF propagation loss and hence higher 3-dB bandwidth. Additionally, Fig. 3.2 confirms that the embodied buffer layer reduces the overlap integral and degrades the performance of the device up to a certain value of D . However, it lessens the optical loss and thus allows the optical waveguide to be pushed closer to the signal electrode compared to the case without a buffer layer, which ultimately results in shorter devices with higher 3-dB bandwidths.

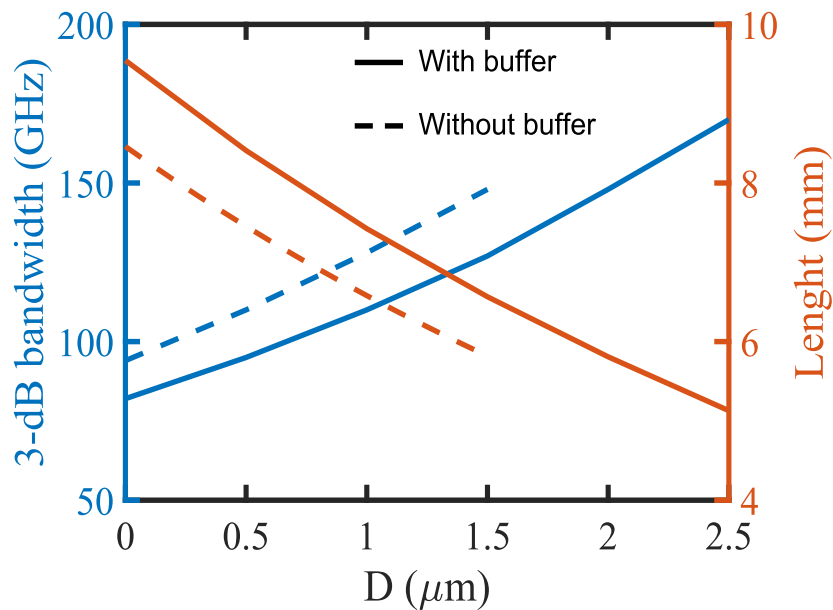


Figure 3.2: 3-dB bandwidth and length of modulator as a function of parameter D with and without a silicon dioxide buffer layer underneath the electrodes for fixed values of $G = 10\mu m$, $V_\pi = 6.6$ V and optical loss of < 0.02 dB/cm. Bandwidth and length of modulator without the buffer layer are not presented for $D > 1.5 \mu m$ because the resulting optical loss is more than 0.02 dB/cm.

3.3 Results and Discussion

3.3.1 Static EO Measurement

The designed devices were fabricated by electron-beam lithography, dry etching, metalization and deposition techniques on a TFLN die. More details on the fabrication steps can be found in Supplement 1. A top view microscopic image of a fabricated device is shown in Fig. 3.1(b). The end-butt coupling method is used to couple the light in and out of the modulators with polished waveguide facets. V_π is measured through a real-time modulation response by applying a 100 kHz triangular voltage sweep. Figures 3.3(a) and 3.3(b) show the detected output signal by a photodetector versus the applied voltage for modulators #1 and #2 in Table 3.1, respectively. The respective V_π are 4.4 V and 6.6 V, which corresponds to a voltage-length product ($V_\pi \cdot L$) of 2.2 V.cm and 3.3 V.cm, respectively. As expected, modulator #1 has a lower V_π owing to its smaller G . Modulators #1 and #2 have an extinction ratio of 23 dB and of 20 dB, respectively. In addition, total insertion loss of these modulators under consideration is about 16 dB, which is mainly dominated by the facet loss.

Figure 3.3(c) investigates the effect of optical waveguide position on the value of V_π for modulator #2 with varying parameter D . In this plot, the V_π values are measured, while the optical losses are simulated using Ansys Lumerical. In the case of $D = 0\mu m$ - i.e., when the optical waveguides reside in the middle of the gap between signal and ground electrodes - $V_\pi = 12.6$ V. Increasing D - i.e., pushing the optical waveguides towards the signal electrode - results in reduced V_π at the cost of increasing optical propagation loss. However, for the case of $D = 2.6\mu m$ with V_π of 6.6 V, the optical loss is still kept below 0.02 dB/cm thanks to the incorporated buffer layer underneath the electrodes.

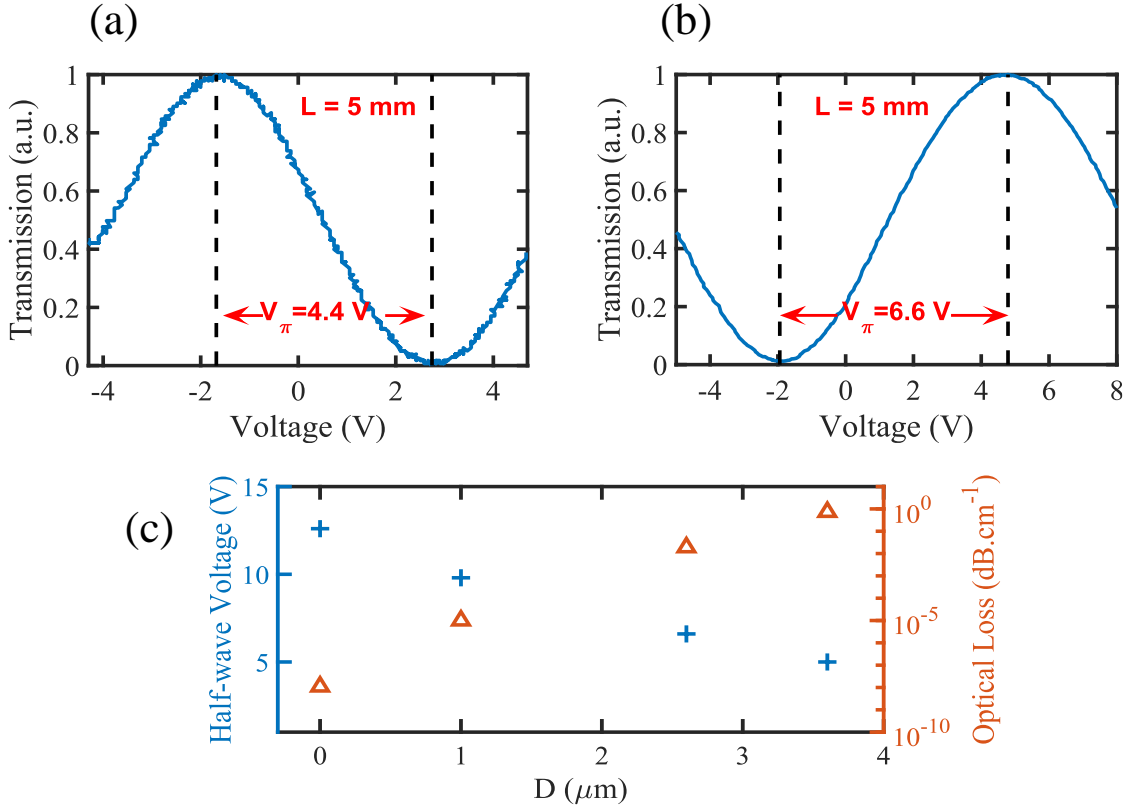


Figure 3.3: Normalized optical transmission of (a) modulator #1 and (b) modulator #2 as a function of the applied electrical voltage, showing V_{π} of 4.4 V and 6.6 V, respectively, for 5 mm-long devices. (c) Variation of V_{π} and optical loss versus the distance between the signal electrode edge and the center of the optical waveguide (parameter D).

3.3.2 Electrical Characterization

Figure 3.4 compares the simulation and measured results for the characteristic impedance, effective index, and loss coefficient of modulator #2 in Table 3.1. The simulations and optimizations, illustrated in red, were done using COMSOL. The experimental values are extracted from the measured electrical S -parameters of the travelling-wave electrodes. These measurements were performed using a Vector Network Analyzer (VNA) and two ground-signal-ground (GSG) probes functioning up to 67 GHz, and were analyzed using

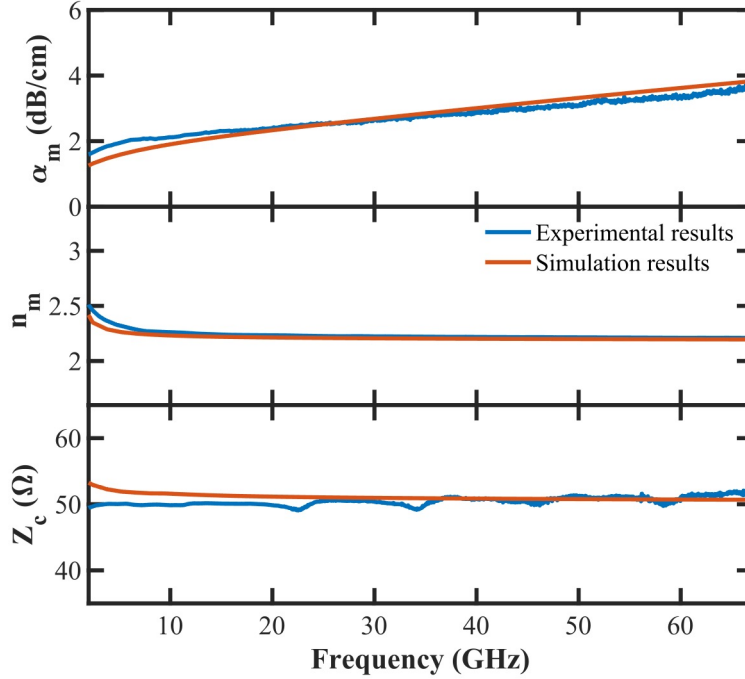


Figure 3.4: Simulation and experimental results of RF loss (α_m), RF effective index (n_m), and characteristic impedance (z_m) of the transmission line as a function of frequency for modulator # 2.

a transmission-line circuit analysis [120, 121]. A great agreement between the simulation and experimental results can be observed in Fig. 3.4. Impedance matching is guaranteed since Z_m is in the range of 49-52 Ω over the RF spectrum. The RF effective index, n_m , is equal to 2.2, which is very close to the optical group index of 2.23 (see the inset of Fig. 3.1(a)) and hence a great velocity matching is achieved for this modulator. The RF loss coefficient, α_m , which represents a combination of conductor and dielectric losses has a reasonably low value of 3.6 dB/cm at 67 GHz or $0.44 \text{ dB}\cdot\text{cm}^{-1}\cdot\text{GHz}^{-1/2}$ due to the relatively large gap of $G = 10\mu\text{m}$ in this device.

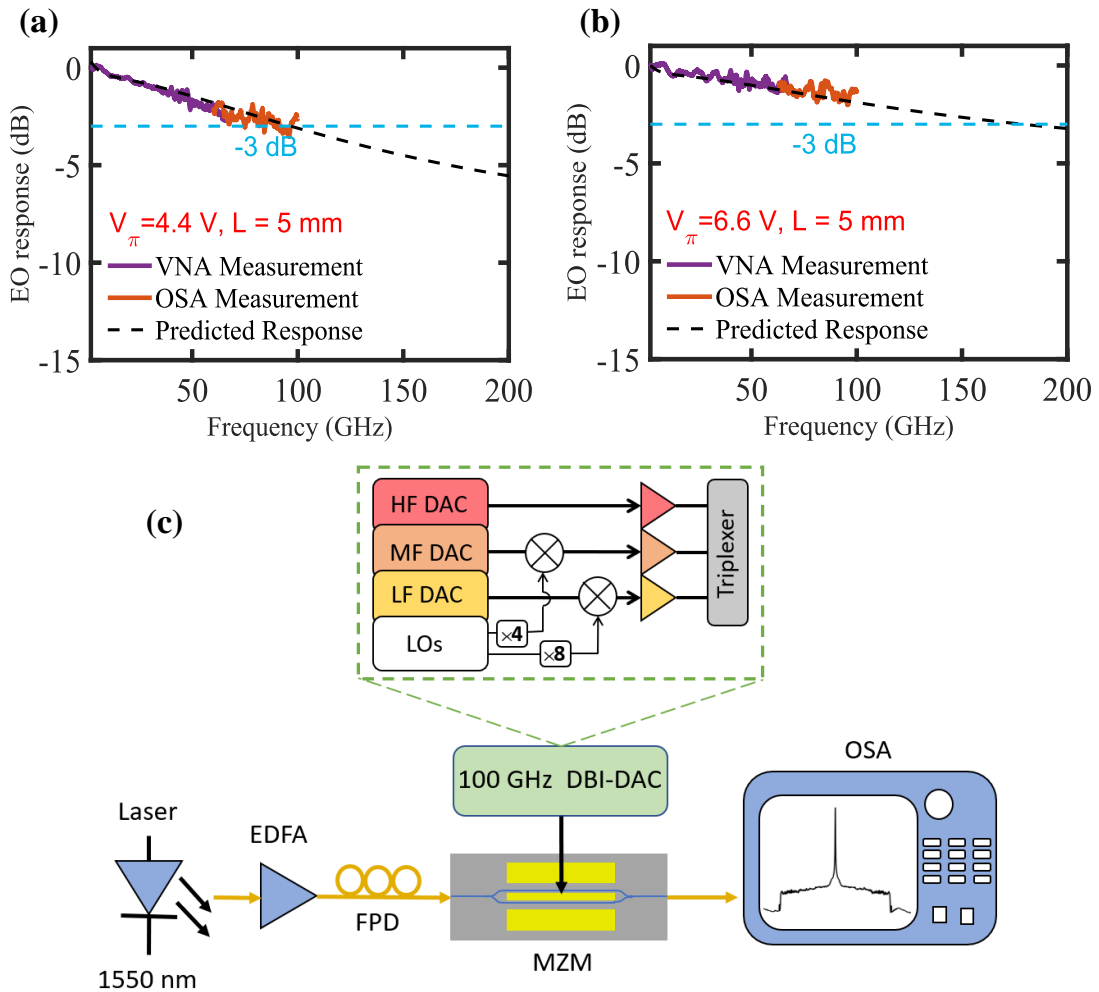


Figure 3.5: Measured EO responses referenced to devices with DC $V_{\pi} \cdot L$ of (a) 2.2 V.cm and (b) 3.3 V.cm, showing ultra-high 3-dB bandwidths of 84 GHz and well beyond 100 GHz, respectively. The EO responses - measured using a vector network analyzer (VNA) up to 67 GHz and an optical spectrum analyser (OSA) from 60 to 100 GHz - are shown with solid violet and orange lines, respectively. (c) Schematic of the experimental set-up for measuring the OSA-based measurements; EDFA: erbium-doped fiber amplifier; FPC: Fiber polarization controller; DBI-DAC: digital-band-interleaved digital-to-analog converter; HF: High frequency; MF: Medium frequency; LF: Low frequency.

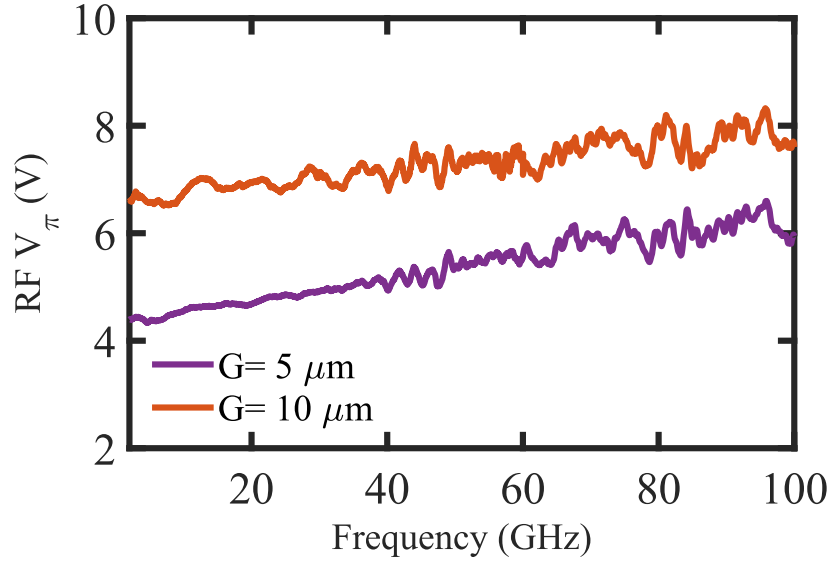


Figure 3.6: Extracted RF V_{π} from EO response shown in Fig. 3.5(a) and 3.5(b) as a function of frequency.

3.3.3 EO Response

Figures 3.5(a) and 3.5(b) demonstrate the characterized EO bandwidth of modulators #1 and #2 in Table 3.1, respectively. To measure the EO response up to 100 GHz at an optical wavelength of 1550 nm, a two-step measurement was performed. The EO response for frequencies below 67 GHz is characterized using lightwave component analyzer (LCA), which includes a calibrated photodetector (PD) and a VNA. In order to apply the RF signal and to terminate the transmission line with a 50- Ω load, two high-speed GSG probes with 67 GHz bandwidth were used at the input and output sides, respectively.

The experimental setup for ultra-high-speed measurement up to 100 GHz is shown in Fig. 3.5(c). The details of this experimental setup are given in Supplement 1.

According to Fig. 3.5(a), the measured 3-dB EO bandwidth of modulator #1, which had

$V_{\pi} \cdot L$ of 2.2 V.cm, is 84 GHz with only 3.6 dB roll-off from low frequencies to 100 GHz. Figure 3.5(b) illustrates that the measured 3-dB EO bandwidth of modulator #2 is well beyond 100 GHz with a roll-off of 2 dB from low frequency to 100 GHz. Using the extracted electrical characteristics and the analytical model described in [122], the EO responses of the two modulators are extrapolated beyond the measurement limit of 100 GHz (see Section 1 of Supplement 1 for details). The simulation results are added to Figs. 3.5(a) and (b). The simulation and experimental results perfectly match up to 100 GHz, thus gives us confidence that the simulations can be trusted to extrapolate the 3-dB modulation bandwidth of device #2. The corresponding 3-dB bandwidth is 170 GHz, as evident in Fig. 3.5(b). This design extends the realm of optical modulators into the subterahertz range of RF frequencies with a low $V_{\pi} \cdot L$ of 3.3 V.cm, which confirms the effectiveness of the proposed and discussed non-symmetric design. Because of the ultra-high bandwidth of this modulator, it is possible to reduce V_{π} much further by increasing the modulator length while still having > 100 GHz bandwidth.

Figure 3.6 presents the RF V_{π} versus frequency for the two modulators, extracted from the measured EO response and DC V_{π} [123]. Modulator #2 with an ultra-high bandwidth of 170 GHz has a $V_{\pi} \cdot L$ of less than 4.1 V.cm up to 100 GHz. This modulator with larger G has less variation in its EO response, as well as its RF V_{π} , over the frequency spectrum owing to its lower RF loss. Conductor loss and hence RF loss decreases in modulators with larger gap due to the lower concentration of current along the electrodes' edges [124]. It has been verified that employing segmented electrodes would help with a more uniform current concentration in the gap of a modulator [115]. The presented design can be easily augmented with segmented electrodes to further reduce the RF loss and consequently push the bandwidth to a greater extent.

3.3.4 Data Modulation

Figure 3.7(a) shows the employed setup for high-speed digital data modulation on modulator #1. The details of the experimental setup are given in Supplement 1.

In the first set of experiments for estimating the data modulation performance of the present devices, a 100 Gbaud on-off keying (OOK) signal was generated and transmitted. The received eye diagram is depicted in Fig. 3.7(b), showing a widely open eye. The bit-error rate (BER) of the captured signal at 100 Gb/s is 8.5×10^{-6} . Next, PAM-4 modulation is carried out at 106.25 Gb/s and 200 Gb/s, resulting in a BER $< 1 \times 10^{-6}$ (error free) and 5.5×10^{-3} , respectively. Furthermore, this high-speed modulator enables transmitting higher data rates up to 240 Gb/s using PAM-8 modulation with a BER of 1.1×10^{-2} , which is within the tolerance of the typical 20% overhead soft-decision forward error correction (SD-FEC) limit of 2×10^{-2} . Overall, the results in Fig. 3.7 indicate the excellent linearity of modulator #1 for high baud-rate optical transmissions. It should be noted that, due to the bandwidth limitation of the employed electronic digital-to-analog converter (DAC), the obtained performance is likely limited by the DAC and driver noise rather than the distortions of the optical modulator.

The energy consumption per bit for data transmission within a traveling wave modulator is proportional to the root-mean-square voltage (V_{rms}) of the driving signal [112]. For PAM-4 modulation at data rate of 106.25 Gb/s, an electrical signal with V_{rms} of 656 mV is applied to the modulator. In this case, the energy consumption of the modulator is estimated to be 81 fJ/bit. To transmit high-speed PAM-8 modulation at data rate of 240 Gb/s, $V_{rms} = 1.23$ V, resulting in an energy consumption of 124 fJ/bit.

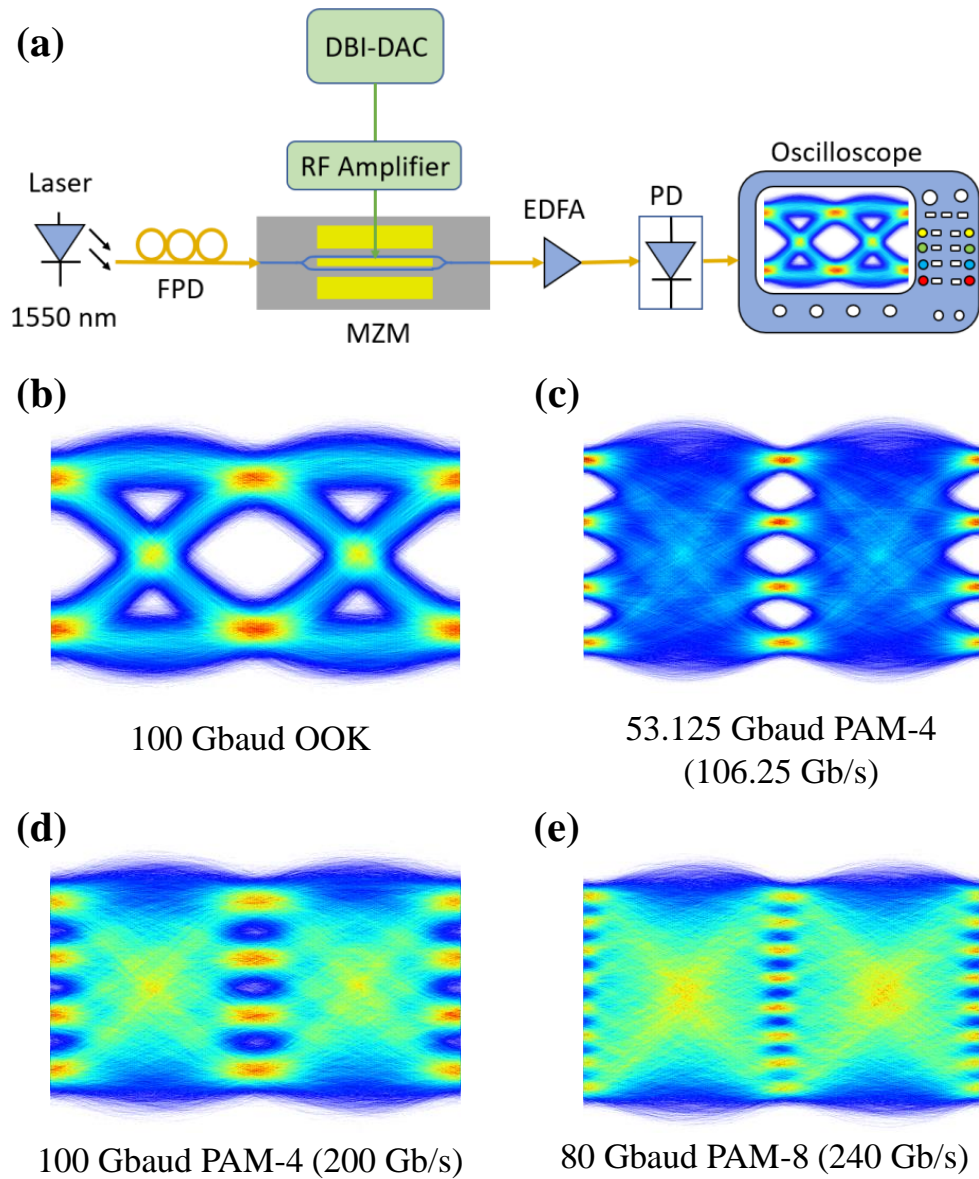


Figure 3.7: High-speed digital data modulation measurements. (a) Schematic of the experimental set-up for the data modulation using 67 GHz real time oscilloscope. Eye diagrams for (b) OOK modulation at data rates of 100 Gb/s. (c), (d) PAM-4 modulation at 53.125 Gbaud (106.25 Gb/s) and 100 Gbaud (200 Gb/s), respectively and (e) Ultra-high speed PAM-8 modulation at 80 Gbaud (240 Gb/s).

3.4 Conclusion

In conclusion, this work demonstrates that the trade-off between bandwidth and V_π of TFLN MZMs can be considerably alleviated by incorporating a buffer layer underneath the electrodes and by pushing the optical waveguides closer to the signal electrode to reduce V_π , while preserving a reasonably large gap between the electrodes to achieve high bandwidth. The experimental results of two modulators with $V_\pi \cdot L$ of 2.2 V.cm and 3.3 V.cm, and with 3-dB electro-optic bandwidth of 84 GHz and 170 GHz, respectively, validate the superior performance of this novel type of modulators. These modulators could transmit 240 Gb.s⁻¹ of data using PAM-8 at 80 Gbaud with minor variation in RF V_π . Given the ease and robustness of fabrication, as well as the integrability with other design concepts, such as segmented electrodes, this design can serve as a model for future optical networks, paving the way for TFLN EO modulators with low voltage and ultra-high-bandwidth in the subterahertz range and the various related digital and analog applications within this frequency range.

3.5 Supplemental Document

This document provides details on the design, fabrication, and experimental setup of high-speed modulators presented in the accompanying paper.

3.5.1 Device Fabrication

In this work, an X-cut lithium thin-film lithium niobate (TFLN) wafer is used with a 500 nm-thick lithium-niobate (LN) layer on 2 μm -thick layer of silicon dioxide on a sil-

icon substrate. First, a 500 nm-thick layer of electron beam lithography (EBL) resist is spin-coated and patterned by e-beam lithography (EBL). Then, the LN thin film is etched for 200 nm in the patterned area through Ar^+ -based inductively-coupled plasma reactive-ion etching (ICP-RIE) to form single-mode optical waveguides. To protect the optical waveguides, 800 nm-thick silicon dioxide cladding layer is deposited by plasma-enhanced chemical-vapour deposition (PECVD). To leave 200 nm of a buffer layer under the electrodes, the oxide layer is partially etched by ICP-RIE at the location of the metal electrodes. Then, EBL resist is used to fabricate the 600-nm-thick gold traveling-wave electrodes through a lift-off process. Finally, the 400-nm thick gold is formed above the electrodes with connected grounds at the in and out ports using the lift-off process. As a result, an 800-nm thick oxide layer remains underneath the section of the electrode that crosses the optical waveguides and connects grounds. This thick layer of oxide can prevent absorption loss from metal electrodes on top of optical waveguides.

3.5.2 Electro-Optic Response of the Modulators up to 200 GHz

The electro-optic (EO) response of modulator #2 in the main text shows about only 2 dB of roll-off from DC to 100 GHz. Higher frequency measurements is limited by the bandwidth of the RF measurement setup. To estimate the 3-dB bandwidth of this modulator, the transmission line parameters, including the RF loss, group index, and characteristic impedance are extracted from the measured S -parameters and utilized to extrapolate the EO response up to 200 GHz, as shown in Figs. 3.8 of the main text. The frequency-modulation response of a TFLN EO Mach-Zehnder modulator can be found as [125]:

$$m(f) = \frac{Z_L + Z_S}{Z_L} \left| \frac{Z_{in}}{Z_{in} + Z_S} \right| \left| \frac{(Z_L + Z_m)u_+ + (Z_L - Z_m)u_-}{(Z_L + Z_G)e^{\gamma_m L} + (Z_L - Z_G)e^{-\gamma_m L}} \right|, \quad (3.1)$$

$$u_{\pm} = (\pm\alpha_m - j\frac{\omega}{c}(n_g \pm n_m))L, \quad (3.2)$$

where Z_L , Z_s , Z_{in} and Z_m are characteristic impedance of the load, generator, RF line input, and electrode transmission line, respectively. n_g and n_m are the optical and RF group index, respectively, α_m is the loss coefficient and L is the active electrode length. The complex RF propagation constant is $\gamma_m = \alpha_m + j\omega n_g/c$, where ω is the RF angular frequency, and c is the speed of light in vacuum. According to Eqn. 3.1, the roll-off frequency can be reduced by velocity matching of the optical and RF waves, minimizing the RF loss, and impedance matching of the load, transmission line, and source.

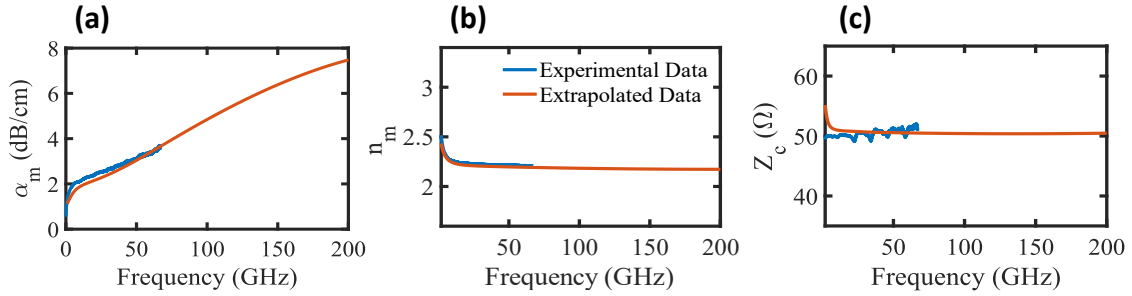


Figure 3.8: Experimental and extrapolated Data of (a) RF loss (α_m), (b) RF effective index (n_m), (c) and characteristic impedance (Z_m) of the transmission line versus frequency.

3.5.3 Ultra-High-Speed Electro-Optic Characterization

The fabricated modulators are driven by a digital-band-interleaved digital-to-analog converter (DBI-DAC) with a 100 GHz analog bandwidth. As shown in Fig 3.5(c) in the main text, the DBI-DAC includes three segments: low frequency/LF, medium-frequency/MF, and high-frequency/HF with ~ 35 GHz bandwidth for each to generate a 100 GHz bandwidth signal. The DBI-DAC is discussed in detail in [126]. The peak-to-peak voltage at

the output of the DBI-DAC is ~ 0.85 V. The modulated optical signal is transmitted to an optical spectrum analyzer (OSA) through a lensed fiber at the optical output. The EO response is calculated through three steps; first, the time-domain waveform of the DBI-DAC, $S_{RF}(t)$, is captured using a 256-GSa/s 113 GHz real-time oscilloscope. Fourier transform is employed to get the RF power spectrum $S_{RF}(f)$. Second, the optical spectrum $S_{Optical}(f)$ at the baseband is determined by subtracting the laser frequency from the measured spectrum on the OSA. Third, the EO response $H_{MZM}(f)$ is calculated from:

$$H_{MZM}(f) = S_{Optical}(f) / \sqrt{S_{RF}(f)} \quad (3.3)$$

Equation 3.3 can be used for the present TFLN modulators, since they operate close to their quadrature point where the cosine transfer function has a slope of ~ 1 . It should be noted that the RF spectrum was captured with ~ 150 kHz resolution, while the optical spectrum was measured with 150-MHz resolution and hence smoothing was done after the division of $S_{Optical}(f) / \sqrt{S_{RF}(f)}$ to mitigate artificial fine features in $H_{MZM}(f)$.

3.5.4 Data Transmission Characterization

According to Fig.3.5(c) in the main text, RF signal was applied using an electronic 120 GS/s 8-bit DAC with a 3-dB bandwidth of 16 GHz and a 6-dB bandwidth of ~ 30 GHz. Due to the bandwidth limitation of the DAC, for generating signal up to 100 Gbaud, digital pre-emphasis was employed to flatten out the output signal spectrum. At 100 Gbaud, the DAC output signal was ~ 100 mV_{pp}. To provide enough voltage swing to the modulator, two RF amplifiers with adjustable gains were cascaded. After optical modulation, the signal was amplified by an erbium-doped fiber amplifier (EDFA), detected by a 70-

GHz photodetector (PD) and then digitized by a 67 GHz real-time oscilloscope for offline digital signal processing (DSP). Offline DSP includes resampling, synchronization, timing recovery and a feed-forward equalizer (FFE) for equalizing the receiver front-end, cable responses and signal reflections due to RF connectors. After equalization, the BER was subsequently calculated by taking into account more than 10 million bits.

CHAPTER 4: MICROWAVE TO OPTICAL CONVERTER

Part of the contents of this chapter has been published in: Juneghani, Farzaneh A., Milad G. Vazimani, Gregory S. Kanter, and Sasan Fathpour. "Integrated Electro-Optical Sensors for Microwave Photonic Applications on Thin-Film Lithium Niobate." In 2021 International Topical Meeting on Microwave Photonics (MWP), pp. 1-4. IEEE, 2021.

Abstract- In-plane integrated electro-optical (EO) sensors have been recently investigated for microwave photonic applications. Here, implementation of these sensors on thin-film lithium niobate (TFLN) on quartz and silicon substrates is proposed and studied. Simulation results confirm the superior performance of such sensors compared to those on previously pursued platforms. A maximum field enhancement (FE) factor of 1100 with 17 GHz bandwidth at the center frequency of 28 GHz is reachable on this platform with the use of a bow-tie antenna. Also, using a patch antenna, a maximum FE factor of 950 can be obtained with a 39 dB difference between the carrier and first sideband intensities for an incident electric field amplitude of 10 V/m. Therefore, by choosing the proper type of antenna, both high-bandwidth and high-sensitivity EO microwave sensors are achievable on TFLN platform.

4.1 Introduction

Recently, there has been a growing interest in employing electro-optical (EO) sensors for transferring wireless microwave/RF signals. These sensors can be employed in various applications such as broadband wireless communication systems and high-speed electromagnetic measurements with high sensitivity [127]. The advantages of an EO sensor,

as a promising candidate for photonic RF front ends, include high bandwidth, negligible E-field perturbation, a fiber-optic interconnection, and compact size [128].

Essential constituents of an EO sensor are a microwave component - which receives the RF signal in the surrounding environment and an optical component, whose properties are altered by the received RF signal. Conventionally, antennas and optical modulators serve as the RF and optical components, respectively, but the two are discrete standalone elements [127]. This separation imposes a requirement on impedance matching of the antenna and the optical modulator in order to transfer the maximum power [129]. However, achieving precise impedance matching is challenging, which causes RF signal distortion [127]. In order to overcome this challenge, in-plane integration of RF antennas and optical waveguides has been recently pursued [127, 130, 131]. In addition, the in-plane integration increases the overlap between the RF and optical fields, which again improves the performance of EO sensors [131].

Several integrated EO sensors have been designed and fabricated using in-plane structures over the past few years [127, 128, 130, 132, 133]. Characterization of these sensors confirm the expected performance improvement. For instance, a tapered antenna array was fabricated on one arm of an asymmetric Mach-Zehnder interferometer (MZI) on bulk lithium niobate (LN) substrate [130]. By using this configuration, the microwave signal can be directly extracted by optical detection. A very wide bandwidth (from 9 kHz to 39 GHz) was reported. In another work and using slotted patched antennas, a first sideband-to-carrier ratio of -22 dB is reported under normal incident field with a power density of 120 W/m^2 [131].

Here, in-plane integration of EO sensors using the thin-film lithium niobate (TFLN) platform is proposed and studied both numerically and experimentally. It is reminded that

TFLN has been extensively explored in the past decade for a variety of EO applications and demonstrated unprecedented performance in applications such as EO modulators [18]. However, to the best of the authors' knowledge, this is the first time that TFLN is being employed for EO microwave sensing applications. Simulation results are very promising and demonstrate that by choosing the proper type of antenna on the TFLN platform, which depends on the application requirements, the performance of these devices can be significantly improved.

4.2 Theory

Figure 4.1 shows the cross-section of the proposed EO sensor. An optical waveguide on the TFLN platform is embedded within the short gap (5 μm) of an antenna. Irradiation of a wireless microwave signal to this device will cause a displacement current, which in turn will induce a strong electric field across the gap. This induced electric field changes the refractive index of the lithium niobate (LN) waveguide due to the strong Pockels effect of the material. The effect of this index variation is optically captured and by post-processing the data, the incident RF electric field can be measured. Here, the antenna can be treated as a phase modulator around the optical waveguide, in which the refractive index variation is calculated as:

$$\Delta n = \frac{1}{2} r_{33} n_{eff}^3 \Gamma E \quad (4.1)$$

where r_{33} is the exploited EO coefficient, n_{eff} is the effective refractive index of the optical mode, Γ is the overlap integral factor between electrical and optical fields in the EO material, and E is the induced electric field across the gap.

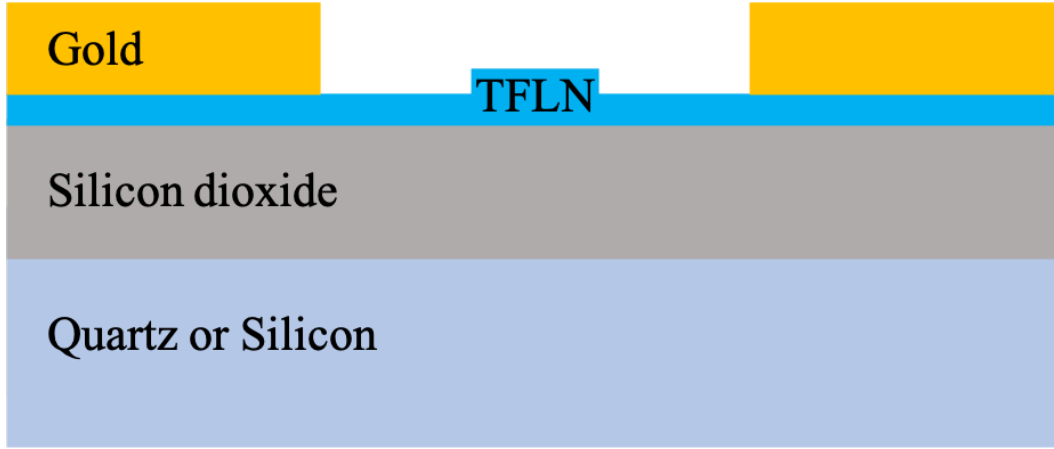


Figure 4.1: Cross-section of an EO sensor on the thin-film lithium niobate platform

The evaluation of these devices can be done through reporting two important parameters: the field enhancement factor and the first sideband-to-carrier ratio. These figure of merits and their relevance to the performance of EO sensors are explained in the following.

4.2.1 Field Enhancement Factor (FE)

The field enhancement factor parameter is defined as the ratio of the electric field amplitude at the center of the gap to the amplitude of the incident electric field [132]:

$$FE = \frac{|E|}{|E_i|} \quad (4.2)$$

Higher field enhancement factor values correspond to an increase of the induced electric field at the center of the waveguide, hence better performance of the device. Based on Equation 4.1, in order to improve the performance and sensitivity of EO sensors, the ΓE product should be increased.

The FE parameter mainly evaluates the performance of the antenna and reveals how good the antenna is in receiving RF signals at the desired frequency. However, the gap of the antenna, which is mainly governed by the optical design limitations, notably affects FE. The bandwidth of an EO sensor is defined as the frequency range, over which the FE drops to ~ 0.7 of its maximum value, corresponding to 3-dB drop in power.

4.2.2 First Sideband-to-Carrier Ratio (FSBCR)

The difference between output and input of the optical waveguide is an effective way to measure the performance of an EO sensor. The analysis can be done in the frequency domain. The optical waveguide is fed with a CW monochromatic laser, which means the spectra of the input consist of one single carrier frequency. If there is no microwave field in the environment, the output spectrum obviously remains intact. In the presence of RF fields, though, the output spectrum will contain a number of sidebands, corresponding to different orders of Bessel functions [134].

As mentioned earlier, the antenna of an EO sensor can be regarded as a phase modulator for the optical fields propagating through the waveguide. Since the modulation depth of these devices is insignificant, the small-signal approximation and the Taylor expansion can be applied on the first-order Bessel function. Therefore, the relationship between the optical intensity at the carrier frequency (I_c) and the first sideband (I_{FSB}) can be obtained as [134]:

$$I_{FSB} = I_c \left(\frac{m}{2}\right)^2 \quad (4.3)$$

where m is the modulation depth and is defined as:

$$m = \pi \frac{V_p}{V_\pi} \quad (4.4)$$

Here, V_p is the peak modulation voltage that is correlated to the FE of the device, and V_π is called half-wave voltage, which is the required voltage to induce a π phase shift on the optical electric field and in the EO material, and given by [134]:

$$V_\pi = \frac{\lambda d}{r_{33} n_{eff}^3 \Gamma L} \quad (4.5)$$

where d is the gap between electrodes, L is the interaction length between RF and optical fields, and λ is the vacuum wavelength of the guided optical mode. High performance EO sensors demonstrate greater values of m , since it corresponds to a larger V_p (or FE) and a smaller V_π or both.

The parameter first sideband-to-carrier ratio ($FSBCR$), as the name suggests, is defined as:

$$FSBCR = \frac{I_{FSB}}{I_{Carrier}} = \left(\frac{m}{2}\right)^2 \quad (4.6)$$

Clearly, higher $FSBCR$ values correspond to better performance of the device and implies that the optical mode is more affected by the antenna. However, m is a very small value for EO sensors and thus, $FSBCR$ is reported in dB units with negative values. Also, it should be mentioned that sometimes this parameter or very similar parameters are called the conversion efficiency in the literature, since it demonstrates how well the RF signal is converted to distortion of the optical mode.

4.3 Simulation and Design

In this work, the performance of integrated EO sensors on bulk LN and TFLN platforms, for both patch and bow-tie antennas, are simulated. However, the figures showing TFLN

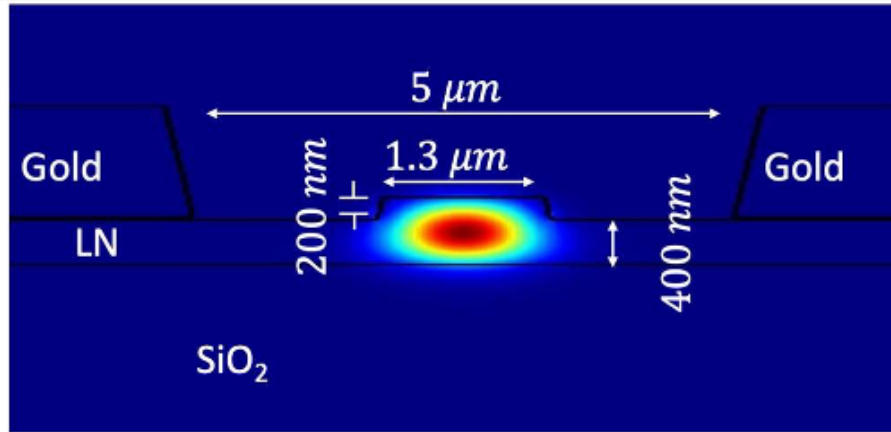


Figure 4.2: Fundamental TE mode of the optical waveguide

simulation results in here correspond to TFLN platform on quartz substrate and simulation results for TFLN on silicon substrate are only included in Table 4.1. Ansys Lumerical was primarily used for optical simulations, while COMSOL Multiphysics was used for microwave/RF simulations.

4.3.1 Optical Waveguide

One of the main advantages of TFLN over bulk LN is the compactness of its optical waveguides. A typical TFLN wafer consists of a 300-600 nm-thick layer of LN with thicker than 2 μm of silicon oxide underneath it, placed on a silicon or quartz substrate. The thin layer of LN with the surrounding index contrast along with the availability of new etching technologies make TFLN capable of having low loss, ~1-1.5 μm-wide rib waveguides with below 250 nm etching depth [43].

In the simulations, an X-cut TFLN wafer with a 600 nm-thick LN layer and 2 μm oxide on a quartz substrate is used. The waveguide is extended along the y-axis of the TFLN wafer

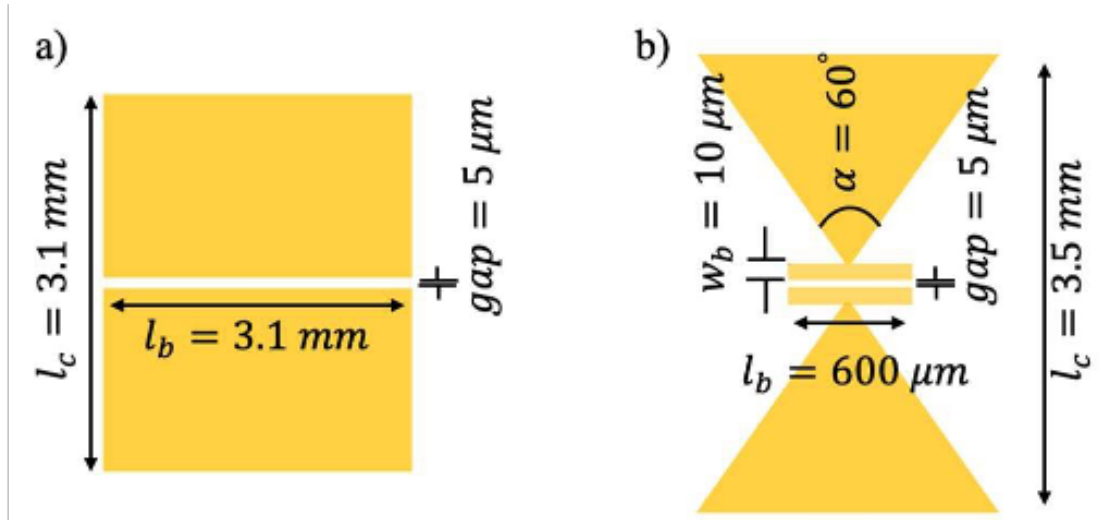


Figure 4.3: Schematic and dimensions of designed a) patch antenna and b) bow-tie antenna for a center frequency of 28 GHz on TFLN on quartz substrate

so that the induced electric field is perpendicular to it and along the z-axis, in order to exploit the highest EO coefficient in LN, r_{33} . An etching depth of 200 nm is assumed in the simulation to form 1.3- μm -wide rib waveguide. Figure 4.2 demonstrates the fundamental transverse electric (TE) mode of the waveguide.

4.3.2 Antenna

In antenna simulations, a planar gold structure is assumed to be deposited on a TFLN wafer. Two types of antennas are simulated in this work, namely, patch antennas and bow-tie antennas. Patch antennas are narrowband antennas, which leverage longer interaction length to improve *FSBCR*. On the other hand, bow-tie antennas provide larger bandwidth while the improvement on the *FSBCR* parameter is not as good as the patch antennas [132, 18]. Therefore, depending on the application requirements, one can choose the proper antenna type for the EO sensors on the TFLN platform.

To achieve sensing in the GHz frequency regime, the antenna needs to be carefully designed and optimized. Figure 4.3 demonstrates the schematic and dimensions of the optimized patch and bow-tie antennas on the TFLN platform on a quartz substrate, operating at the center frequency of 28 GHz. The incident field is assumed to be 10 V/m in all simulations.

4.4 Simulation Results and Discussion

The simulation results, along with reported values from published papers on integrated EO sensors, are summarized in Table 4.1. After the integrated EO sensor on silicon substrate in Ref [132], devices on the TFLN platform on quartz substrate demonstrate the best field enhancement factor, i.e., 1100 and 950 for bow-tie and patch antennas, respectively.

It is noted that the higher value of FE in Ref [132] originates from the very short gap of the device ($1 \mu\text{m}$), which causes high optical loss since the optical mode is not as compact in that platform. To compensate for the high optical loss, a very short interaction length ($50 \mu\text{m}$) was considered for the device, which drastically affected the $FSBCR$ parameter.

Thanks to the compact waveguide and mode size on the TFLN platform, the optical waveguide can reside in a $5 \mu\text{m}$ gap of the antenna while the optical propagation loss can be kept below 0.15 dB/cm, based on the simulation results using Ansys Lumerical. The small gap helps with increasing both FE and $FSBCR$ parameters of the EO sensor through larger amplitude for the induced electric field in the gap of the antenna, and higher Γ values. The distribution of the electric field within the gap, as well as the FE factor versus frequency, are shown in Fig 4.4 and Fig 4.5 for EO sensors on TFLN on quartz substrate with bow-tie and patch antennas, respectively.

Table 4.1: Comparison of performance parameters for EO sensors in microwave applications. First six rows are the simulations results of this work and next four rows are from the literature

Type	EO Material Substrate	Gap (μm)	Interaction length (μm)	Center frequency (GHz)	Bandwidth (GHz)	Maximum FE	FSBCR (dB)
Bow-tie (TFLN)	LN Quartz	5	600	28	11	1100	-50
Bow-tie (TFLN)	LN Silicon	5	600	28	6.5	740	-54
Bow-tie (Bulk LN)	LN LN	10	600	28	3.5	600	-57
Patch (TFLN)	LN Quartz	5	3100	28	4	950	-37
Patch (TFLN)	LN Silicon	5	1600	28	4	645	-46
Patch (Bulk LN)	LN LN	10	780	28	4	280	-60
MA Bow-tie [132]	EO Polymer Silicon	1	50	65	—	1400	-73
Patch [131]	SEO125 GaAs	10	2000	37	2	280	-61
Patch [127]	LiTaO ₃ Silica	5	800	58	2.5	880	-64
Bow-tie [134]	SEO100 Silica	10	1200	10	3	450	-63

It is evident from Table 4.1 that bow-tie antennas on TFLN on quartz demonstrate much wider bandwidth at the same center frequency compared to the same type of antennas on silicon substrate and bulk LN. This is because the lowest frequency of the bow-tie antenna depends on the flare angle and wing length. Therefore, larger bow-tie antennas have wider bandwidths. The size of an antenna is proportional to $1/\epsilon_r$, where ϵ_r is the substrate dielectric constant. Hence, the TFLN platform leverages low- ϵ quartz and

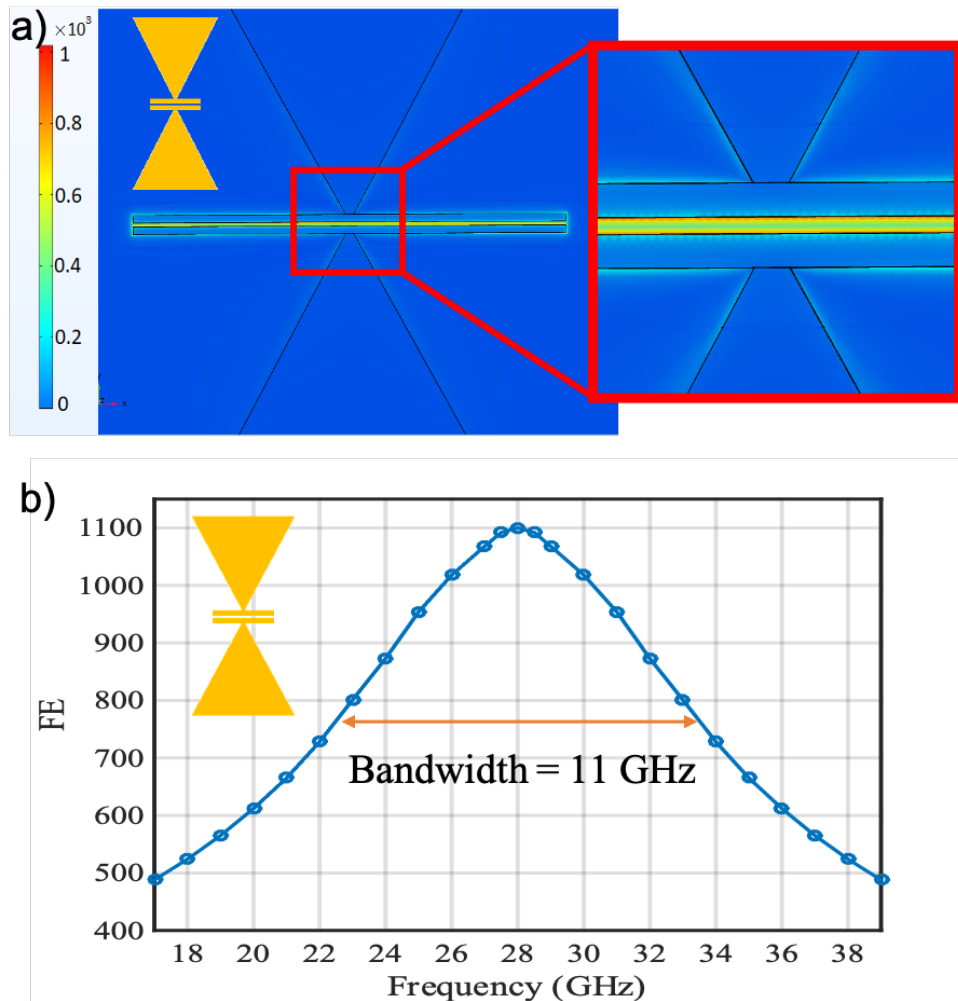


Figure 4.4: a) Electric field distribution within the gap and b) FE versus frequency for the EO sensor on TFLN on quartz substrate with a bow-tie antenna

silicon substrates to afford larger-size bow-tie antennas and improve the bandwidth of the EO sensor.

For the same reason, patch antennas on the TFLN are larger than counterparts on bulk LN, which means they can collect more power and have a longer interaction length. The effect can be seen in both *FE* and *FSBCR* parameters. It is worth mentioning that, EO

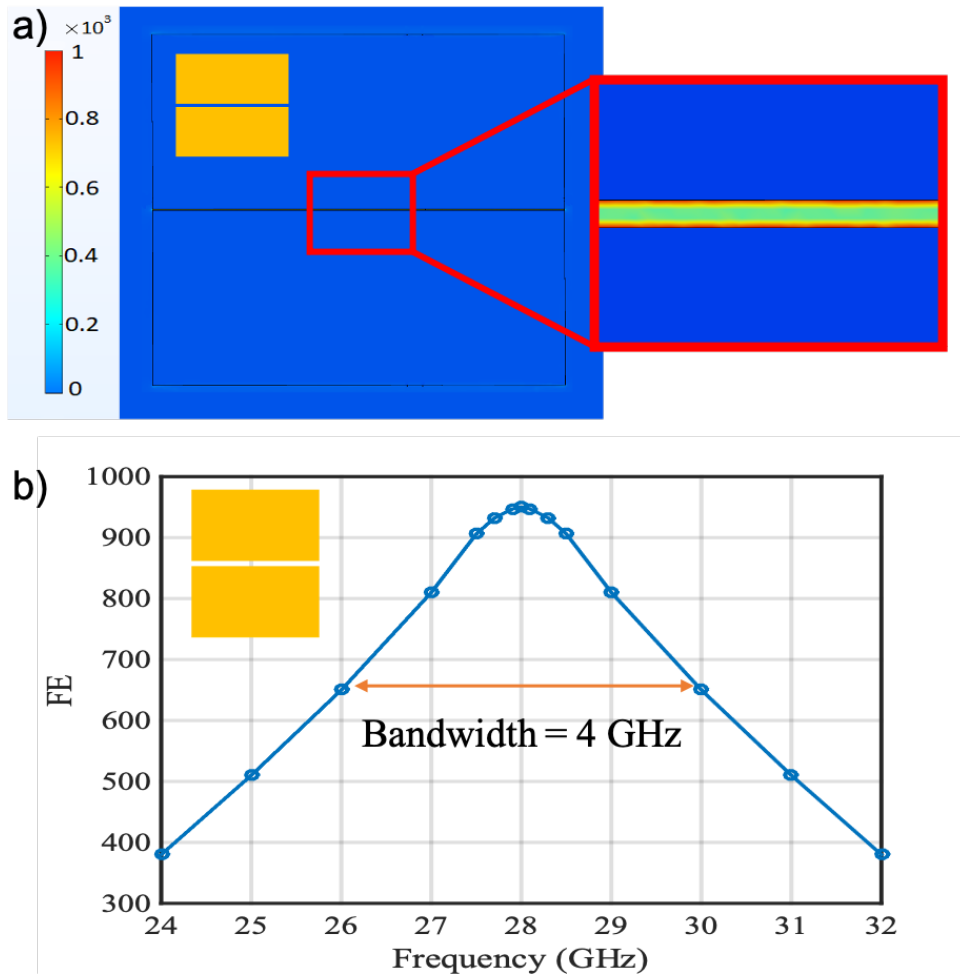


Figure 4.5: a) Electric field distribution within the gap and b) FE versus frequency for the EO sensor on TFLN on quartz substrate with a patch antenna

sensors using patch antenna on the TFLN platform on quartz substrate demonstrate the best *FSBCR* performance, which makes it a very good candidate for sensitive and narrow-band applications.

4.5 Experimental Results and Discussion

As it was discussed before and shown in Table 4.1, devices on TFLN platform on quartz substrate demonstrate the best efficiency and/or bandwidth. However, this project is our first experience in the group working with Quartz substrate, which requires modifications in several fabrication steps including E-beam lithography, etching, dicing, and polishing. As it will be discussed in Section 6.2, we are working on development of these processes for having high-performance devices on TFLN on quartz substrate.

While these developments are in progress, we decided to fabricate these devices on TFLN on silicon substrate, which we have extensive experience of working with them within our group. As shown in Table 4.1 the device performance on silicon substrate is not as good as those on Quartz substrate, but still better than conventional LN and other devices in the literature. These devices can be used for proof of concept as well as for providing performance comparison with the ultimate fabricated devices on Quartz substrate.

TFLN platform with 300 nm-thick LN layer on silicon substrate was used for this project. 1.1 μm -wide rib optical waveguides are patterned on the chip using ZEP-520A E-beam resist and are formed via etching the LN layer for 120 nm. Patch and bow-tie antennas have the dimension of 1.6 mm \times 1.6 mm and 1.8 mm \times 1mm, respectively. Antennas are deposited using E-beam evaporator followed by a lift-off process and consist of 20 nm of Cr to help with the adhesion to the LN layer and 600 nm of gold. Figure 4.6 illustrates the layout and some of the microscopic images of the fabricated patch and bow-tie antennas as well as optical waveguides and ring resonators.

Performance evaluation of these devices require both optical and microwave measurements for optical waveguides and antennas, respectively. This project is in collaboration

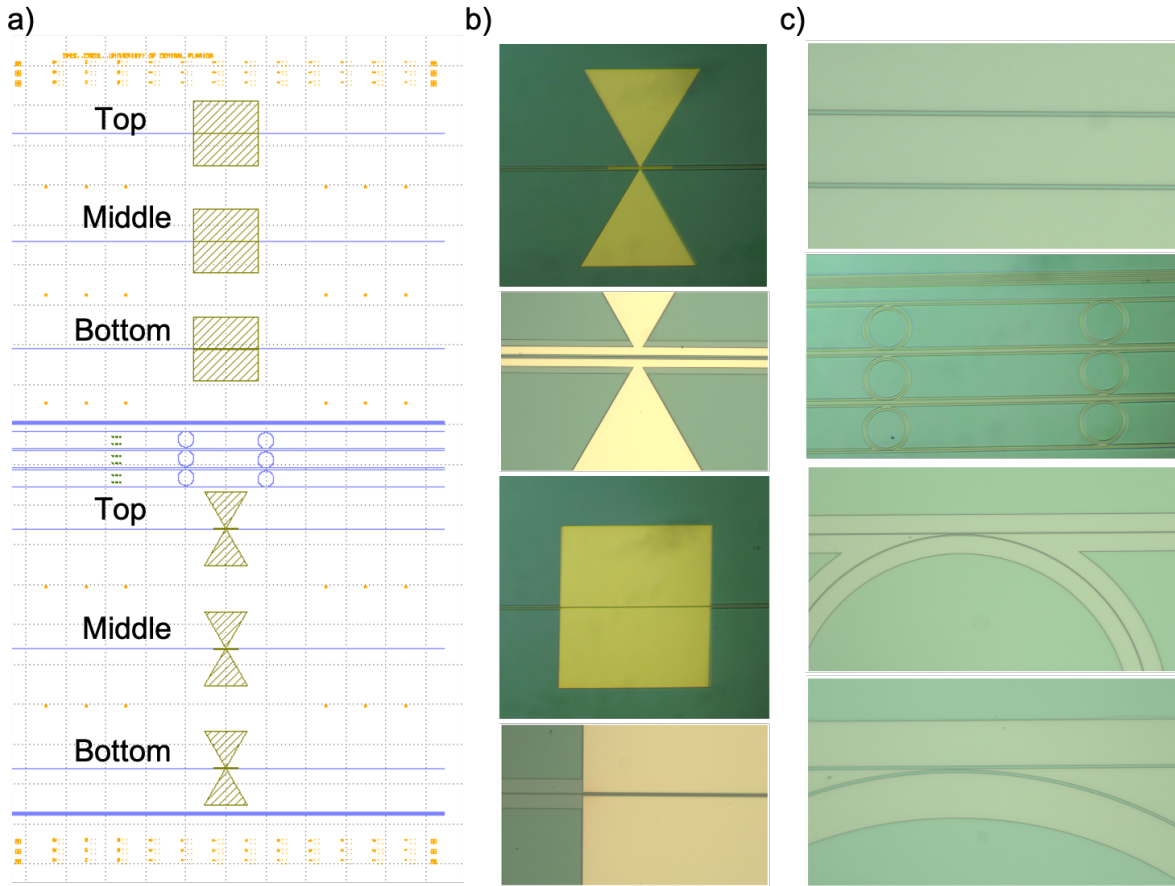


Figure 4.6: a) Mask layout for the fabrication. Some microscopic images of the fabricated b) Bow-tie and patch antennas and c) Waveguides and ring resonators on TFLN platform on Silicon substrate

with NuCrypt company and they will be responsible for microwave measurements. The optical measurement setup is shown in Fig. 4.7(a). Edge-coupling method is used for coupling the light in and out of the chip with single mode fibers. Optical propagation loss is measured through curve fitting to the transmission spectrum of several ring resonators with various gap between the ring and bus waveguide. As shown in Fig. 4.7(b), the propagation loss was measured to be 2.26 dB/cm. Optical measurement results are summarized in Table 4.2. Top, middle, and bottom waveguides for both bow-tie and

patch antennas are indicated on the layout in Fig. 4.6(a).

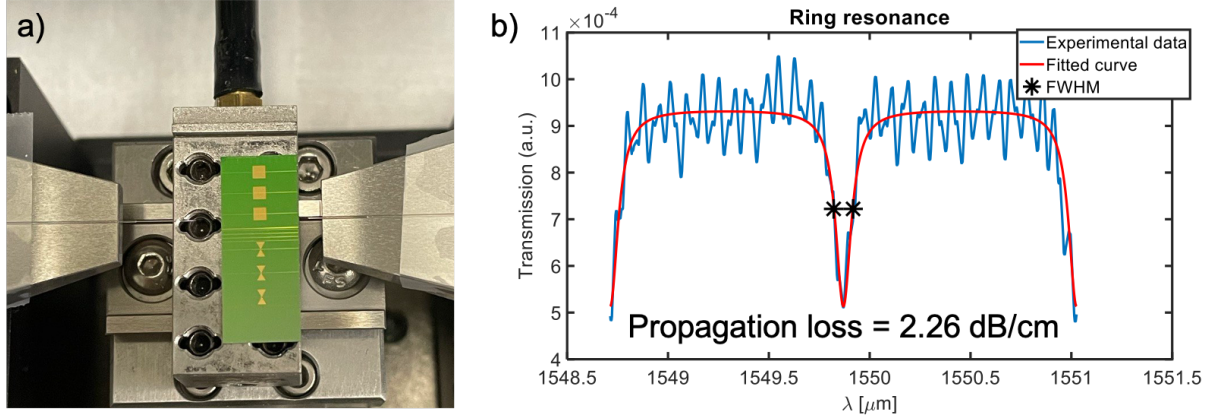


Figure 4.7: a) Optical measurement setup. b) ring resonator measurement result showing 2.26 dB/cm of propagation loss.

Table 4.2: Optical (insertion loss) measurement results for devices on TFLN platform on silicon substrate with input power of 13.5 dBm or 22.5 mW.

Waveguide	Output Power (dBm)	Insertion Loss (dB)
Patch Top	-7.5	21
Patch Middle	-4.5	18
Patch Bottom	-3	16.5
Bow-tie Top	0	13.5
Bow-tie Middle	-0.5	14
Bow-tie Bottom	-2.5	16

Currently, our collaborators at NuCrypt company are working on microwave measurements for these devices. Very recently, they provided us with some preliminary results for the patch antennas. Figure 4.8(a) demonstrates the output optical spectrum with (blue) and without (gray) RF transmit at 28.5 GHz. It is evident that by having the RF power on, two sidebands located 28.5 GHz away from the carrier frequency appear on the spectrum, which correspond to the first order Bessel function of the first kind as a result of phase modulation. Also, this device was polarization sensitive and by rotating the polarized

horn antenna by 90 degrees the sidebands disappear.

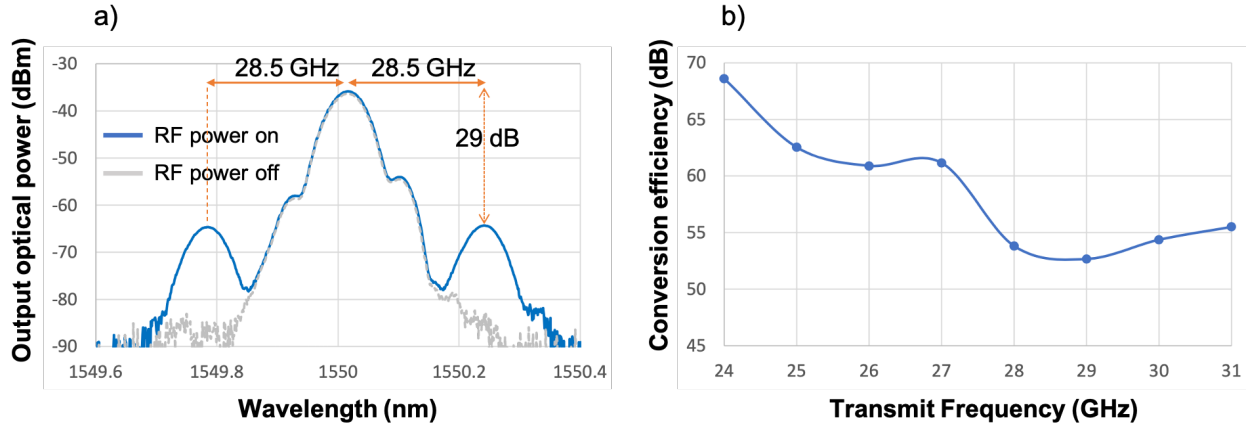


Figure 4.8: a) Output optical spectrum with and without RF power. b) Frequency response of the device.

Figure 4.8(b) illustrates the frequency response of the device. It can be seen that the device operates around the center frequency of 28.5-29 GHz, which is very close to the designed center frequency of 28 GHz. Also, the conversion efficiency at the center frequency is -53 dB, which is only 7 dB less than the designed conversion efficiency of -46 dB. Moreover, the bandwidth of this device is more than 3 GHz, but for the more accurate measurement of the bandwidth, the frequency response measurement after 31 GHz will be conducted.

Figure 4.9 shows the sideband to carrier ratio in dB as a function of input RF power in dBm. As expected, the sidebands are linearly related to the input power. Also, conversion efficiency of -53 dB can be seen on this plot again.

These devices can be used in a photonic down-conversion experiment. The optical output of these devices can be passed through another phase modulator, which is modulated with a local oscillator at a frequency close to the input microwave frequency. Therefore, the sidebands can undergo a down-conversion process and via filtering the carrier fre-

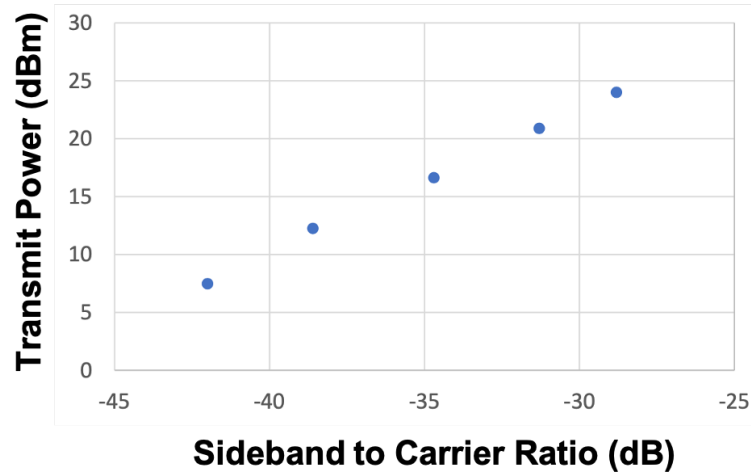


Figure 4.9: Sideband to carrier ratio as a function of the applied RF power.

quency, the down-converted signal can be easily detected without requiring high-speed detectors.

Figure 4.10 demonstrates the results of such a photonic down-conversion experiment, in which the device under test is radiated with a 28 GHz microwave signal and the phase modulator is fed with a local oscillator at 27.5 GHz. Figure 4.10 (a) shows the detected signal at 500 MHz as a result of the down-conversion process. Figure 4.10 (b) exhibits the quadratic relation between the input microwave electric field and the power of the down-converted tone. It's noted that this plot is in logarithmic scale thus the quadratic relation appears as a line with a slope of two.

4.6 Conclusion

The presented results confirm that very high-performance EO sensors for microwave/RF applications are attainable using the TFLN platform on a quartz/silicon substrate. Due

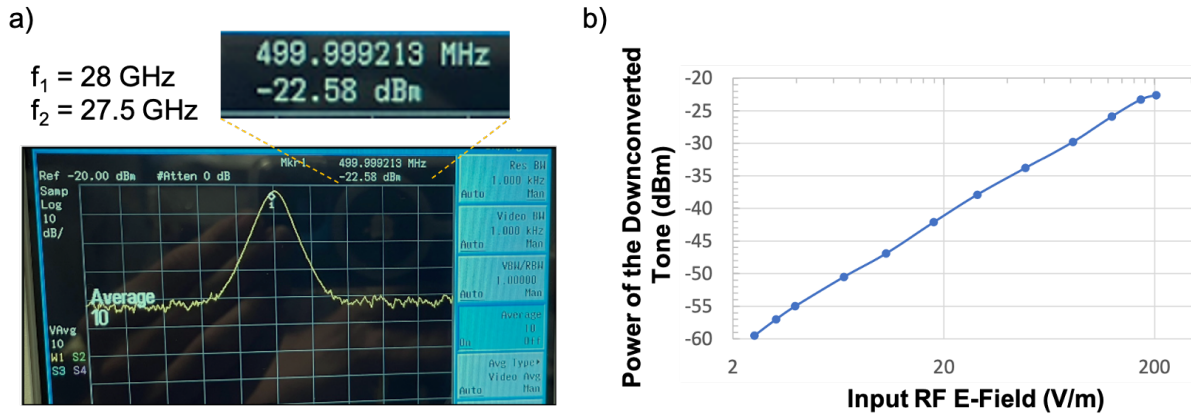


Figure 4.10: Photonic down-conversion experiment results. a) Detected signal at 500 MHz frequency can be observed as a result of down-conversion process. b) Quadratic relation (slope of 2 in the logarithmic scale) between the input electric field and power of the down-converted tone

to the compact waveguide and mode size, and consequently short gap of the antennas on this platform, a high field- enhancement factor is achievable, regardless of the choice of the antenna. Using this platform, EO sensors with bow-tie antennas are an excellent candidate for wideband microwave sensing applications, while EO sensors with patch antennas are more suitable for highly sensitive applications.

CHAPTER 5: NONLINEAR WAVELENGTH TRANSLATOR

5.1 Introduction

Part of the contents of this chapter has been published in: Milad Gholipour Vazimali and Sasan Fathpour "Applications of thin-film lithium niobate in nonlinear integrated photonics," Advanced Photonics 4(3), 034001 (2022).

The goal of this project is to build an all-optical wavelength translation device capable of shifting one C-band optical channel into a different C-band channel. Second-order nonlinear processes can be utilized to achieve this goal. Figure 5.1 schematically demonstrates how cascading SFG and DFG processes can be employed to accomplish this wavelength translation. First, the signal is moved to a much higher frequency via SFG with pump (λ_P). Then the output of the SFG process undergoes a DFG process with another control pump (λ_C) to generate the output, which is shifted with respect to the input signal.

As mentioned in Section 1.4, TFLN is a great platform for realization of efficient second-order nonlinear processes. In the following subsections SFG, DFG, and cascading processes are briefly explained to provide the required background for this project. Periodic poling is used as the phase-matching method, which was covered in detail in Sections 1.4.1 and 1.4.2.

5.1.1 Sum-Frequency Generation (SFG)

The SFG process has the ability to mix two distinct wavelengths and generate a signal at the frequency equal to the summation of them, which makes it suitable for numerous

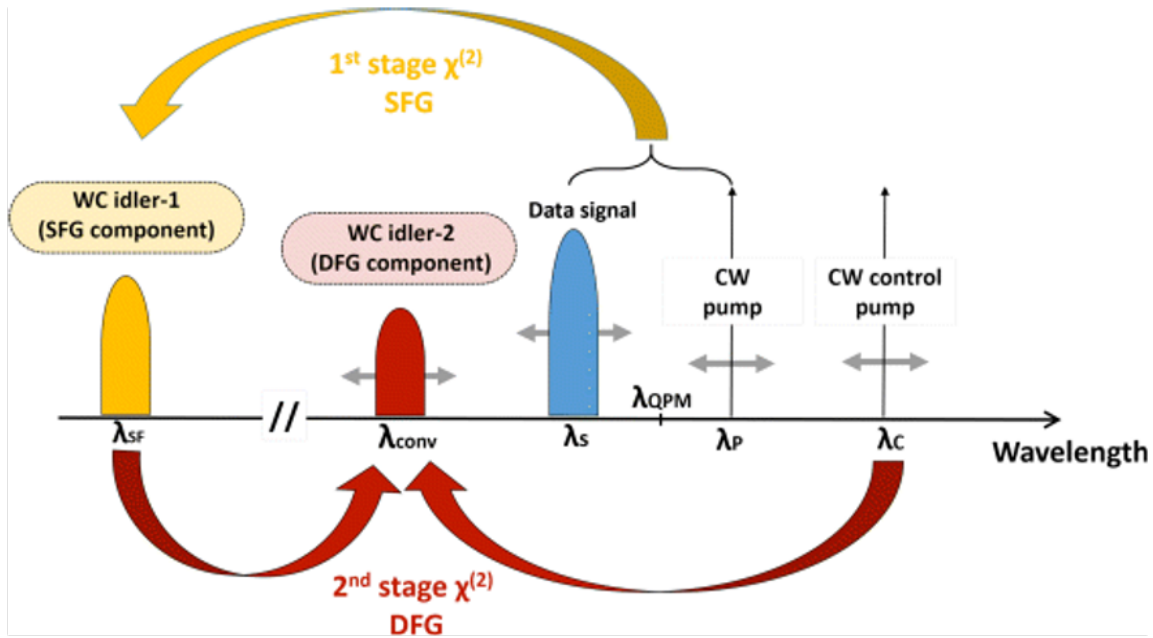


Figure 5.1: Schematic of a wavelength translator using cascaded SFG/DFG processes

applications. SFG can be used to generate light at frequency ranges where SHG cannot be utilized due to the lack of efficient lasers. It is also very common to use SFG for upconversion detection. For instance, low-power mid-infrared (mid-IR) light, down to a single-photon [135], can be converted to visible wavelengths and detected using low-noise and high-performance visible detectors. SFG on TFLN has been demonstrated on both straight waveguides [136, 65] and resonant-based structures [137, 138, 139]. Our team demonstrated a SFG bandwidth of ~ 20 nm in a TFLN PPLN device with normalized conversion efficiency of ~ 900 $\%W^{-1}cm^{-2}$, when one of the lasers was at a fixed wavelength and the other one was swept within its tuning range [65]. Additionally, swiping both lasers resulted in SFG from 1,460 nm to 1,620 nm. In microdisk resonators, a Conversion efficiency of $2.2 \times 10^{-3} W^{-1}$ is reported with a relatively low Q of 1.8×10^5 using the MPM method [138]. Ideally, conversion efficiencies four times larger than SHG should be achieved for SFG [140]. Therefore, having state-of-the-art values for Q and utilizing nat-

ural QPM or PPLN - as the most efficient PM methods for resonators so far - can notably boost the efficiency of SFG. SFG can be combined with other second-order nonlinear phenomena, such as SHG, to obtain highly-efficient higher-order nonlinear processes through cascading [141, 142, 143, 144, 145, 50]. Moreover, SFG has been cascaded with the EO effect, which is in principle a second-order nonlinear process as well. This is very useful for low-power and high-speed control of SFG [146].

5.1.2 *Difference-Frequency Generation (DFG)*

As the name suggests, DFG process generates a signal at the frequency equal to the frequency difference between the two input signals. DFG has been extensively used for generating terahertz and mid-IR sources on other platforms [147, 148]. On the TFLN platform, DFG has been demonstrated using both straight waveguides [44, 149] and resonant-based structures [48]. A new hybrid TFLN/Si platform is proposed by providing numerical simulation results to utilize DFG for terahertz generation [150], though it appears to be challenging to be realized from the fabrication perspective. Using periodically-poled TFLN on sapphire - with transparency window up to $4.5 \mu\text{m}$ - mid-infrared generation up to $3.66 \mu\text{m}$ with a DFG normalized conversion efficiency of $200 \text{ \%W}^{-1}\text{cm}^{-2}$ is demonstrated [149]. Sapphire helps with circumventing the high absorption loss of the oxide layer at wavelengths longer than $2.5 \mu\text{m}$ [151, 149]. Cascaded SHG/DFG is used to demonstrate effective four-wave mixing on a microdisk on TFLN using MPM [152]. In collaboration with Johns Hopkins university, our group have utilized DFG in a TFLN PPLN device and spectral filtering to demonstrate a novel optical isolator concept based on nonlinear optics [44]. The isolator has a wide bandwidth ($> 150 \text{ nm}$) with 40 dB transmittance difference between forward and backward propagating waves.

5.1.3 Cascaded Second-Order Nonlinear Processes

Higher order harmonics and wave mixing effects can occur by cascading $\chi^{(2)}$ processes in a single or multiple TFLN devices. Furthermore, effective third-order nonlinearities can be realized through cascading $\chi^{(2)}$ processes[153]. This is specifically very intriguing for the TFLN platform since $\chi^{(2)}$ of LN is much stronger than its other nonlinearities. Cascading $\chi^{(2)}$ processes has been extensively studied on the TFLN platform in order to further improve the performance of other nonlinear processes[154, 143, 152, 144, 145, 155, 156, 157, 67].

There are several methods to achieve such cascading effects (see Fig. 5.2). A straightforward method is by placing two or more different periodically-poled sections, each being responsible for a specific $\chi^{(2)}$ process. For instance, our group demonstrated two device (each with two cascaded PPLN sections) for low-harmonic generation, namely third- and fourth- harmonic generations (THG and FHG). For THG, the first PPLN segment was designed for SHG while the second PPLN was responsible for SFG, resulting in a cascaded SHG/SFG ($\omega + \omega \rightarrow 2\omega / 2\omega + \omega \rightarrow 3\omega$). For FHG, both PPLN segments were poled for SHG, resulting in SHG/SHG ($\omega + \omega \rightarrow 2\omega / 2\omega + 2\omega \rightarrow 4\omega$)[154]. Another method is to have more than one period in a PPLN device and generate a wider range of k -vectors to compensate for different phase-mismatching required for various nonlinear processes. This has been done in a chirped PPLN straight waveguide, which resulted in illustration of high-harmonics up to the 13th harmonic[145]. Also, a PPLN microdisk with dual period was utilized for THG and FHG[76]. Additionally, it is possible to achieve cascading in a single PPLN waveguide for THG and FHG via pulse pumping and by slightly detuning the pump wavelength from the QPM wavelength[65, 67, 157]. This latter method was used to demonstrate self-phase modulation with an effective nonlinear refractive index,

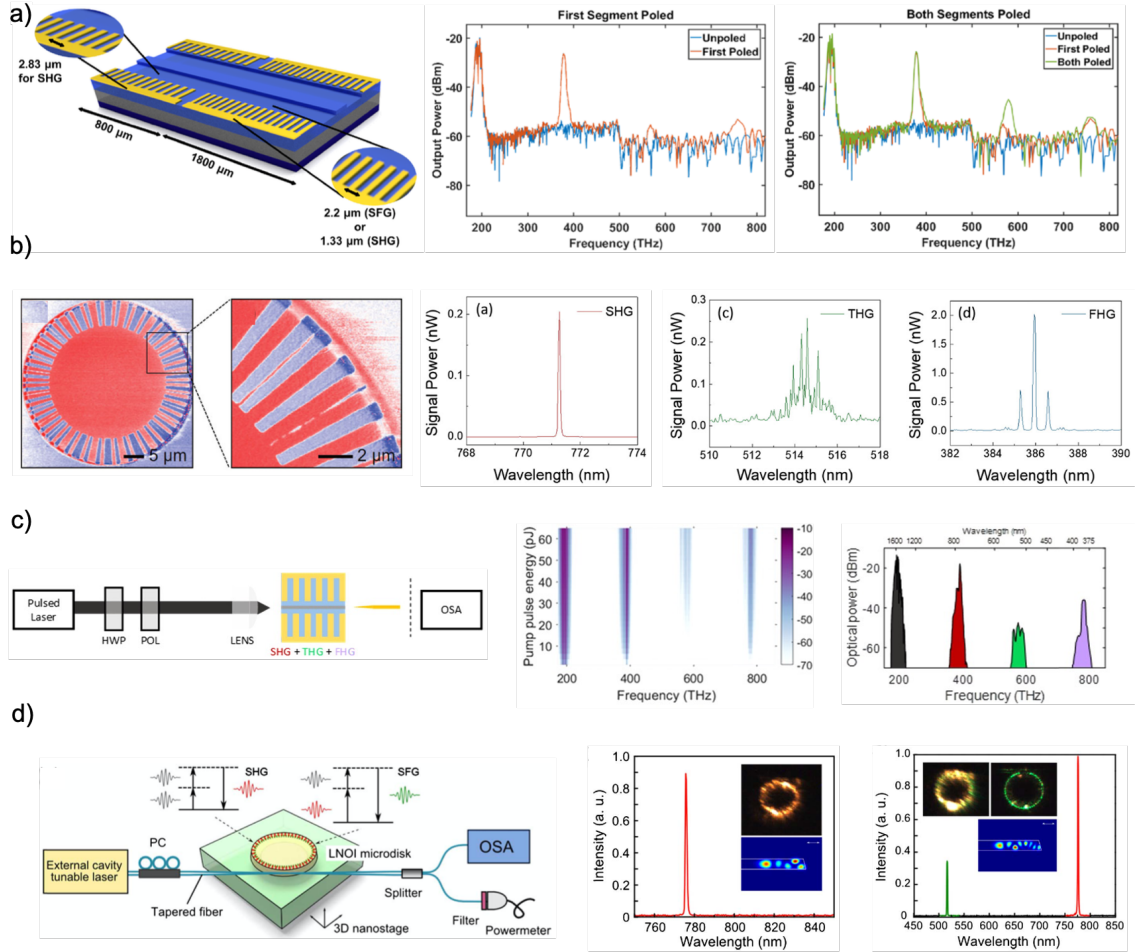
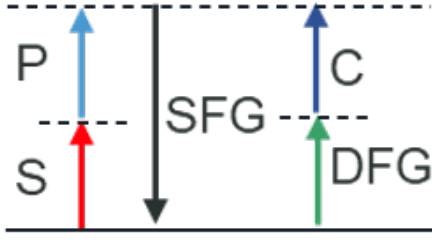


Figure 5.2: Some of the schemes used for implementing cascaded $\chi^{(2)}$ processes in TFLN and the corresponding harmonic generations. a) Two PPLN sections with different poling periods to enable SHG/SFG cascading for a THG device and SHG/SHG for a FHG device [154]. b) Dual-period PPLN microdisk with demonstrated THG and FHG [76]. c) THG and FHG on a single PPLN device via pulse pumping [65]. d) SHG and THG on a microdisk through cascaded SHG/SFG by taking advantage of the natural BPM [143].

$n_{2,eff}$, that is almost 200 times larger than the intrinsic n_2 of LN in a dispersion-engineered PPLN waveguide[157]. The effective $\chi_{eff}^{(3)}$ reported in this paper is larger than other well-known photonic Kerr-based platforms (such as Si and SiN) and proves the effectiveness of the cascading process. Moreover, in the first reported cascaded $\chi^{(2)}$ for THG in a res-



$$\omega_{df} = \omega_s + \omega_p - \omega_c$$

Figure 5.3: Energy-level description of the cascaded SFG/DFG process for wavelength translation

onator, it was shown that natural BPM can be employed to observe both SHG and THG at higher values of pump power[143].

5.2 Theory

The energy-level description of the cascaded SFG/DFG process for wavelength translation is illustrated in Fig. 5.3. The updated theory for this simultaneous SFG/DFG process in a single waveguide using coupled amplitude equations and under slowly varying approximation can be expressed as Equ. 5.1:

$$\frac{\partial A_p}{\partial z} = K_p A_{sf} A_s^* e^{i\Delta k_{sf} z} - \frac{\alpha_p}{2} A_p \quad (5.1a)$$

$$\frac{\partial A_s}{\partial z} = K_s A_{sf} A_p^* e^{i\Delta k_{sf} z} - \frac{\alpha_s}{2} A_s \quad (5.1b)$$

$$\frac{\partial A_{sf}}{\partial z} = K_{sf1} A_p A_s e^{-i\Delta k_{sf} z} + K_{sf2} A_c A_{df} e^{-i\Delta k_{df} z} - \frac{\alpha_{sf}}{2} A_{sf} \quad (5.1c)$$

$$\frac{\partial A_c}{\partial z} = K_c A_{sf} A_{df}^* e^{i\Delta k_{df} z} - \frac{\alpha_c}{2} A_c \quad (5.1d)$$

$$\frac{\partial A_{df}}{\partial z} = K_{df} A_{sf} A_c^* e^{i\Delta k_{df} z} - \frac{\alpha_{df}}{2} A_{df} \quad (5.1e)$$

Where A_i and α_i are the amplitude and propagation loss of the interacting waves, respectively. K_i denote the coupling coefficients that are defined as:

$$K_p = \frac{2i\omega_p^2}{k_p c^2} d_{eff} V_{sfg} \quad (5.2a)$$

$$K_s = \frac{2i\omega_s^2}{k_s c^2} d_{eff} V_{sfg} \quad (5.2b)$$

$$K_{sf1} = \frac{2i\omega_{sf}^2}{k_{sf} c^2} d_{eff} V_{sfg} \quad (5.2c)$$

$$K_{sf2} = \frac{2i\omega_{sf}^2}{k_{sf} c^2} d_{eff} V_{dfg} \quad (5.2d)$$

$$K_c = \frac{2i\omega_c^2}{k_c c^2} d_{eff} V_{dfg} \quad (5.2e)$$

$$K_{df} = \frac{2i\omega_{df}^2}{k_{df} c^2} d_{eff} V_{dfg} \quad (5.2f)$$

In which k_i and ω_i are the wave-vectors and angular frequencies of the interacting waves, respectively. c is the speed of light in vacuum, d_{eff} is the effective second-order nonlinear coefficient, and V_{sfg} and V_{dfg} are the normalized overlap integral of the interacting waves in the SFG and DFG processes, respectively. Δk_{sf} and Δk_{df} in Equ. 5.1 are the phase-mismatch terms for SFG and DFG processes, respectively, and are defined as:

$$\Delta k_{sf} = k_{sf} - k_p - k_s - k_m \quad (5.3a)$$

$$\Delta k_{df} = k_{sf} - k_c - k_{df} - k_m \quad (5.3b)$$

Where k_m is the phase term induced by the quasi-phase-matching technique, which is periodic poling in here and is calculated as:

$$k_m = \frac{2\pi}{\Lambda} \quad (5.4)$$

Where Λ is the poling period.

Using results from [158], the analytical conversion efficiency for this simultaneous cascaded SFG/DFG process is given by:

$$\begin{aligned}\eta_{cSF/DF} &= \frac{P_{df}}{P_s P_p P_c L^4} \\ &= \left[\left(\frac{n_{2\omega}}{n_\omega} \right) \eta_{SHG} \right]^2 \cdot \frac{4}{L^4} \left\{ \left[\frac{L}{\Delta} \sin(\Delta L) + \frac{\cos(\Delta L) - 1}{\Delta^2} \right]^2 + \left[\frac{\sin(\Delta L)}{\Delta^2} - \frac{L}{\Delta} \cos(\Delta L) \right]^2 \right\}\end{aligned}\quad (5.5)$$

Where P_i is the optical power of the interacting waves, L is the length of the device, η_{SHG} is the normalized efficiency for second-harmonic generation, and $n_{2\omega}$ and n_ω are the refractive indices at second-harmonic and fundamental wavelengths. Parameter Δ is the average phase mismatch and is given by:

$$\Delta = \frac{\Delta k_{sf} + \Delta k_{df}}{2} \quad (5.6)$$

It should be noted that Δ can always be managed to be zero with proper choice of pump wavelength.

Equation 5.5 is written in terms of normalized conversion efficiency for SHG in order to simplify the modal analysis since it only requires two modes. Also, in this equation, it is assumed that $\delta = \Delta k_{sf} - \Delta k_{df} = 0$, which is valid when the input and output signal wavelengths are the same. However, in practice, when the input and output wavelengths are not equal, δ will be non-zero and the peak efficiency will be reduced. While this analytical solution provides a very good approximation of the conversion efficiency, full numerical solution of the coupled amplitude equations is required for the general case.

5.3 Design

To meet the requirements for this project the ultimate device must have two PPLN waveguides for TE and TM polarizations with similar performances in terms of power, efficiency, and bandwidth. The following sections discuss these figure of merits and how to obtain the design parameters to fulfill the requirements of the project.

5.3.1 Efficiency

Obviously, one of the main goals of the design is to maximize the power and efficiency of the cascaded SFG/DFG process according to Equ. 5.5. Therefore, η_{SHG} needs to be maximized, which is defined as:

$$\eta_{SHG} = \frac{P_{2\omega}}{P_{\omega}^2 L^2} = \frac{2\omega^2 d_{eff}^2}{n_{\omega}^2 n_{2\omega} \epsilon_0 c^3 A_{eff}} \quad (5.7)$$

Where d_{eff} is the effective nonlinear coefficient and is equal to $d_{eff} = 2d_{33}/\pi$ for a first order quasi phase-matched interaction with all the waves polarized along the z-axis. A_{eff} is the mode effective area and is given by:

$$A_{eff} = \frac{[\iint_{-\infty}^{\infty} |E_{\omega}(x,y)|^2 dx dy]^2 [\iint_{-\infty}^{\infty} |E_{2\omega}(x,y)|^2 dx dy]}{[\iint_{LN} E_{\omega}^2(x,y) E_{2\omega}(x,y) dx dy]^2} \quad (5.8)$$

The effective area has units of μm^2 and describes the optical mode size and spatial overlap between the pump and second-harmonic waves. In Equ. 5.8, $E(x,y)$ are the normalized simulated electric field mode profiles. Therefore, to maximize the efficiency of the process, A_{eff} needs to be minimized, which is dictated by the waveguide dimensions.

There are five more consideration in designing the waveguides to obtain the highest effi-

ciency out of the devices: 1) The waveguides should be single mode at the pump wavelength, 2) TM slab coupling should be avoided, 3) TE polarization fraction should be ideally 100%, 4) The width of the waveguide shouldn't be too small, and 5) The etch depth should be minimized. The last two considerations make sure the overlap of the optical mode and the side-walls of the waveguide are minimized, since LN's etch process is physical and the side-walls are rough, which causes optical propagation loss.

Taking all the mentioned criteria into account, resulted in designing 900 nm-wide waveguides on a LNOI platform with 500 nm-thick LN layer and etch depth of 250 nm to form the ridge waveguide. With these parameters, the poling period is calculated to be $3.24\mu\text{m}$ using the following equation:

$$\Lambda = \frac{\lambda_{\omega}}{2(n_{2\omega} - n_{\omega})} \quad (5.9)$$

As mentioned earlier, this project requires two identical PPLN waveguides for the two polarizations. To meet this requirement, we decided to put two waveguides within the gap of one set of poling electrodes and fingers to achieve similar poling condition for the two waveguides. The distance between the two waveguides is designed to be $8\mu\text{m}$ to avoid the coupling between them and each waveguide is $3\mu\text{m}$ away from the edge of the gold fingers to avoid optical propagation loss. The schematic of the device along with the design parameters are illustrated in Fig. 5.4.

5.3.2 Bandwidth

Another important requirement for this project is to have ~ 100 GHz of bandwidth for the process. Bandwidth is inversely proportional to the length of the device, hence shorter devices can easily meet this requirement. However, larger bandwidth does not offer any

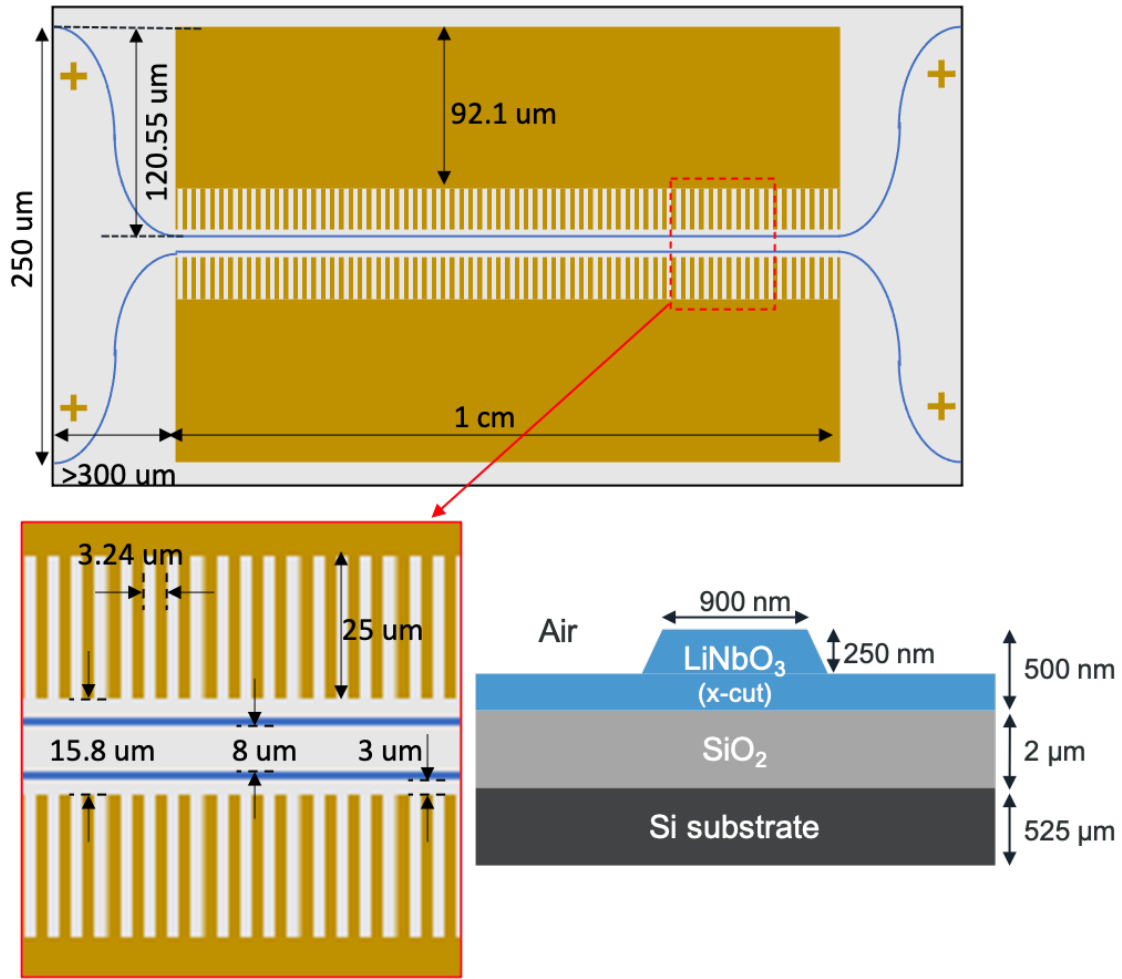


Figure 5.4: Schematic drawing of the design with parameters

benefit and in fact shorter devices provide less output power, which is not favorable. On the other hand, longer devices are more sensitive to fabrication and poling errors. Therefore, the optimum length of the device should be calculated to satisfy all these conditions.

For SHG, bandwidth can be calculated using the transfer function:

$$P_{SH} \propto \text{sinc}^2\left(\frac{\Delta k \cdot L}{2}\right) \quad (5.10)$$

Where the phase mismatch is defined as:

$$\Delta k = k_{2\omega} - 2k_{\omega} - k_{QPM} \quad (5.11)$$

According to Equ. 5.10, the SHG power drops by 50% when $\Delta k.L = \pm 2.78$. Therefore, phase matching bandwidth can be evaluated by considering the amount of angular frequency detuning, Ω , that can be imparted on the fundamental wave before the generated second-harmonic power drops to 50%. The angular frequency detuning can be incorporated to Equ. 5.11 in the following way:

$$\Delta k(\Omega) = k(2\omega + 2\Omega) - 2k(\omega + \Omega) - k_{QPM} \quad (5.12)$$

Which using Taylor series expansion of Δk with respect to Ω , can be written as:

$$\Delta k(\Omega) = \Delta k_0 + 2\Delta k' \Omega + \Delta k'' \Omega^2 \quad (5.13)$$

Where Δk_0 , $\Delta k'$ (group velocity mismatch), and $\Delta k''$ (group velocity dispersion) are defined as:

$$\Delta k_0 = k_{2\omega} - 2k_{\omega} - k_{QPM} \quad (5.14a)$$

$$\Delta k' = \frac{1}{v_{g,2\omega}} - \frac{1}{v_{g,\omega}} \quad (5.14b)$$

$$\Delta k'' = 2GVD(2\omega) - GVD(\omega) \quad (5.14c)$$

In which v_g is the group velocity and GVD is the group velocity dispersion. As explained in the last section, poling period is designed such that $\Delta k_0 = 0$. Therefore, the bandwidth is typically dominated by the group velocity mismatch or $\Delta k'$. If we neglect the higher order term (Ω^2), we find $\Delta k.L = \pm 2.78$ when $2\Delta k'.\Omega.L = \pm 2.78$. Therefore, the half-width-

half-maximum angular frequency bandwidth is:

$$\Omega_{HWHF,SHG} = \frac{2.78}{2\Delta k'.L} \text{ [rad/s]} \quad (5.15)$$

And full-width-half-maximum frequency is equal to:

$$f_{FWHF,SHG} = \frac{2.78}{2\pi\Delta k'.L} \text{ [Hz]} \quad (5.16)$$

When group velocity mismatch is small, the high order dispersion terms dominate and the bandwidth calculation above is not accurate. To improve the accuracy, we can include the next higher order term. We now find $\Delta k.L = \pm 2.78$ when $(2\Delta k'.\Omega + \Delta k''.\Omega^2)L = \pm 2.78$. Rewriting in normal quadratic form which is easily solved using quadratic formula:

$$\Delta k''.\Omega^2 + 2\Delta k'.\Omega \mp \frac{2.78}{L} = 0 \quad (5.17)$$

It is noted that in some cases when the bandwidth is very large, this approximation may still fail and therefore even more high order terms are needed.

For the full cascaded process the output power is given by:

$$P_{output} \propto 4\left\{\left[\frac{L}{\Delta}\sin(\Delta L) + \frac{\cos(\Delta L) - 1}{\Delta^2}\right]^2 + \left[\frac{\sin(\Delta L)}{\Delta^2} - \frac{L}{\Delta}\cos(\Delta L)\right]^2\right\} \quad (5.18)$$

Which is equal to 0.5 when $\Delta.L = \pm 3.4766569$. We have made the approximation that the input and output wavelengths are the same, i.e., $\omega_p \approx \omega_s \approx \omega_c \approx \omega_{df} = \omega$. Therefore, $\Delta k_{sf} = \Delta k_{df}$ and hence $\Delta = (\Delta k_{sf} + \Delta k_{df})/2 = \Delta k_{sf}$ and $\delta = \Delta k_{sf} - \Delta k_{df} = 0$. With this assumption, we have:

$$\Delta = \Delta_{sf} = k_{sf} - k_p - k_s - k_{QPM} = k_{2\omega} - 2k_{\omega} - k_{QPM} \quad (5.19)$$

Consequently, everything is similar to the case of SHG and by just changing the fixed number from 2.78 to 3.4766569 all the aforementioned equations can be used here as well. Based on the mode simulation results and to meet the requirements, a 1 cm-long device is chosen for this project.

These parameters are included in the mask layout shown in Fig. 5.5. The 40 sets of devices include 5 variations for the poling periods to account for LN thickness variation and/or deviation from the targeted etch depth, 2 variations of the device length, and repeating each device 4 times on different parts of the chip. It was mentioned earlier that these devices are designed to be 1 cm long. However, since the longer devices are more sensitive to fabrication errors, 5 mm-long devices are also included in the layout.

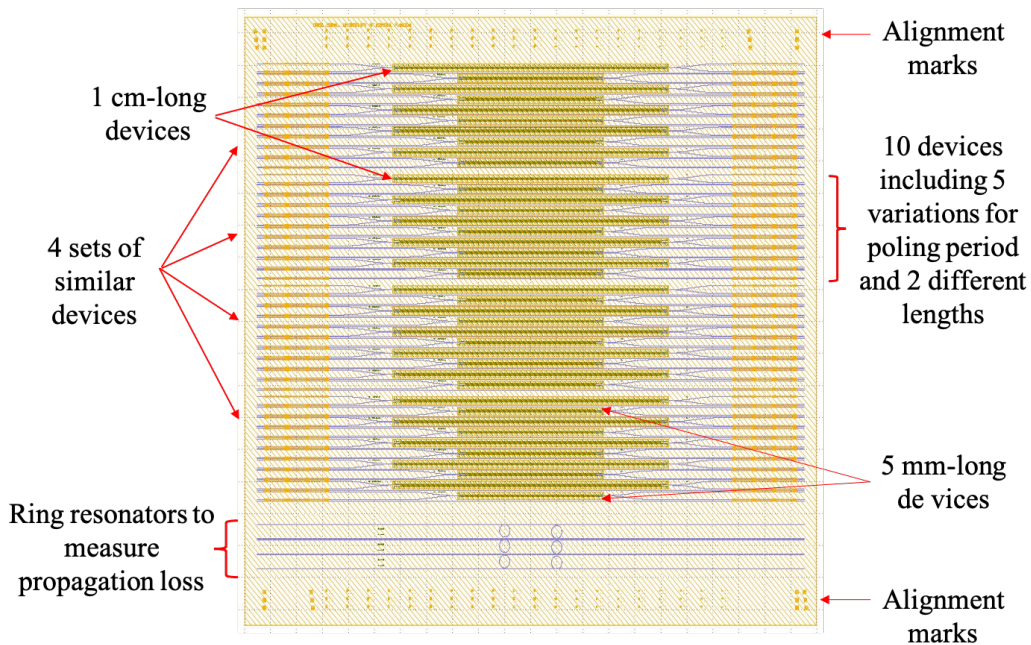


Figure 5.5: Mask layout used for fabrication of the devices for nonlinear wavelength translator project.

5.4 Experimental Results and Discussion

The fabrication of this chip started with first E-beam lithography run on ZEP-520A E-beam resist followed by a metal deposition and lift-off process to define the alignment marks. Next, another E-beam lithography was done to pattern the resist around the waveguides and etch the LN layer for 250 nm to form the rib optical waveguides. Finally, another metal deposition and lift-off was performed after the final E-beam run for the formation of the electrodes and fingers. Figure 5.6 demonstrates some of the microscopic images of the fabricated chip.

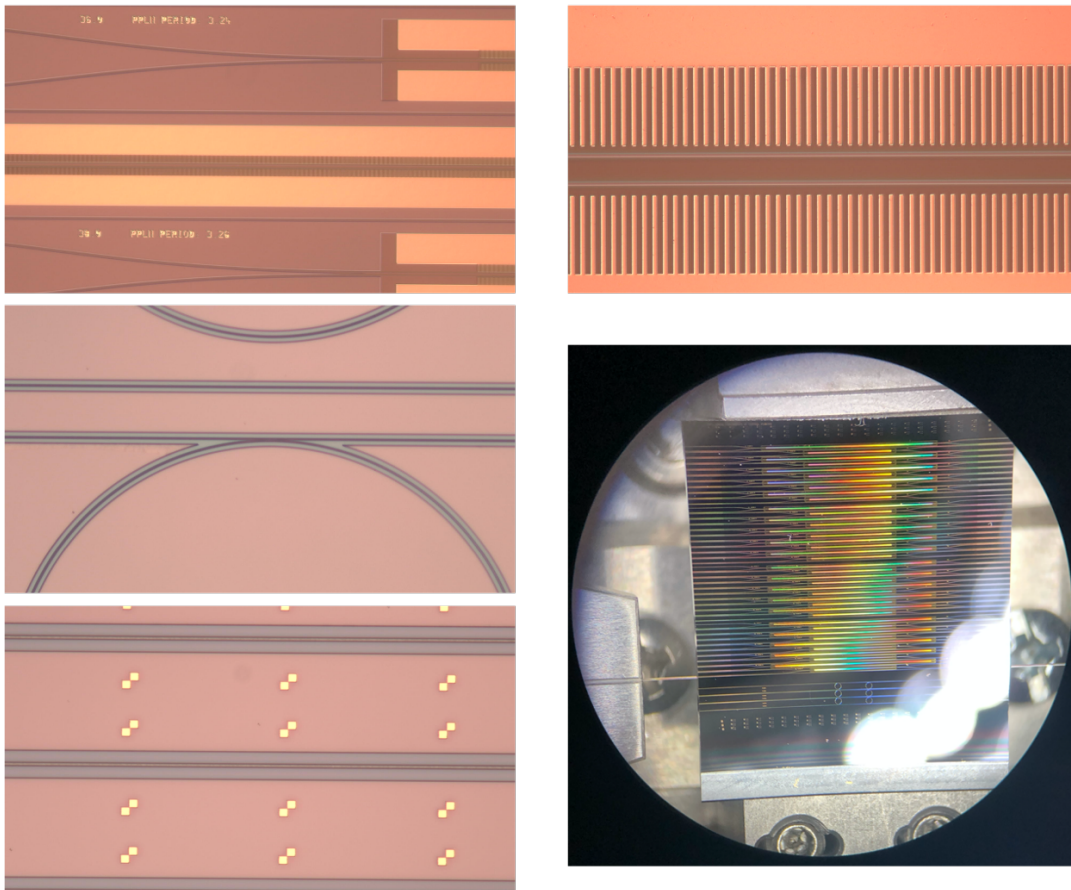


Figure 5.6: Some of the microscopic images and the fabricated chip.

Figure 5.7 exhibits the setup that is used for poling and measurement of these devices. For poling, the probes are placed on the electrodes and a high voltage is applied to them such that considering the gap between the electrodes the applied electric field exceeds the coercive field of TFLN. For the parameters mentioned in last sections, the required voltage for this project is more than 750 V. Such high voltages can cause breakdown of air and also damage or burn the electrodes (see Fig. 5.8). For this reason, a few drops of Silicone oil was placed on the chip before applying the high voltage. This oil covers the surrounding area of the waveguide and changes the effective indices of the waveguide modes, which precludes us from actively monitoring the second-harmonic generation process. Therefore, finding the best required waveform to achieve efficient poling becomes challenging.

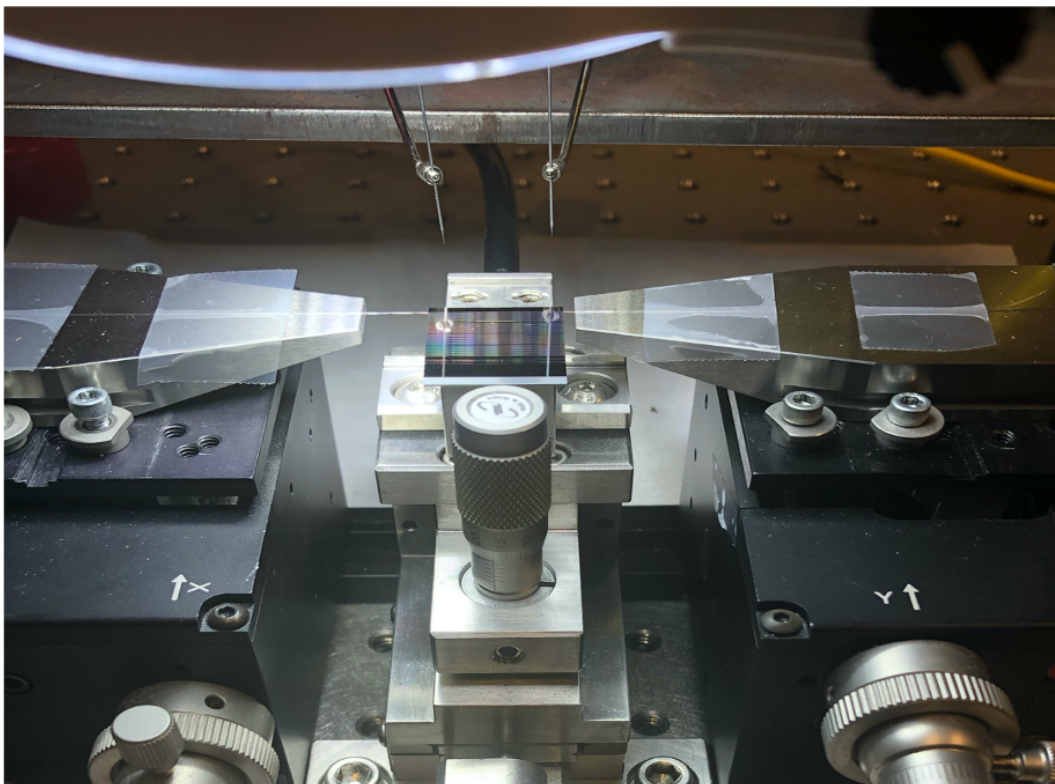


Figure 5.7: Poling and measurement setup.

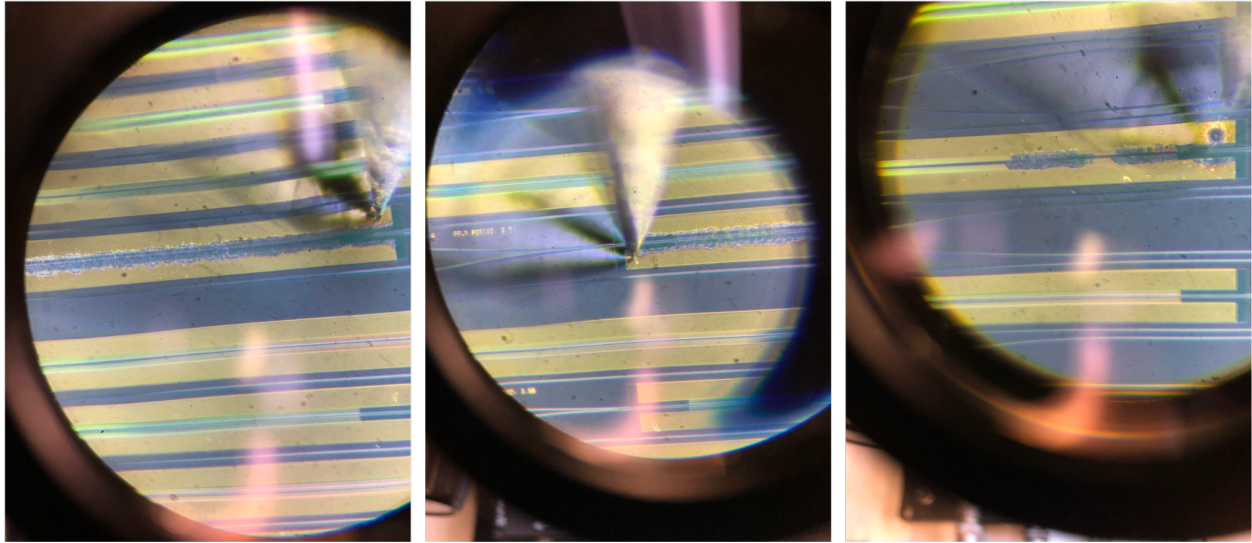


Figure 5.8: Applying voltages more than 500 V resulted in burning the electrodes.

In order to overcome this challenge, the poling fingers for some of the devices were designed to have their central second-harmonic generation wavelength within the range of our tunable laser when oil is applied on the chip. To achieve this, it was assumed that the oil uniformly covers around the waveguides and possesses refractive index of 1.5. This could help us to find the best required waveform for poling. Poling, depoling, and poling again in one of these devices with pulse duration of 5 ms and period of 5 s and peak voltage value of 800 V resulted in second-harmonic generation shown in Fig. 5.9. For other devices designed to work with oil, the central wavelength of SHG was out of the range of our tunable laser.

for other devices, as mentioned earlier, the SHG couldn't be observed during the poling process since the oil changes the central wavelength of SHG significantly. Therefore, the poling was done first. Then, oil was completely removed from the sample through standard cleaning with Acetone, 2-Propanol, and DI-water followed by RCA-1 cleaning procedure. Next, devices were measured in order to observe SHG. Unfortunately, none of

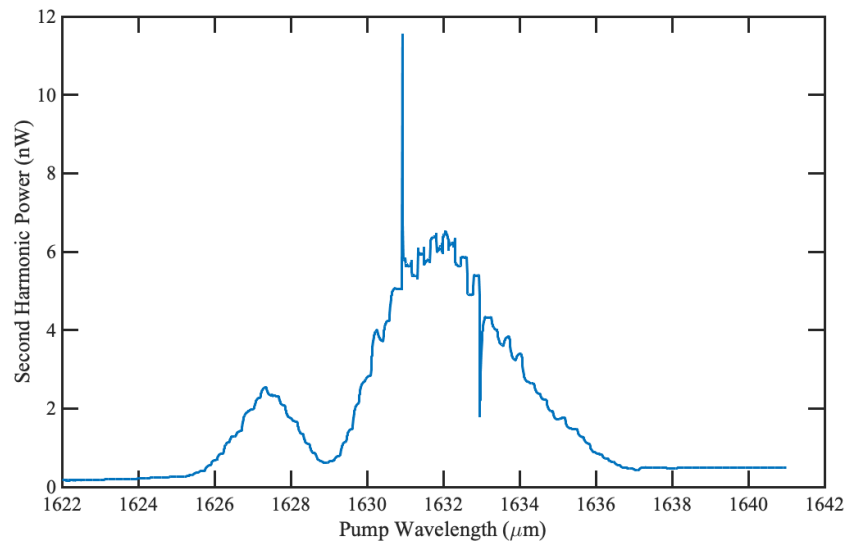


Figure 5.9: Second-harmonic generation in one of the devices that was designed to work with oil.

the devices had their central wavelength within the range of our tunable laser. This discrepancy between the design and experiment is originating from the difference between the assumed waveguide shape in the design and the actual shape that was achieved after fabrication. The difference in the side wall angle had the most significant impact, but also the waveguides were etched for 240 nm instead of 250 nm that was considered in the design.

CHAPTER 6: CONCLUSION AND FUTURE WORK

Thin-film lithium niobate is a great candidate for realization of compact photonic integrated circuits owing to its wide transparency window and phenomenal electro-optic, nonlinear optic, and ferroelectric properties along with its high index contrast. As it was mentioned before, Many different photonic components and circuits can be efficiently implemented on this platform. In this dissertation, we used this versatile platform to demonstrate a wide range of devices and applications. First, Bragg grating filters with two transmission peaks within the stop band were demonstrated, which can be harnessed in quantum optic applications. Then, high-speed electro-optic Mach-Zehnder modulators with extrapolated 3-dB bandwidth of 170 GHz and half-wave voltage-length product of 3.3 V.cm was reported with many different applications, especially in data communication. Next, microwave to photonic converter devices were shown, which can be used as a microwave electro-optic sensor and proves the effectiveness of TFLN platform in microwave photonic applications. Finally, periodically-poled lithium niobate devices were used for demonstration of nonlinear wavelength translators on TFLN.

TFLN is still at its early stages of development and will have a lot more to offer in the near future. This chapter provides some of the future directions that can be pursued following the presented works in this dissertation.

6.1 Integrated Frequency-Domain Hong-Ou-Mandel Interferometer

Hong-Ou-Mandel (HOM) interference is a fundamental quantum mechanical phenomenon [159], which can be used in several quantum information processing applications. Spatial-

domain HOM interferometer was shown on conventional LN platform [160, 161] using PPLN as the source of photon-pair generation, followed by electro-optic modulators to control the phase and beam splitter for the interference of the photons. Frequency-domain HOM interferometer was demonstrated on optical tables [95] using a PPLN crystal for photon-pair generation followed by a pulse shaper to filter two narrowband part of the wide output spectrum of the generated photons and then using a phase modulator the entangled photons interfered in the frequency domain.

The tunable dual channel filter that was reported in Chapter 2 can be replaced with the pulse shaper and serve the same purpose. Therefore, the frequency-domain HOM can be integrated in one chip consisting of a PPLN device, dual channel filter, and a phase modulator. We designed and fabricated a chip to demonstrated a fully integrated frequency-domain HOM interferometer on TFLN platform. Figure 6.1 exhibits the mask layout and the fabricated chip.

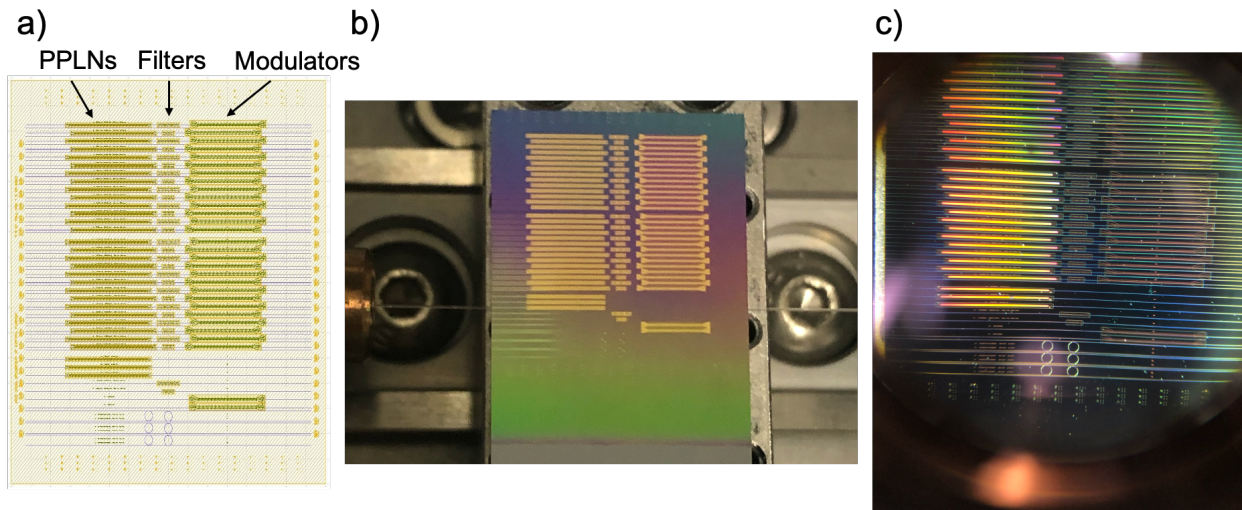


Figure 6.1: a) Mask layout, b) Picture of the measurement setup, and c) Microscopic image of the fabricated chip for integrated frequency-domain HOM interferometer.

It is very challenging to get the desired response from this circuit. As it was mentioned in Chapter 5 the central wavelength of PPLN devices are very sensitive to the fabrication errors. Also, dual channel filters are low yield in terms of having the two transmission peaks with the intended frequency separation working around the central wavelength that are designed and with a reasonable extinction ratio and peak power penalty. Therefore, combining these two components and have them working around the same center wavelength and fulfill other requirements becomes a very challenging task. In the fabricated chip, only three filters demonstrated two transmission peaks within the stop band, which among them only one of them had the frequency separation close to what we were aiming for (see Fig. 6.2(a)). However, the center wavelength of the photon-pair generated by the PPLN device was around 1545 nm (see Fig. 6.2(b)) while the central wavelength of the filter response was around 1522.5 nm. As it was shown in Chapter 2, the low tunability factor demonstrated for these filter cannot be used for tuning the filter response over 20 nm and it is mostly for fine tuning.

Nevertheless, the design for this chip is ready and can be tweaked with a more delicate design to account for any possible variation during the fabrication process to make sure at least one of the devices will meet the requirements.

6.2 Microwave to Optical Converter on TFLN on Quartz Substrate

As it was mentioned in Chapter 4, the best performance for microwave to optical converter devices can be obtained on TFLN platform on quartz substrate. The design of these devices for this platform is already completed and the design parameters are shown in Fig. 4.2 and Fig. 4.3. The fabrication of these devices on Quartz substrate has been done twice. Figure 6.3 demonstrates the mask layout used for the fabrication along with some

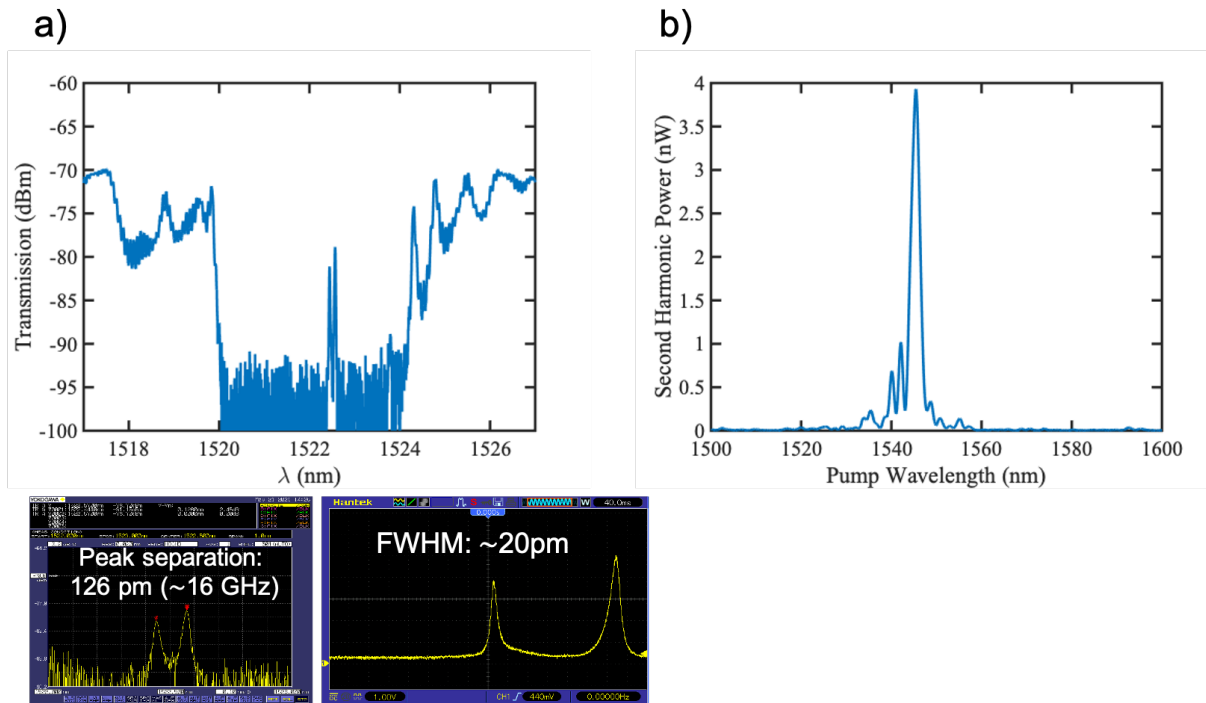


Figure 6.2: Measurement results for the integrated HOM interferometer. a) Filter's spectral response along with the peak separation and FWHM. b) Second-harmonic generation using the PPLN device.

of the microscopic images of the fabricated chips. However, none of these fabricated devices were functional, which is due to the differences in the process of these chips compared to the process of devices on TFLN on silicon substrate. E-beam lithography, etching, dicing, and polishing need to be modified and optimized for these chips.

Figures 6.4(a) and (b) exhibit SEM images of the fabricated chips, in which several cracks on the LN layer as well as a large gap between LN layer and the insulator layer underneath can be observed. These could be attributed to the wafer quality or the over-heating during one of the processes such as etching, dicing, and polishing. It could also be due to the mechanical stress that is applied to the bonded thin-film layer during dicing or polishing. The imperfections in the E-beam run can be clearly seen in Fig. 6.4(c), where shows

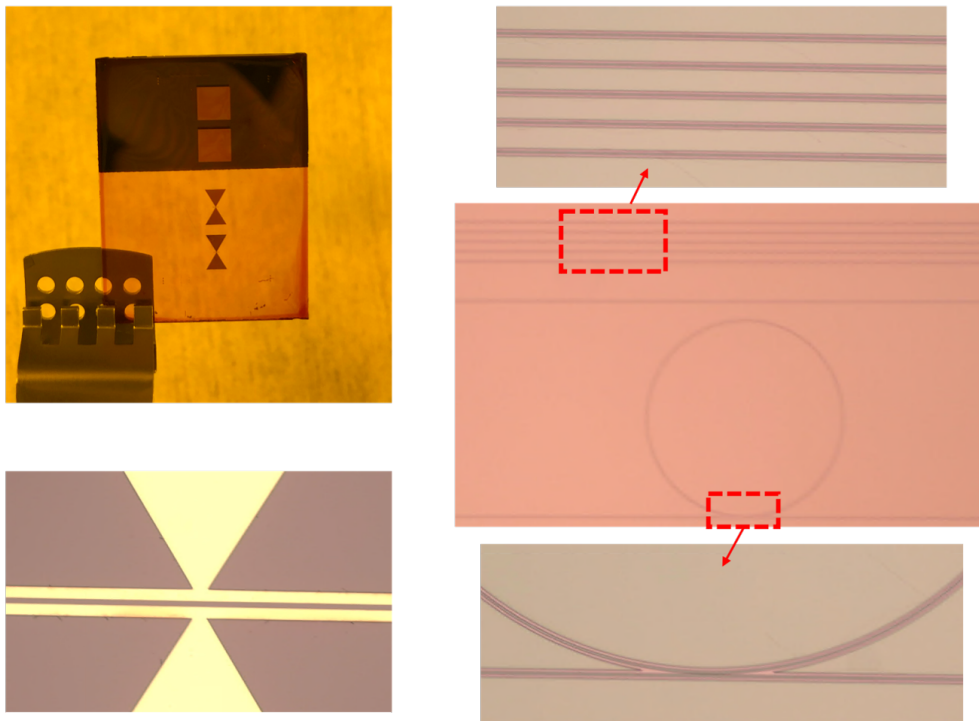
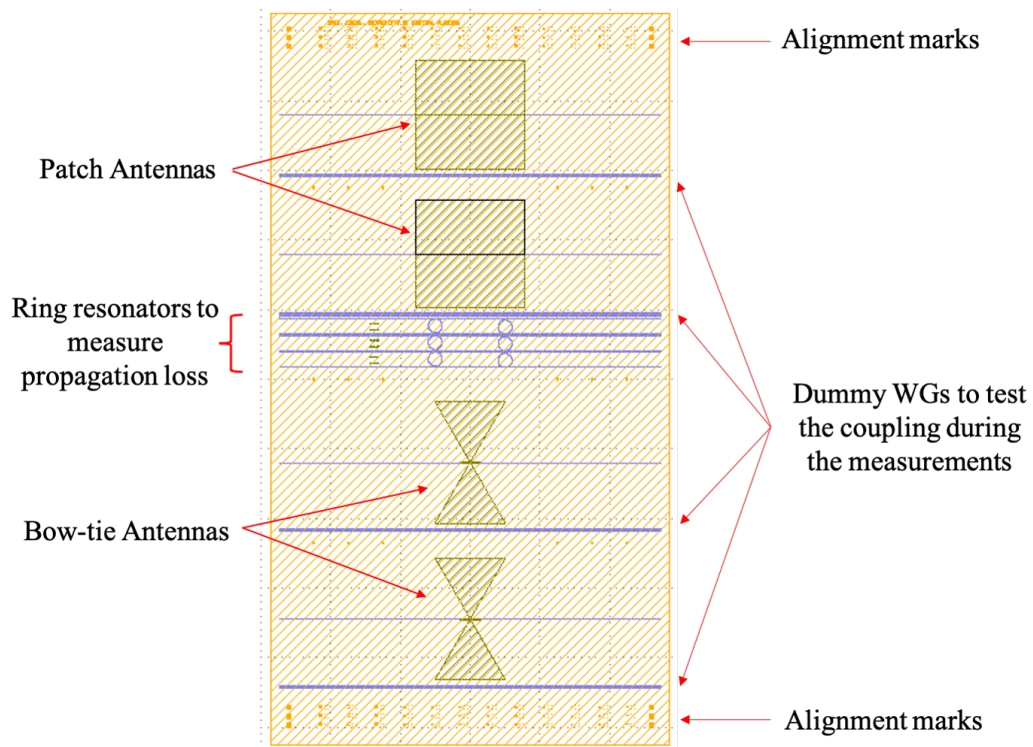


Figure 6.3: Layout and some of the microscopic images of the fabricated devices on quartz substrate.

a microscopic image of the waveguides after E-beam run and development before etching. Etching the LN layer with this pattern after E-beam run results in very non-uniform waveguides as illustrated in Fig. 6.4(d).

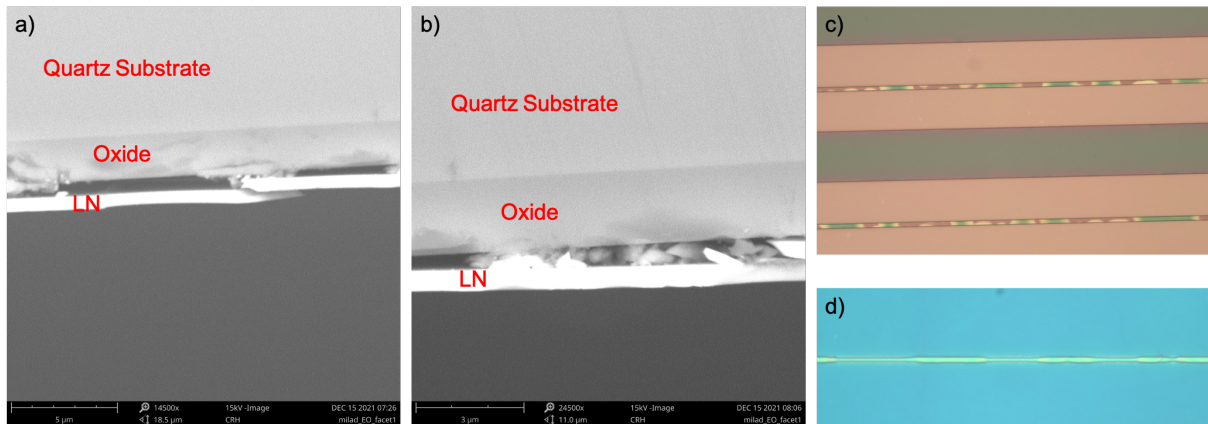


Figure 6.4: SEM images of the fabricated chip on Quartz substrate in a) and b) show the issues occurred during the fabrication. Microscopic images of the waveguides c) after E-beam lithography and development and d) after the etch step.

Several modifications are required for E-beam lithography on TFLN on quartz substrate since the thermal conductivity of these chips are very different from the ones on silicon substrate. Also, there is no conductive material in these chips and thus a conductive layer such as a thin layer of gold needs to be deposited on the resist to avoid charge accumulation, which also affects the E-beam run parameters. Moreover, the etch step should be modified as well since the thermal conductivity of quartz is much less than silicon and causes overheating, which changes the etch rate and can also damage the bonding between LN and oxide layers. All these processes are currently being optimized for the quartz substrate and the full fabrication will be done afterwards.

6.3 Experimental Demonstration of Nonlinear Wavelength Translator

In Chapter 5 it was explained that because of the discrepancy between the design and fabrication, the central wavelength of the PPLN devices were shifted out of the range of our tunable laser. This information is now being used in the design to avoid this issue in the second round of fabrication. Moreover, the propagation loss for the last fabricated chip was measured to be ~ 4 dB/cm (see Fig. 6.5), which is high.

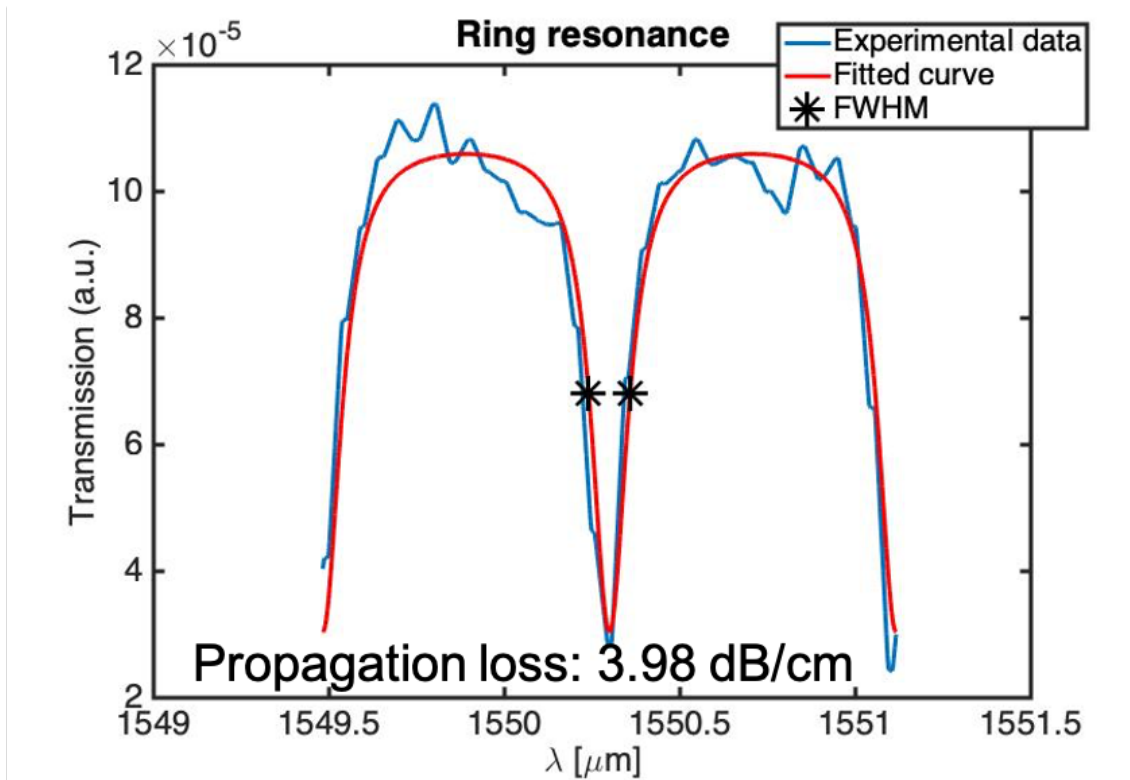


Figure 6.5: Propagation loss measurement of the first fabricated chip for the nonlinear wavelength translator project.

From the SEM images of the fabricated waveguides shown in Fig. 6.6, it is evident that the side walls are rough and since the waveguides are very compact (900 nm-wide with 250 nm etch depth), the optical mode touches the side walls and results in high propagation

loss. Therefore, we are also developing a better etch recipe for LN to reduce the optical propagation loss.

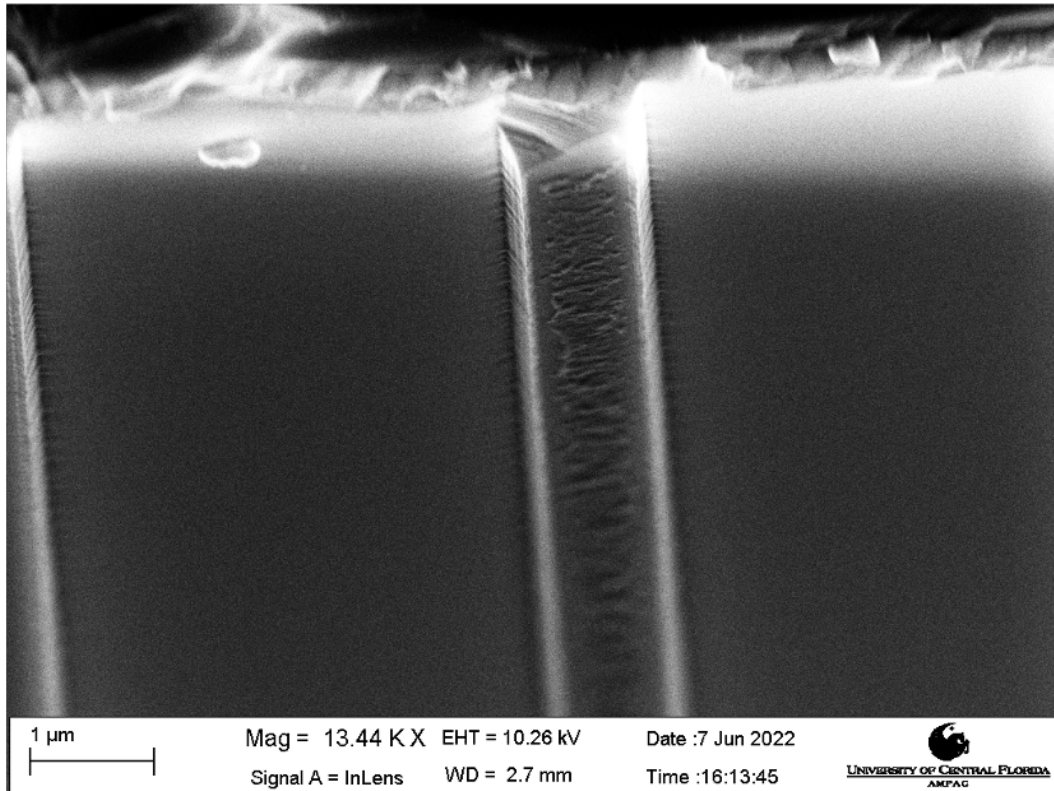


Figure 6.6: SEM image of the fabricated waveguide in the first round of fabrication demonstrating rough side walls, which causes high optical propagation loss.

Also, it can be seen in this SEM image that the residue of the resist is left on top of the waveguide even after several standard cleaning (Acetone, 2-Propanol, and DI water) as well as RCA-1 and O_2 plasma cleaning and putting the sample in hot NMP. This is because LN is etched through ion milling process and for deep etch (such as 250 nm in here) it can burn the E-beam resist. The burned E-beam resist is very hard to remove from the sample.

We are taking all the necessary steps to prevent all the aforementioned issues to happen again in the next round of fabrication.

APPENDIX: COPYRIGHT PERMISSIONS

Applications of thin-film lithium niobate in nonlinear integrated photonics, [Advanced Photonics, 2022](#)

Dear Milad,

Thank you for seeking permission from SPIE to reprint material from our publications. SPIE shares the copyright with you, so as author you retain the right to reproduce your paper in part or in whole.

Publisher's permission is hereby granted under the following conditions: (1) the material to be used has appeared in our publication without credit or acknowledgment to another source; and (2) you credit the original SPIE publication. Include the authors' names, title of paper, volume title, SPIE volume number, and year of publication in your credit statement.

Please let me know if I may be of any further assistance.

Best,

Karleena Burdick

Editorial Assistant, Publications

SPIE – the international society for optics and photonics

karleenab@spie.org

1 360 685 5515

Tunable dual-channel ultra-narrowband Bragg grating filter on thin-film lithium niobate, [Optics Letters](#), 2021

Dear Milad,

Thank you for contacting Optica Publishing Group.

For the use of material from Kamal Abdelsalam, Ehsan Ordouie, Milad G. Vazimali, Farzaneh A. Juneghani, Prem Kumar, Gregory S. Kanter, and Sasan Fathpour, "Tunable dual-channel ultra-narrowband Bragg grating filter on thin-film lithium niobate," *Opt. Lett.* 46, 2730-2733 (2021):

Because you are the author of the source paper from which you wish to reproduce material, Optica Publishing Group considers your requested use of its copyrighted materials to be permissible within the author rights granted in the Copyright Transfer Agreement submitted by the requester on acceptance for publication of his/her manuscript. If the entire article is being included, it is requested that the Author Accepted Manuscript (or preprint) version be the version included within the thesis and that a complete citation of the original material be included in any publication. This permission assumes that the material was not reproduced from another source when published in the original publication.

The Author Accepted Manuscript version is the preprint version of the article that was accepted for publication but not yet prepared and/or formatted by Optica Publishing Group or its vendors.

While your publisher should be able to provide additional guidance, we prefer the below citation formats:

For citations in figure captions:

[Reprinted/Adapted] with permission from [ref #] © Optica Publishing Group. (Please include the full citation in your reference list)

For images without captions:

Journal Vol. #, first page (year published) An example: Opt. Express 19, 2720 (2011)

Please let me know if you have any questions.

Kind Regards,

Hannah Greenwood

Hannah Greenwood

June 13, 2022

Authorized Agent, Optica Publishing Group

Integrated Electro-Optical Sensors for Microwave Photonic Applications on Thin-Film
Lithium Niobate, [IEEE, 2021 International Topical Meeting on Microwave Photonics](#)
(MWP)

Thesis / Dissertation Reuse

The IEEE does not require individuals working on a thesis to obtain a formal reuse license, however, you may print out this statement to be used as a permission grant:

Requirements to be followed when using any portion (e.g., figure, graph, table, or textual material) of an IEEE copyrighted paper in a thesis:

1) In the case of textual material (e.g., using short quotes or referring to the work within these papers) users must give full credit to the original source (author, paper, publication) followed by the IEEE copyright line © 2011 IEEE. 2) In the case of illustrations or tabular material, we require that the copyright line © [Year of original publication] IEEE appear prominently with each reprinted figure and/or table. 3) If a substantial portion of the original paper is to be used, and if you are not the senior author, also obtain the senior author's approval.

Requirements to be followed when using an entire IEEE copyrighted paper in a thesis:

1) The following IEEE copyright/ credit notice should be placed prominently in the references: © [year of original publication] IEEE. Reprinted, with permission, from [author names, paper title, IEEE publication title, and month/year of publication] 2) Only the accepted version of an IEEE copyrighted paper can be used when posting the paper or your thesis on-line. 3) In placing the thesis on the author's university website, please display the following message in a prominent place on the website: In reference to IEEE copy-

righted material which is used with permission in this thesis, the IEEE does not endorse any of [university/educational entity's name goes here]'s products or services. Internal or personal use of this material is permitted. If interested in reprinting/republishing IEEE copyrighted material for advertising or promotional purposes or for creating new collective works for resale or redistribution, please go to http://www.ieee.org/publications_standards/publications/rights/rights_link.html to learn how to obtain a License from RightsLink.

If applicable, University Microfilms and/or ProQuest Library, or the Archives of Canada may supply single copies of the dissertation.

LIST OF REFERENCES

- [1] R. Weis and T. Gaylord, "Lithium niobate: summary of physical properties and crystal structure," *Applied Physics A*, vol. 37, no. 4, pp. 191–203, 1985.
- [2] D. N. Nikogosyan, *Nonlinear optical crystals: a complete survey*. Springer Science & Business Media, 2006.
- [3] N. Li, C. P. Ho, S. Zhu, Y. H. Fu, Y. Zhu, and L. Y. T. Lee, "Aluminium nitride integrated photonics: A review," *Nanophotonics*, 2021.
- [4] H. Zhang, X. He, Y. Shih, M. Schurman, Z. Feng, and R. Stall, "Study of nonlinear optical effects in gan: Mg epitaxial film," *Applied physics letters*, vol. 69, no. 20, pp. 2953–2955, 1996.
- [5] R. Schmidt and I. Kaminow, "Metal-diffused optical waveguides in LiNbO_3 ," *Applied Physics Letters*, vol. 25, no. 8, pp. 458–460, 1974.
- [6] J. L. Jackel, C. Rice, and J. Veselka, "Proton exchange for high-index waveguides in LiNbO_3 ," *Applied Physics Letters*, vol. 41, no. 7, pp. 607–608, 1982.
- [7] S. Fathpour, "Heterogeneous nonlinear integrated photonics," *IEEE Journal of Quantum Electronics*, vol. 54, no. 6, pp. 1–16, 2018.
- [8] P. Rabiei, J. Ma, S. Khan, J. Chiles, and S. Fathpour, "Heterogeneous lithium niobate photonics on silicon substrates," *Optics express*, vol. 21, no. 21, pp. 25573–25581, 2013.
- [9] "Partow technologies, llc.." <http://www.partow-tech.com/>. Accessed: Mar 2022.
- [10] "Nanoln.." <http://www.nanoln.com/>. Accessed: Mar 2022.

- [11] “Ngk insulators, ltd..” <https://www.ngk-insulators.com/>. Accessed: Mar 2022.
- [12] Y. Kong, F. Bo, W. Wang, D. Zheng, H. Liu, G. Zhang, R. Rupp, and J. Xu, “Recent progress in lithium niobate: optical damage, defect simulation, and on-chip devices,” *Advanced Materials*, vol. 32, no. 3, p. 1806452, 2020.
- [13] Y. Xu, M. Shen, J. Lu, J. B. Surya, A. Al Sayem, and H. X. Tang, “Mitigating photorefractive effect in thin-film lithium niobate microring resonators,” *Optics Express*, vol. 29, no. 4, pp. 5497–5504, 2021.
- [14] A. L. Kozub, A. Schindlmayr, U. Gerstmann, and W. G. Schmidt, “Polaronic enhancement of second-harmonic generation in lithium niobate,” *Physical Review B*, vol. 104, no. 17, p. 174110, 2021.
- [15] M. Boukhtouta, Y. Megdoud, S. Benlamari, H. Meradji, Z. Chouahda, R. Ahmed, S. Ghemid, M. Abu-Jafar, S. Syrotyuk, D. Rai, *et al.*, “Predictions on structural, electronic, optical and thermal properties of lithium niobate via first-principle computations,” *Philosophical Magazine*, vol. 100, no. 9, pp. 1150–1171, 2020.
- [16] A. Rao, A. Patil, J. Chiles, M. Malinowski, S. Novak, K. Richardson, P. Rabiei, and S. Fathpour, “Heterogeneous microring and mach-zehnder modulators based on lithium niobate and chalcogenide glasses on silicon,” *Optics express*, vol. 23, no. 17, pp. 22746–22752, 2015.
- [17] A. Rao, M. Malinowski, A. Honardoost, J. R. Talukder, P. Rabiei, P. Delfyett, and S. Fathpour, “Second-harmonic generation in periodically-poled thin film lithium niobate wafer-bonded on silicon,” *Optics express*, vol. 24, no. 26, pp. 29941–29947, 2016.

- [18] A. Honardoost, F. A. Juneghani, R. Safian, and S. Fathpour, "Towards subterahertz bandwidth ultracompact lithium niobate electrooptic modulators," *Optics express*, vol. 27, no. 5, pp. 6495–6501, 2019.
- [19] M. Zhang, C. Wang, R. Cheng, A. Shams-Ansari, and M. Lončar, "Monolithic ultra-high-Q lithium niobate microring resonator," *Optica*, vol. 4, no. 12, pp. 1536–1537, 2017.
- [20] R. Gao, H. Zhang, F. Bo, W. Fang, Z. Hao, N. Yao, J. Lin, J. Guan, L. Deng, M. Wang, *et al.*, "Broadband highly efficient nonlinear optical processes in on-chip integrated lithium niobate microdisk resonators of Q-factor above 10^8 ," *New Journal of Physics*, vol. 23, no. 12, p. 123027, 2021.
- [21] K. Luke, P. Kharel, C. Reimer, L. He, M. Loncar, and M. Zhang, "Wafer-scale low-loss lithium niobate photonic integrated circuits," *Optics Express*, vol. 28, no. 17, pp. 24452–24458, 2020.
- [22] J. Lin, F. Bo, Y. Cheng, and J. Xu, "Advances in on-chip photonic devices based on lithium niobate on insulator," *Photonics Research*, vol. 8, no. 12, pp. 1910–1936, 2020.
- [23] Y. Jia, L. Wang, and F. Chen, "Ion-cut lithium niobate on insulator technology: Recent advances and perspectives," *Applied Physics Reviews*, vol. 8, no. 1, p. 011307, 2021.
- [24] D. Sun, Y. Zhang, D. Wang, W. Song, X. Liu, J. Pang, D. Geng, Y. Sang, and H. Liu, "Microstructure and domain engineering of lithium niobate crystal films for integrated photonic applications," *Light: Science & Applications*, vol. 9, no. 1, pp. 1–18, 2020.

- [25] Y. Jiao, Z. Shao, S. Li, X. Wang, F. Bo, J. Xu, and G. Zhang, "Improvement on thermal stability of nano-domains in lithium niobate thin films," *Crystals*, vol. 10, no. 2, p. 74, 2020.
- [26] M. Younesi, R. Geiss, S. Rajaei, F. Setzpfandt, Y.-H. Chen, and T. Pertsch, "Periodic poling with a micrometer-range period in thin-film lithium niobate on insulator," *JOSA B*, vol. 38, no. 3, pp. 685–691, 2021.
- [27] B. J. Stanicki, M. Younesi, F. J. F. Löchner, H. Thakur, W.-K. Chang, R. Geiss, F. Setzpfandt, Y.-H. Chen, and T. Pertsch, "Surface domain engineering in lithium niobate," *OSA Continuum*, vol. 3, no. 2, pp. 345–358, 2020.
- [28] Y. Liu, X. Yan, J. Wu, B. Zhu, Y. Chen, and X. Chen, "On-chip erbium-doped lithium niobate microcavity laser," *Science China Physics, Mechanics & Astronomy*, vol. 64, no. 3, pp. 1–5, 2021.
- [29] R. Gao, J. Guan, N. Yao, L. Deng, J. Lin, M. Wang, L. Qiao, Z. Wang, Y. Liang, Y. Zhou, *et al.*, "On-chip ultra-narrow-linewidth single-mode microlaser on lithium niobate on insulator," *Optics Letters*, vol. 46, no. 13, pp. 3131–3134, 2021.
- [30] Q. Luo, C. Yang, R. Zhang, Z. Hao, D. Zheng, H. Liu, X. Yu, F. Gao, F. Bo, Y. Kong, *et al.*, "On-chip erbium-doped lithium niobate microring lasers," *Optics Letters*, vol. 46, no. 13, pp. 3275–3278, 2021.
- [31] X. Liu, X. Yan, H. Li, Y. Chen, X. Chen, *et al.*, "Tunable single-mode laser on thin film lithium niobate," *Optics Letters*, vol. 46, no. 21, pp. 5505–5508, 2021.
- [32] D. Yin, Y. Zhou, Z. Liu, Z. Wang, H. Zhang, Z. Fang, W. Chu, R. Wu, J. Zhang, W. Chen, *et al.*, "Electro-optically tunable microring laser monolithically integrated on lithium niobate on insulator," *Optics Letters*, vol. 46, no. 9, pp. 2127–2130, 2021.

- [33] R. Zhang, C. Yang, Z. Hao, D. Jia, Q. Luo, D. Zheng, H. Liu, X. Yu, F. Gao, F. Bo, *et al.*, “Integrated lithium niobate single-mode lasers by the vernier effect,” *Science China Physics, Mechanics & Astronomy*, vol. 64, no. 9, pp. 1–5, 2021.
- [34] M. Yu, Y. Okawachi, R. Cheng, C. Wang, M. Zhang, A. L. Gaeta, and M. Lončar, “Raman lasing and soliton mode-locking in lithium niobate microresonators,” *Light: Science & Applications*, vol. 9, no. 1, pp. 1–7, 2020.
- [35] D. Zhu, L. Shao, M. Yu, R. Cheng, B. Desiatov, C. Xin, Y. Hu, J. Holzgrafe, S. Ghosh, A. Shams-Ansari, *et al.*, “Integrated photonics on thin-film lithium niobate,” *Advances in Optics and Photonics*, vol. 13, no. 2, pp. 242–352, 2021.
- [36] C. O. de Beeck, F. M. Mayor, S. Cuyvers, S. Poelman, J. F. Herrmann, O. Atalar, T. P. McKenna, B. Haq, W. Jiang, J. D. Witmer, *et al.*, “III/V-on-lithium niobate amplifiers and lasers,” *Optica*, vol. 8, no. 10, pp. 1288–1289, 2021.
- [37] A. Shams-Ansari, D. Renaud, R. Cheng, L. Shao, L. He, D. Zhu, M. Yu, H. R. Grant, L. Johansson, M. Zhang, *et al.*, “Electrically pumped laser transmitter integrated on thin-film lithium niobate,” *Optica*, vol. 9, no. 4, pp. 408–411, 2022.
- [38] A. Honardoost, K. Abdelsalam, and S. Fathpour, “Rejuvenating a versatile photonic material: thin-film lithium niobate,” *Laser & Photonics Reviews*, vol. 14, no. 9, p. 2000088, 2020.
- [39] Y. Qi and Y. Li, “Integrated lithium niobate photonics,” *Nanophotonics*, vol. 9, no. 6, pp. 1287–1320, 2020.
- [40] M. Xu, Y. Zhu, F. Pittalà, J. Tang, M. He, W. C. Ng, J. Wang, Z. Ruan, X. Tang, M. Kuschnerov, *et al.*, “Dual-polarization thin-film lithium niobate in-phase quadra-

- ture modulators for terabit-per-second transmission," *Optica*, vol. 9, no. 1, pp. 61–62, 2022.
- [41] F. Arab Juneghani, J. Zhao, M. Gholipour Vazimali, X. Chen, S. Thai Le, H. Chen, E. Ordouie, N. K. Fontaine, and S. Fathpour, "Demonstration of non-symmetric thin-film lithium niobate modulator with a 3-db bandwidth beyond 100 ghz, *Accepted*," in *CLEO: Science and Innovations*, p. NA, Optical Society of America, 2022.
- [42] C. Hu, A. Pan, T. Li, X. Wang, Y. Liu, S. Tao, C. Zeng, and J. Xia, "High-efficient coupler for thin-film lithium niobate waveguide devices," *Optics Express*, vol. 29, no. 4, pp. 5397–5406, 2021.
- [43] K. Abdelsalam, E. Ordouie, M. G. Vazimali, F. A. Juneghani, P. Kumar, G. S. Kanter, and S. Fathpour, "Tunable dual-channel ultra-narrowband bragg grating filter on thin-film lithium niobate," *Optics Letters*, vol. 46, no. 11, pp. 2730–2733, 2021.
- [44] K. Abdelsalam, T. Li, J. B. Khurgin, and S. Fathpour, "Linear isolators using wavelength conversion," *Optica*, vol. 7, no. 3, pp. 209–213, 2020.
- [45] X. Ye, F. Ni, H. Li, H. Liu, Y. Zheng, and X. Chen, "High-speed programmable lithium niobate thin film spatial light modulator," *Optics Letters*, vol. 46, no. 5, pp. 1037–1040, 2021.
- [46] R. W. Boyd, *Nonlinear optics*. Academic press, 2020.
- [47] C. Lu, Y. Zhang, J. Qiu, Y. Tang, T. Ding, S. Liu, Y. Zheng, and X. Chen, "Highly tunable birefringent phase-matched second-harmonic generation in an angle-cut lithium niobate-on-insulator ridge waveguide," *Optics Letters*, vol. 47, no. 5, pp. 1081–1084, 2022.

- [48] R. Luo, Y. He, H. Liang, M. Li, J. Ling, and Q. Lin, "Optical parametric generation in a lithium niobate microring with modal phase matching," *Physical Review Applied*, vol. 11, no. 3, p. 034026, 2019.
- [49] A. Rao, J. Chiles, S. Khan, S. Toroghi, M. Malinowski, G. F. Camacho-González, and S. Fathpour, "Second-harmonic generation in single-mode integrated waveguides based on mode-shape modulation," *Applied Physics Letters*, vol. 110, no. 11, p. 111109, 2017.
- [50] J. Lin, N. Yao, Z. Hao, J. Zhang, W. Mao, M. Wang, W. Chu, R. Wu, Z. Fang, L. Qiao, *et al.*, "Broadband quasi-phase-matched harmonic generation in an on-chip monocrystalline lithium niobate microdisk resonator," *Physical review letters*, vol. 122, no. 17, p. 173903, 2019.
- [51] C. Wang, Z. Li, M.-H. Kim, X. Xiong, X.-F. Ren, G.-C. Guo, N. Yu, and M. Lončar, "Metasurface-assisted phase-matching-free second harmonic generation in lithium niobate waveguides," *Nature Communications*, vol. 8, no. 1, pp. 1–7, 2017.
- [52] E. Lim, M. M. Fejer, R. Byer, and W. Kozlovsky, "Blue light generation by frequency doubling in periodically poled lithium niobate channel waveguide," *Electronics letters*, vol. 25, no. 11, pp. 731–732, 1989.
- [53] L. E. Myers, R. Eckardt, M. Fejer, R. Byer, W. Bosenberg, and J. Pierce, "Quasi-phase-matched optical parametric oscillators in bulk periodically poled LiNbO_3 ," *JOSA B*, vol. 12, no. 11, pp. 2102–2116, 1995.
- [54] L. Chang, Y. Li, N. Volet, L. Wang, J. Peters, and J. E. Bowers, "Thin film wavelength converters for photonic integrated circuits," *Optica*, vol. 3, no. 5, pp. 531–535, 2016.

- [55] J. T. Nagy and R. M. Reano, "Reducing leakage current during periodic poling of ion-sliced x-cut MgO doped lithium niobate thin films," *Optical Materials Express*, vol. 9, no. 7, pp. 3146–3155, 2019.
- [56] A. Boes, L. Chang, T. Nguyen, G. Ren, J. Bowers, and A. Mitchell, "Efficient second harmonic generation in lithium niobate on insulator waveguides and its pitfalls," *Journal of Physics: Photonics*, vol. 3, no. 1, p. 012008, 2021.
- [57] J. Zhao, M. Rüsing, M. Roeper, L. M. Eng, and S. Mookherjea, "Poling thin-film x-cut lithium niobate for quasi-phase matching with sub-micrometer periodicity," *Journal of Applied Physics*, vol. 127, no. 19, p. 193104, 2020.
- [58] B. Slautin, A. Turygin, E. Greshnyakov, A. Akhmatkhanov, H. Zhu, and V. Y. Shur, "Domain structure formation by local switching in the ion sliced lithium niobate thin films," *Applied Physics Letters*, vol. 116, no. 15, p. 152904, 2020.
- [59] J. T. Nagy and R. M. Reano, "Submicrometer periodic poling of lithium niobate thin films with bipolar preconditioning pulses," *Optical Materials Express*, vol. 10, no. 8, pp. 1911–1920, 2020.
- [60] S. Reitzig, M. Rüsing, J. Zhao, B. Kirbus, S. Mookherjea, and L. M. Eng, ""seeing is believing"—in-depth analysis by co-imaging of periodically-poled x-cut lithium niobate thin films," *Crystals*, vol. 11, no. 3, p. 288, 2021.
- [61] R. K. Prasath, I. R. Rajan, G. Madhupriya, M. A. Meerasha, S. Boomadevi, and K. Pandiyan, "Measurement of the internal electric field in periodically poled congruent lithium niobate crystals by far-field diffraction," *Applied Optics*, vol. 60, no. 13, pp. 3791–3796, 2021.

- [62] A. Boes, L. Chang, M. Knoerzer, T. G. Nguyen, J. D. Peters, J. E. Bowers, and A. Mitchell, "Improved second harmonic performance in periodically poled LNOI waveguides through engineering of lateral leakage," *Optics Express*, vol. 27, no. 17, pp. 23919–23928, 2019.
- [63] C. Wang, C. Langrock, A. Marandi, M. Jankowski, M. Zhang, B. Desiatov, M. M. Fejer, and M. Lončar, "Ultrahigh-efficiency wavelength conversion in nanophotonic periodically poled lithium niobate waveguides," *Optica*, vol. 5, no. 11, pp. 1438–1441, 2018.
- [64] J.-y. Chen, Y. M. Sua, Z.-h. Ma, C. Tang, Z. Li, and Y.-p. Huang, "Efficient parametric frequency conversion in lithium niobate nanophotonic chips," *OSA Continuum*, vol. 2, no. 10, pp. 2914–2924, 2019.
- [65] A. Rao, K. Abdelsalam, T. Sjaardema, A. Honardoost, G. F. Camacho-Gonzalez, and S. Fathpour, "Actively-monitored periodic-poling in thin-film lithium niobate photonic waveguides with ultrahigh nonlinear conversion efficiency of 4600% $w^{-1}cm^{-2}$," *Optics express*, vol. 27, no. 18, pp. 25920–25930, 2019.
- [66] J. Zhao, M. Rüsing, U. A. Javid, J. Ling, M. Li, Q. Lin, and S. Mookherjea, "Shallow-etched thin-film lithium niobate waveguides for highly-efficient second-harmonic generation," *Optics Express*, vol. 28, no. 13, pp. 19669–19682, 2020.
- [67] C. Lu, H. Li, J. Qiu, Y. Zhang, S. Liu, Y. Zheng, and X. Chen, "Second and cascaded harmonic generation of pulsed laser in a lithium niobate on insulator ridge waveguide," *Optics Express*, vol. 30, no. 2, pp. 1381–1387, 2022.
- [68] J.-Y. Chen, C. Tang, Z.-H. Ma, Z. Li, Y. M. Sua, and Y.-P. Huang, "Efficient and highly tunable second-harmonic generation in z-cut periodically poled lithium niobate nanowaveguides," *Optics Letters*, vol. 45, no. 13, pp. 3789–3792, 2020.

- [69] J.-Y. Chen, Z.-H. Ma, Y. M. Sua, Z. Li, C. Tang, and Y.-P. Huang, "Ultra-efficient frequency conversion in quasi-phase-matched lithium niobate microrings," *Optica*, vol. 6, no. 9, pp. 1244–1245, 2019.
- [70] J. Lu, M. Li, C.-L. Zou, A. Al Sayem, and H. X. Tang, "Toward 1% single-photon anharmonicity with periodically poled lithium niobate microring resonators," *Optica*, vol. 7, no. 12, pp. 1654–1659, 2020.
- [71] Z. Hao, L. Zhang, W. Mao, A. Gao, X. Gao, F. Gao, F. Bo, G. Zhang, and J. Xu, "Second-harmonic generation using d_{33} in periodically poled lithium niobate microdisk resonators," *Photonics Research*, vol. 8, no. 3, pp. 311–317, 2020.
- [72] J. Lu, J. B. Surya, X. Liu, A. W. Bruch, Z. Gong, Y. Xu, and H. X. Tang, "Periodically poled thin-film lithium niobate microring resonators with a second-harmonic generation efficiency of 250,000%/W," *Optica*, vol. 6, no. 12, pp. 1455–1460, 2019.
- [73] M. Li, Y.-L. Zhang, H. X. Tang, C.-H. Dong, G.-C. Guo, and C.-L. Zou, "Photon-photon quantum phase gate in a photonic molecule with $\chi^{(2)}$ nonlinearity," *Physical Review Applied*, vol. 13, no. 4, p. 044013, 2020.
- [74] M. Heuck, K. Jacobs, and D. R. Englund, "Controlled-phase gate using dynamically coupled cavities and optical nonlinearities," *Physical review letters*, vol. 124, no. 16, p. 160501, 2020.
- [75] R. Wolf, Y. Jia, S. Bonaus, C. S. Werner, S. J. Herr, I. Breunig, K. Buse, and H. Zappe, "Quasi-phase-matched nonlinear optical frequency conversion in on-chip whispering galleries," *Optica*, vol. 5, no. 7, pp. 872–875, 2018.

- [76] L. Zhang, Z. Hao, Q. Luo, A. Gao, R. Zhang, C. Yang, F. Gao, F. Bo, G. Zhang, and J. Xu, "Dual-periodically poled lithium niobate microcavities supporting multiple coupled parametric processes," *Optics Letters*, vol. 45, no. 12, pp. 3353–3356, 2020.
- [77] S. Xie, J. Zhan, Y. Hu, Y. Zhang, S. Veilleux, J. Bland-Hawthorn, and M. Dagenais, "Add-drop filter with complex waveguide bragg grating and multimode interferometer operating on arbitrarily spaced channels," *Optics letters*, vol. 43, no. 24, pp. 6045–6048, 2018.
- [78] D. Liu, M. Zhang, Y. Shi, and D. Dai, "Four-channel cwdm (de) multiplexers using cascaded multimode waveguide gratings," *IEEE Photonics Technology Letters*, vol. 32, no. 4, pp. 192–195, 2020.
- [79] R. Cheng and L. Chrostowski, "Design of silicon integrated bragg gratings for microwave photonics signal processing," in *2019 International Topical Meeting on Microwave Photonics (MWP)*, pp. 1–4, IEEE, 2019.
- [80] S. Kaushal, R. Cheng, M. Ma, A. Mistry, M. Burla, L. Chrostowski, and J. Azaña, "Optical signal processing based on silicon photonics waveguide bragg gratings," *Frontiers of Optoelectronics*, vol. 11, no. 2, pp. 163–188, 2018.
- [81] W. Zhang and J. Yao, "A fully reconfigurable waveguide bragg grating for programmable photonic signal processing," *Nature communications*, vol. 9, no. 1, pp. 1–9, 2018.
- [82] S. Khan, M. A. Baghban, and S. Fathpour, "Electronically tunable silicon photonic delay lines," *Optics express*, vol. 19, no. 12, pp. 11780–11785, 2011.

- [83] P. Prabhathan, V. Murukeshan, Z. Jing, and P. V. Ramana, "Compact soi nanowire refractive index sensor using phase shifted bragg grating," *Optics express*, vol. 17, no. 17, pp. 15330–15341, 2009.
- [84] H. Wang, A. M. Lee, Z. Frehlick, H. Lui, D. I. McLean, S. Tang, and H. Zeng, "Perfectly registered multiphoton and reflectance confocal video rate imaging of in vivo human skin," *Journal of biophotonics*, vol. 6, no. 4, pp. 305–309, 2013.
- [85] N. C. Harris, D. Grassani, A. Simbula, M. Pant, M. Galli, T. Baehr-Jones, M. Hochberg, D. Englund, D. Bajoni, and C. Galland, "Integrated source of spectrally filtered correlated photons for large-scale quantum photonic systems," *Physical Review X*, vol. 4, no. 4, p. 041047, 2014.
- [86] D. Pohl, A. Messner, F. Kaufmann, M. R. Escalé, J. Holzer, J. Leuthold, and R. Grange, "100-gbd waveguide bragg grating modulator in thin-film lithium niobate," *IEEE Photonics Technology Letters*, vol. 33, no. 2, pp. 85–88, 2020.
- [87] W. Horn, S. Kroesen, J. Herrmann, J. Imbrock, and C. Denz, "Electro-optical tunable waveguide bragg gratings in lithium niobate induced by femtosecond laser writing," *Optics express*, vol. 20, no. 24, pp. 26922–26928, 2012.
- [88] K. Chen, F. Duan, and Y. Yu, "High-performance thermo-optic tunable grating filters based on laterally supported suspended silicon ridge waveguide," *Optics express*, vol. 26, no. 15, pp. 19479–19488, 2018.
- [89] D. Zhu, L. Shao, M. Yu, R. Cheng, B. Desiatov, C. Xin, Y. Hu, J. Holzgrafe, S. Ghosh, A. Shams-Ansari, *et al.*, "Integrated photonics on thin-film lithium niobate," *Advances in Optics and Photonics*, vol. 13, no. 2, pp. 242–352, 2021.

- [90] K. Abdelsalam, T. Li, J. B. Khurgin, and S. Fathpour, "Linear isolators using wavelength conversion," *Optica*, vol. 7, no. 3, pp. 209–213, 2020.
- [91] M. A. Baghban, J. Schollhammer, C. Errando-Herranz, K. B. Gylfason, and K. Gallo, "Bragg gratings in thin-film lithium niobate waveguides," *Optics Express*, vol. 25, no. 26, pp. 32323–32332, 2017.
- [92] M. R. Escalé, D. Pohl, A. Sergeev, and R. Grange, "Extreme electro-optic tuning of Bragg mirrors integrated in lithium niobate nanowaveguides," *Optics Letters*, vol. 43, no. 7, pp. 1515–1518, 2018.
- [93] A. Prencipe, M. A. Baghban, and K. Gallo, "Tunable ultranarrowband grating filters in thin-film lithium niobate," *ACS Photonics*, vol. 8, no. 10, pp. 2923–2930, 2021.
- [94] D. Pohl, F. Kaufmann, M. R. Escalé, J. Holzer, and R. Grange, "Tunable Bragg grating filters and resonators in lithium niobate-on-insulator waveguides," in *CLEO: Science and Innovations*, pp. STu4J–5, Optical Society of America, 2020.
- [95] P. Imany, O. D. Odele, M. S. Alshaykh, H.-H. Lu, D. E. Leaird, and A. M. Weiner, "Frequency-domain Hong-Ou-Mandel interference with linear optics," *Optics Letters*, vol. 43, no. 12, pp. 2760–2763, 2018.
- [96] B. S. Elkus, K. Abdelsalam, A. Rao, V. Velez, S. Fathpour, P. Kumar, and G. S. Kanter, "Generation of broadband correlated photon-pairs in short thin-film lithium-niobate waveguides," *Optics Express*, vol. 27, no. 26, pp. 38521–38531, 2019.
- [97] B. S. Elkus, K. Abdelsalam, S. Fathpour, P. Kumar, and G. S. Kanter, "Quantum-correlated photon-pair generation via cascaded nonlinearity in an ultra-compact lithium-niobate nano-waveguide," *Optics Express*, vol. 28, no. 26, pp. 39963–39975, 2020.

- [98] A. Rao, K. Abdelsalam, T. Sjaardema, A. Honardoost, G. F. Camacho-Gonzalez, and S. Fathpour, "Actively-monitored periodic-poling in thin-film lithium niobate photonic waveguides with ultrahigh nonlinear conversion efficiency of 4600% w- 1 cm- 2," *Optics express*, vol. 27, no. 18, pp. 25920–25930, 2019.
- [99] J. Hong, W. Huang, and T. Makino, "On the transfer matrix method for distributed-feedback waveguide devices," *Journal of lightwave technology*, vol. 10, no. 12, pp. 1860–1868, 1992.
- [100] L. Chrostowski and M. Hochberg, *Silicon photonics design: from devices to systems*. Cambridge University Press, 2015.
- [101] G. T. Reed, G. Mashanovich, F. Y. Gardes, and D. Thomson, "Silicon optical modulators," *Nature photonics*, vol. 4, no. 8, pp. 518–526, 2010.
- [102] R. W. Tkach, "Scaling optical communications for the next decade and beyond," *Bell Labs Technical Journal*, vol. 14, no. 4, pp. 3–9, 2010.
- [103] Q. Xu, B. Schmidt, S. Pradhan, and M. Lipson, "Micrometre-scale silicon electro-optic modulator," *nature*, vol. 435, no. 7040, pp. 325–327, 2005.
- [104] C. Sun, M. T. Wade, Y. Lee, J. S. Orcutt, L. Alloatti, M. S. Georgas, A. S. Waterman, J. M. Shainline, R. R. Avizienis, S. Lin, *et al.*, "Single-chip microprocessor that communicates directly using light," *Nature*, vol. 528, no. 7583, pp. 534–538, 2015.
- [105] A. Samani, E. El-Fiky, M. Osman, D. Patel, R. Li, M. Jacques, and D. Plant, "180 gb/s single carrier single polarization 16-qam transmission using an o-band silicon photonic iqm," *Optics express*, vol. 27, no. 10, pp. 14447–14456, 2019.
- [106] M. Aoki, M. Suzuki, H. Sano, T. Kawano, T. Ido, T. Taniwatari, K. Uomi, and A. Takai, "Ingaas/ingaasp mqw electroabsorption modulator integrated with a dfb

- laser fabricated by band-gap energy control selective area mocvd," *IEEE Journal of Quantum Electronics*, vol. 29, no. 6, pp. 2088–2096, 1993.
- [107] Y. Ogiso, J. Ozaki, Y. Ueda, N. Kashio, N. Kikuchi, E. Yamada, H. Tanobe, S. Kanazawa, H. Yamazaki, Y. Ohiso, *et al.*, "Over 67 ghz bandwidth and 1.5 v $\nu\pi$ inp-based optical iq modulator with nipi heterostructure," *Journal of lightwave technology*, vol. 35, no. 8, pp. 1450–1455, 2016.
- [108] Y. Ogiso, J. Ozaki, Y. Ueda, H. Wakita, M. Nagatani, H. Yamazaki, M. Nakamura, T. Kobayashi, S. Kanazawa, T. Fujii, *et al.*, "Ultra-high bandwidth inp iq modulator for beyond 100-gbd transmission," in *Optical Fiber Communication Conference*, pp. M2F–2, Optical Society of America, 2019.
- [109] E. L. Wooten, K. M. Kissa, A. Yi-Yan, E. J. Murphy, D. A. Lafaw, P. F. Hallemeier, D. Maack, D. V. Attanasio, D. J. Fritz, G. J. McBrien, *et al.*, "A review of lithium niobate modulators for fiber-optic communications systems," *IEEE Journal of selected topics in Quantum Electronics*, vol. 6, no. 1, pp. 69–82, 2000.
- [110] A. Rao, A. Patil, P. Rabiei, A. Honardoost, R. DeSalvo, A. Paoletta, and S. Fathpour, "High-performance and linear thin-film lithium niobate mach–zehnder modulators on silicon up to 50 ghz," *Optics letters*, vol. 41, no. 24, pp. 5700–5703, 2016.
- [111] P. O. Weigel, J. Zhao, K. Fang, H. Al-Rubaye, D. Trotter, D. Hood, J. Mudrick, C. Dallo, A. T. Pomerene, A. L. Starbuck, *et al.*, "Bonded thin film lithium niobate modulator on a silicon photonics platform exceeding 100 ghz 3-db electrical modulation bandwidth," *Optics express*, vol. 26, no. 18, pp. 23728–23739, 2018.
- [112] C. Wang, M. Zhang, X. Chen, M. Bertrand, A. Shams-Ansari, S. Chandrasekhar, P. Winzer, and M. Lončar, "Integrated lithium niobate electro-optic modulators operating at cmos-compatible voltages," *Nature*, vol. 562, no. 7725, pp. 101–104, 2018.

- [113] S. Sun, M. He, M. Xu, X. Zhang, Z. Ruan, L. Liu, and X. Cai, "120 gb s⁻¹ hybrid silicon and lithium niobate modulators with on-chip termination resistor," in *2020 Optical Fiber Communications Conference and Exhibition (OFC)*, pp. 1–3, IEEE, 2020.
- [114] M. He, M. Xu, Y. Ren, J. Jian, Z. Ruan, Y. Xu, S. Gao, S. Sun, X. Wen, L. Zhou, *et al.*, "High-performance hybrid silicon and lithium niobate mach–zehnder modulators for 100 gbit s⁻¹ and beyond," *Nature Photonics*, vol. 13, no. 5, pp. 359–364, 2019.
- [115] P. Kharel, C. Reimer, K. Luke, L. He, and M. Zhang, "Breaking voltage–bandwidth limits in integrated lithium niobate modulators using micro-structured electrodes," *Optica*, vol. 8, no. 3, pp. 357–363, 2021.
- [116] M. Xu, M. He, H. Zhang, J. Jian, Y. Pan, X. Liu, L. Chen, X. Meng, H. Chen, Z. Li, *et al.*, "High-performance coherent optical modulators based on thin-film lithium niobate platform," *Nature communications*, vol. 11, no. 1, pp. 1–7, 2020.
- [117] X. Chen, G. Raybon, D. Che, J. Cho, and K. Kim, "Transmission of 200-gbaud pdm probabilistically shaped 64-qam signals modulated via a 100-ghz thin-film linbo 3 i/q modulator," in *2021 Optical Fiber Communications Conference and Exhibition (OFC)*, pp. 1–3, IEEE, 2021.
- [118] A. Rao and S. Fathpour, "Compact lithium niobate electrooptic modulators," *IEEE Journal of Selected Topics in Quantum Electronics*, vol. 24, no. 4, pp. 1–14, 2017.
- [119] A. Honardoost, F. A. Juneghani, R. Safian, and S. Fathpour, "Towards subterahertz bandwidth ultracompact lithium niobate electrooptic modulators," *Optics express*, vol. 27, no. 5, pp. 6495–6501, 2019.
- [120] D. M. Pozar, *Microwave engineering*. John wiley & sons, 2011.

- [121] W. R. Eisenstadt and Y. Eo, "S-parameter-based ic interconnect transmission line characterization," *IEEE transactions on components, hybrids, and manufacturing technology*, vol. 15, no. 4, pp. 483–490, 1992.
- [122] J.-M. Liu, *Photonic devices*. Cambridge University Press, 2009.
- [123] D. D. Jones, "Semiconductor devices for high-speed optoelectronics, by giovanni ghione: Scope: monograph and review. level: undergraduate, postgraduate and early career researcher," 2011.
- [124] D. F. Williams and S. Schwarz, "Reduction of propagation losses in coplanar waveguide," in *1984 IEEE MTT-S International Microwave Symposium Digest*, pp. 453–454, IEEE, 1984.
- [125] A. Honardoost, R. Safian, A. Rao, and S. Fathpour, "High-speed modeling of ultra-compact electrooptic modulators," *Journal of Lightwave Technology*, vol. 36, no. 24, pp. 5893–5902, 2018.
- [126] X. Chen, S. Chandrasekhar, S. Randel, G. Raybon, A. Adamiecki, P. Pupalaiakis, and P. J. Winzer, "All-electronic 100-ghz bandwidth digital-to-analog converter generating pam signals up to 190 gbaud," *Journal of Lightwave Technology*, vol. 35, no. 3, pp. 411–417, 2017.
- [127] Y. N. Wijayanto, H. Murata, and Y. Okamura, "Electrooptic millimeter-wave–lightwave signal converters suspended to gap-embedded patch antennas on low- k dielectric materials," *IEEE Journal of Selected Topics in Quantum Electronics*, vol. 19, no. 6, pp. 33–41, 2013.

- [128] J. Zhang, Z. Zhao, C. Li, and Y. Li, "Broad-band integrated optical electric field sensor using reflection mach-zehnder waveguide modulator," *Fiber and Integrated Optics*, vol. 36, no. 4-5, pp. 157–164, 2017.
- [129] R. B. Waterhouse and D. Novak, "Integrated antenna/electro-optic modulator for rf photonic front-ends," in *2011 IEEE MTT-S International Microwave Symposium*, pp. 1–4, IEEE, 2011.
- [130] J. Zhang, F. Chen, and B. Liu, "Integrated photonic electric field sensor operating more than 26 ghz," *IEEE Microwave and Wireless Components Letters*, vol. 30, no. 10, pp. 1009–1012, 2020.
- [131] D. Park, V. Pagán, T. Murphy, J. Luo, A.-Y. Jen, and W. Herman, "Free space millimeter wave-coupled electro-optic high speed nonlinear polymer phase modulator with in-plane slotted patch antennas," *Optics express*, vol. 23, no. 7, pp. 9464–9476, 2015.
- [132] F. Mokhtari-Koushyar, E. Heidari, H. Dalir, C.-J. Chung, X. Xu, V. J. Sorger, and R. T. Chen, "Wideband multi-arm bowtie antenna for millimeter wave electro-optic sensors and receivers," *Journal of Lightwave Technology*, vol. 36, no. 16, pp. 3418–3426, 2018.
- [133] Y. N. Wijayanto, H. Murata, and Y. Okamura, "Wireless microwave-optical signal conversion in quasi-phase-matching electro-optic modulators using gap-embedded patch-antennas," *IEICE transactions on electronics*, vol. 96, no. 2, pp. 212–219, 2013.
- [134] O. D. Herrera, K.-J. Kim, R. Voorakaranam, R. Himmelhuber, S. Wang, V. Demir, Q. Zhan, L. Li, R. A. Norwood, R. L. Nelson, *et al.*, "Silica/electro-optic polymer optical modulator with integrated antenna for microwave receiving," *Journal of Lightwave Technology*, vol. 32, no. 20, pp. 3861–3867, 2014.

- [135] J. S. Dam, P. Tidemand-Lichtenberg, and C. Pedersen, "Room-temperature mid-infrared single-photon spectral imaging," *Nature photonics*, vol. 6, no. 11, pp. 788–793, 2012.
- [136] G. Li, Y. Chen, H. Jiang, and X. Chen, "Broadband sum-frequency generation using d_{33} in periodically poled LiNbO₃ thin film in the telecommunications band," *Optics letters*, vol. 42, no. 5, pp. 939–942, 2017.
- [137] Z. Hao, J. Wang, S. Ma, W. Mao, F. Bo, F. Gao, G. Zhang, and J. Xu, "Sum-frequency generation in on-chip lithium niobate microdisk resonators," *Photonics Research*, vol. 5, no. 6, pp. 623–628, 2017.
- [138] X. Ye, S. Liu, Y. Chen, Y. Zheng, and X. Chen, "Sum-frequency generation in lithium-niobate-on-insulator microdisk via modal phase matching," *Optics Letters*, vol. 45, no. 2, pp. 523–526, 2020.
- [139] H. Jiang, H. Liang, R. Luo, X. Chen, Y. Chen, and Q. Lin, "Nonlinear frequency conversion in one dimensional lithium niobate photonic crystal nanocavities," *Applied Physics Letters*, vol. 113, no. 2, p. 021104, 2018.
- [140] A. K. Hansen, P. E. Andersen, O. B. Jensen, B. Sumpf, G. Erbert, and P. M. Petersen, "Highly efficient single-pass sum frequency generation by cascaded nonlinear crystals," *Optics letters*, vol. 40, no. 23, pp. 5526–5529, 2015.
- [141] T. Sjaardema, A. Rao, and S. Fathpour, "Third-and fourth-harmonic generation in cascaded periodically-poled lithium niobate ultracompact waveguides on silicon," in *CLEO: Science and Innovations*, pp. STh1J–1, Optical Society of America, 2019.
- [142] S. Lauria and M. F. Saleh, "Mixing second and third-order nonlinear interactions in nanophotonic lithium-niobate waveguides," *arXiv preprint arXiv:2111.13796*, 2021.

- [143] S. Liu, Y. Zheng, and X. Chen, "Cascading second-order nonlinear processes in a lithium niobate-on-insulator microdisk," *Optics Letters*, vol. 42, no. 18, pp. 3626–3629, 2017.
- [144] R. Wolf, I. Breunig, H. Zappe, and K. Buse, "Cascaded second-order optical nonlinearities in on-chip micro rings," *Optics express*, vol. 25, no. 24, pp. 29927–29933, 2017.
- [145] D. D. Hickstein, D. R. Carlson, A. Kowligy, M. Kirchner, S. R. Domingue, N. Nader, H. Timmers, A. Lind, G. G. Ycas, M. M. Murnane, *et al.*, "High-harmonic generation in periodically poled waveguides," *Optica*, vol. 4, no. 12, pp. 1538–1544, 2017.
- [146] D. Wang, T. Ding, Y. Zheng, and X. Chen, "Cascaded sum-frequency generation and electro-optic polarization coupling in the PPLNOI ridge waveguide," *Optics Express*, vol. 27, no. 11, pp. 15283–15288, 2019.
- [147] Y. J. Ding, "Progress in terahertz sources based on difference-frequency generation," *JOSA B*, vol. 31, no. 11, pp. 2696–2711, 2014.
- [148] C. Erny, K. Moutzouris, J. Biegert, D. Kühlke, F. Adler, A. Leitenstorfer, and U. Keller, "Mid-infrared difference-frequency generation of ultrashort pulses tunable between 3.2 and 4.8 μm from a compact fiber source," *Optics letters*, vol. 32, no. 9, pp. 1138–1140, 2007.
- [149] J. Mishra, T. P. McKenna, E. Ng, H. S. Stokowski, M. Jankowski, C. Langrock, D. Heydari, H. Mabuchi, M. Fejer, and A. H. Safavi-Naeini, "Mid-infrared nonlinear optics in thin-film lithium niobate on sapphire," *Optica*, vol. 8, no. 6, pp. 921–924, 2021.

- [150] J. Yang and C. Wang, "Efficient terahertz generation scheme in a thin-film lithium niobate-silicon hybrid platform," *Optics Express*, vol. 29, no. 11, pp. 16477–16486, 2021.
- [151] S. Fathpour, "Emerging heterogeneous integrated photonic platforms on silicon," *Nanophotonics*, vol. 4, no. 2, pp. 143–164, 2015.
- [152] S. Liu, Y. Zheng, Z. Fang, X. Ye, Y. Cheng, and X. Chen, "Effective four-wave mixing in the lithium niobate on insulator microdisk by cascading quadratic processes," *Optics Letters*, vol. 44, no. 6, pp. 1456–1459, 2019.
- [153] G. I. Stegeman, D. J. Hagan, and L. Torner, " $\chi^{(2)}$ cascading phenomena and their applications to all-optical signal processing, mode-locking, pulse compression and solitons," *Optical and Quantum electronics*, vol. 28, no. 12, pp. 1691–1740, 1996.
- [154] T. Sjaardema, M. Malinowski, A. Rao, and S. Fathpour, "Low-harmonic generation in cascaded thin-film lithium niobate waveguides," *Advanced Photonics Research*, p. 2100262, 2022.
- [155] B. S. Elkus, K. Abdelsalam, S. Fathpour, P. Kumar, and G. S. Kanter, "Quantum-correlated photon-pair generation via cascaded nonlinearity in an ultra-compact lithium-niobate nano-waveguide," *Optics Express*, vol. 28, no. 26, pp. 39963–39975, 2020.
- [156] M. Wang, N. Yao, R. Wu, Z. Fang, S. Lv, J. Zhang, J. Lin, W. Fang, and Y. Cheng, "Strong nonlinear optics in on-chip coupled lithium niobate microdisk photonic molecules," *New Journal of Physics*, vol. 22, no. 7, p. 073030, 2020.
- [157] M. Jankowski, C. Langrock, B. Desiatov, A. Marandi, C. Wang, M. Zhang, C. R. Phillips, M. Lončar, and M. Fejer, "Ultrabroadband nonlinear optics in nanopho-

- tonic periodically poled lithium niobate waveguides," *Optica*, vol. 7, no. 1, pp. 40–46, 2020.
- [158] J. Wang, Q. Sun, and J. Sun, "Ultrafast all-optical logic and gate for csrz signals using periodically poled lithium niobate," *JOSA B*, vol. 26, no. 5, pp. 951–958, 2009.
- [159] C.-K. Hong, Z.-Y. Ou, and L. Mandel, "Measurement of subpicosecond time intervals between two photons by interference," *Physical review letters*, vol. 59, no. 18, p. 2044, 1987.
- [160] K.-H. Luo, S. Brauner, C. Eigner, P. R. Sharapova, R. Ricken, T. Meier, H. Herrmann, and C. Silberhorn, "Nonlinear integrated quantum electro-optic circuits," *Science advances*, vol. 5, no. 1, p. eaat1451, 2019.
- [161] H. Jin, F. Liu, P. Xu, J. Xia, M. Zhong, Y. Yuan, J. Zhou, Y. Gong, W. Wang, and S. Zhu, "On-chip generation and manipulation of entangled photons based on reconfigurable lithium-niobate waveguide circuits," *Physical review letters*, vol. 113, no. 10, p. 103601, 2014.